

# Applications of Spectroscopy in Environmental Monitoring of Gases and Aerosols

Guest Editors: Arnaud Cuisset, Dean S. Venables, Xiaoming Gao, and Hassen Aroui





---

# **Applications of Spectroscopy in Environmental Monitoring of Gases and Aerosols**

Journal of Spectroscopy

---

**Applications of Spectroscopy in  
Environmental Monitoring of  
Gases and Aerosols**

Guest Editors: Arnaud Cuisset, Dean S. Venables,  
Xiaoming Gao, and Hassen Aroui



---

Copyright © 2016 Hindawi Publishing Corporation. All rights reserved.

This is a special issue published in "Journal of Spectroscopy." All articles are open access articles distributed under the Creative Commons Attribution License, which permits unrestricted use, distribution, and reproduction in any medium, provided the original work is properly cited.

## Editorial Board

João Abrantes, Portugal  
Khaliq Ahmed, USA  
Faisal M. Alamgir, USA  
Wolfgang Anwand, Germany  
Gabriele Arnold, Germany  
Naoki Asakawa, Japan  
Luciano Bachmann, Brazil  
Mark Baker, UK  
Adam G. Balogh, Germany  
Malgorzata Baranska, Poland  
Lahcen Bih, Morocco  
Dhananjay Bodas, India  
Lars H. Böttger, Germany  
Damien Boyer, France  
Stefano Caldarelli, France  
Jose S. Camara, Portugal  
Brian Cannon, USA  
Elizabeth A. Carter, Australia  
Wee Chew, Singapore  
Jau-Wern Chiou, Taiwan  
Daniel O. Cicero, Italy  
Malcolm R. Clench, UK  
Stephen Cooke, USA  
Daniel Cozzolino, Australia  
Vincenza Crupi, Italy  
Arnaud Cuisset, France  
Eugen Culea, Romania  
Eric Da Silva, Canada  
Lesley Davenport, USA  
Alessandro De Giacomo, Italy  
Marcella Dell'aglio, Italy  
Renata Diniz, Brazil  
Ana Dominguez-Vidal, Spain  
Christophe Dujardin, France  
Thomas R. Eykyn, UK  
Michele Fedel, Italy

Davide Ferri, Switzerland  
Roberto Flammini, Italy  
Anatoly Frenkel, USA  
Nives Galić, Croatia  
Javier Garcia-Guinea, Spain  
Martin Giera, Netherlands  
Gianfranco Giubileo, Italy  
M.G.-Nikolaidis, New Zealand  
Andras Gorzsas, Sweden  
S. P. H.-Rivera, Puerto Rico  
Tino Hofmann, USA  
Shuchen Hsieh, Taiwan  
Xinyang Huang, China  
Hiromi Ikeura-Sekiguchi, Japan  
Fumiyuki Ito, Japan  
Rodolphe Jaffiol, France  
Christopher K. Jankowski, Canada  
ZhiLiang Jiang, China  
Dale Keefe, Canada  
Rizwan Hasan Khan, India  
Jeongkwon Kim, Republic of Korea  
Piotr Koczon, Poland  
Nikolaos Kourkoumelis, Greece  
Christoph Krafft, Germany  
K.S.V. Krishna Rao, India  
Nikša Krstulović, Croatia  
Violeta Lasic, Italy  
Adam F. Lee, UK  
Young Jong Lee, USA  
Nicolae Leopold, Romania  
Min Soo Lim, USA  
Alessandro Longo, Italy  
Paola Luches, Italy  
Mahmoud A. Mahmoud, USA  
Petre Makreski, Macedonia  
Dmitriy Malinovsky, UK

Djordje Mandrino, Slovenia  
Artem E. Masunov, USA  
Thomas G. Mayerhofer, Germany  
Yehia Mechref, USA  
Gellert Mezei, USA  
Shinichi Morita, Japan  
Kouichi Nakagawa, Japan  
Austin Nevin, Italy  
Masaki Oura, Japan  
Giancarlo Pace, Portugal  
Carlos Andres Palacio, Belgium  
Jose M. Pedrosa, Spain  
Simona C. Pinzaru, Romania  
Piotr Przybylski, Poland  
Maria Ramil, Spain  
Ihtesham ur Rehman, UK  
Tomasz Ruman, Poland  
Davidson Sajan, India  
Stephane Schilt, Switzerland  
Feride Severcan, Turkey  
Zhifeng Shao, USA  
Masanori Shinohara, Japan  
Maciej Sitarz, Poland  
Rafal Sitko, Poland  
Massimo Tallarida, Germany  
Riadh Ternane, Tunisia  
Pedro D. Vaz, Portugal  
Stéphane Viel, France  
Annemarie Wagner, Sweden  
Thomas Walther, UK  
Chuji Wang, USA  
Chih-Che Wu, Taiwan  
Maria Carmen Yebra-Biurrun, Spain  
Guoqiang Yu, USA  
Kassym Zhumadilov, Japan  
Zoran D. Zujovic, New Zealand

# Contents

---

## **Applications of Spectroscopy in Environmental Monitoring of Gases and Aerosols**

Arnaud Cuisset, Dean S. Venables, Xiaoming Gao, and Hassen Aroui

Volume 2016, Article ID 2575782, 1 page

## **Background Radiance Estimation for Gas Plume Quantification for Airborne Hyperspectral Thermal Imaging**

Ramzi Idoughi, Thomas H. G. Vidal, Pierre-Yves Foucher, Marc-André Gagnon, and Xavier Briottet

Volume 2016, Article ID 5428762, 17 pages

## **Optical Estimation on Pollution Level of Respirable Dust Based on Infrared Transmitting Behavior in Coalmine Fully Mechanized Working Face**

Wen-Zheng Wang, Yan-Ming Wang, and Guo-Qing Shi

Volume 2016, Article ID 2626414, 13 pages

## **Atmospheric Aerosols Detection Research with a Dual Field of View Lidar**

Lv Lihui, Zhang Tianshu, Liu Cheng, Dong Yunsheng, Chen Zhenyi, Fan Guangqiang, Liu Yang, and Liu Wenqing

Volume 2015, Article ID 459460, 6 pages

## **Multi-Quartz Enhanced Photoacoustic Spectroscopy with Different Acoustic Microresonator Configurations**

Huadan Zheng, Xukun Yin, Lei Dong, Hongpeng Wu, Xiaoli Liu, Weiguang Ma, Lei Zhang, Wangbao Yin, and Suotang Jia

Volume 2015, Article ID 218413, 6 pages

## **Analysis of ACAM Data for Trace Gas Retrievals during the 2011 DISCOVER-AQ Campaign**

C. Liu, X. Liu, M. G. Kowalewski, S. J. Janz, G. González Abad, K. E. Pickering, K. Chance, and L. N. Lamsal

Volume 2015, Article ID 827160, 7 pages

## **Retrieval of Atmospheric CO<sub>2</sub> and CH<sub>4</sub> Variations Using Ground-Based High Resolution Fourier Transform Infrared Spectra**

Tian Yuan, Liu Cheng, Sun You Wen, Xie Pin Hua, Wang Wei, Liu Wen Qing, Liu Jian Guo, Li Ang, Hu Ren Zhi, and Zeng Yi

Volume 2015, Article ID 736382, 9 pages

## Editorial

# Applications of Spectroscopy in Environmental Monitoring of Gases and Aerosols

**Arnaud Cuisset,<sup>1</sup> Dean S. Venables,<sup>2</sup> Xiaoming Gao,<sup>3</sup> and Hassen Aroui<sup>4</sup>**

<sup>1</sup>*Laboratoire de Physico-Chimie de l'Atmosphère, Université du Littoral Côte d'Opale, 59140 Dunkerque, France*

<sup>2</sup>*Department of Chemistry, National University of Ireland, University College of Cork, Cork, Ireland*

<sup>3</sup>*Anhui Institute of Optics and Fine Mechanics, Chinese Academy of Sciences, Hefei 230031, China*

<sup>4</sup>*Laboratoire de Dynamique Moléculaire et Matériaux Photoniques, Université de Tunis, Ecole Nationale Supérieure d'Ingénieurs de Tunis, 5 Avenue Taha Hussein, 1008 Tunis, Tunisia*

Correspondence should be addressed to Arnaud Cuisset; [arnaud.cuisset@univ-littoral.fr](mailto:arnaud.cuisset@univ-littoral.fr)

Received 7 May 2016; Accepted 8 May 2016

Copyright © 2016 Arnaud Cuisset et al. This is an open access article distributed under the Creative Commons Attribution License, which permits unrestricted use, distribution, and reproduction in any medium, provided the original work is properly cited.

Spectroscopy has long been the most important tool for investigating the earth's atmosphere. Indeed, it is worth noting that spectroscopy is the only method that can be used for remote observations of the atmosphere. Remote measurements are indispensable given both the spatial heterogeneity of the atmosphere's chemical composition and physical properties, as well as the financial and technical difficulties (or outright inability) to probe the atmosphere directly with in situ sensors of any type. In situ spectroscopic methods are also widely used in atmospheric studies, including measuring short-lived reactive species that drive the chemistry of the atmosphere, isotopologue concentrations, and the optical properties of particles, which strongly alter radiative forcing and influence climate. The information provided by such spectroscopic methods is critical to determining air quality, identifying emissions of air pollutants, quantifying the magnitude and fluxes of climate forcing agents, ensuring compliance with regulations, and informing environmental policies at national and international levels.

Despite its long history, new developments in atmospheric spectroscopy continue to be made both on the instrumental side and on the analysis of spectra. On one hand, on-going instrumental advances continue to be driven by new technologies in light sources, sample environments, and detectors; on the other hand, the ability and need to collect increasingly detailed spatial and temporal information continue to promote the importance of novel spectral analysis strategies. So, along with the emergence of new techniques, even apparently mature spectroscopic techniques continue to evolve in both scope and performance.

This special issue focuses on several examples of developments in applying spectroscopy to atmospheric and air quality measurements. The articles feature a range of techniques covering wavelengths from the ultraviolet through to the mid-infrared spectral regions using both active and passive light sources. This broad spectral range is suited to various measurement targets, ranging from water vapour and the major anthropogenic greenhouse gases, carbon dioxide and methane, to the classical air pollutants, ozone and nitrogen dioxide. Although most applications focus on direct atmospheric observations, the applications of spectroscopy to air quality in mines and industrial plume monitoring are also considered. Technological solutions such as acoustic microresonators and dual field-of-view lidar allow us to improve sensitivity detection limits for gas detection and improved coverage of atmospheric aerosols at near and far ranges. It is also notable how strongly spectral analysis features in the papers. This is to be expected given the increasing spatial information from various approaches and the importance of remote observations. The articles underline these considerations with new inversion algorithms and calibration methods for trace gas retrievals and hyperspectral imaging in the long-wave infrared. Taken together, these studies indicate the breadth of methods, the range of applications, and the on-going development in spectroscopy as an essential tool for understanding the atmosphere.

*Arnaud Cuisset  
Dean S. Venables  
Xiaoming Gao  
Hassen Aroui*

## Research Article

# Background Radiance Estimation for Gas Plume Quantification for Airborne Hyperspectral Thermal Imaging

Ramzi Idoughi,<sup>1,2</sup> Thomas H. G. Vidal,<sup>1</sup> Pierre-Yves Foucher,<sup>1</sup>  
Marc-André Gagnon,<sup>3</sup> and Xavier Briottet<sup>1</sup>

<sup>1</sup>ONERA, The French Aerospace Lab, DOTA, 2 Avenue Edouard Belin, 31400 Toulouse, France

<sup>2</sup>Institut Supérieur de l'Aéronautique et de l'Espace (ISAE), Toulouse, France

<sup>3</sup>Telops Inc., 100-2600 St-Jean-Baptiste Avenue, Québec, QC, Canada G2E 6J5

Correspondence should be addressed to Pierre-Yves Foucher; pierre-yves.foucher@onera.fr

Received 2 October 2015; Accepted 23 February 2016

Academic Editor: Hassen Aroui

Copyright © 2016 Ramzi Idoughi et al. This is an open access article distributed under the Creative Commons Attribution License, which permits unrestricted use, distribution, and reproduction in any medium, provided the original work is properly cited.

Hyperspectral imaging in the long-wave infrared (LWIR) is a mean that is proving its worth in the characterization of gaseous effluent. Indeed the spectral and spatial resolution of acquisition instruments is steadily decreasing, making the gases characterization increasingly easy in the LWIR domain. The majority of literature algorithms exploit the plume contribution to the radiance corresponding to the difference of radiance between the plume-present and plume-absent pixels. Nevertheless, the off-plume radiance is unobservable using a single image. In this paper, we propose a new method to retrieve trace gas concentration from airborne infrared hyperspectral data. More particularly the outlined method improves the existing background radiance estimation approach to deal with heterogeneous scenes corresponding to industrial scenes. It consists in performing a classification of the scene and then applying a principal components analysis based method to estimate the background radiance on each cluster stemming from the classification. In order to determine the contribution of the classification to the background radiance estimation, we compared the two approaches on synthetic data and Telops Fourier Transform Spectrometer (FTS) Imaging Hyper-Cam LW airborne acquisition above ethylene release. We finally show ethylene retrieved concentration map and estimate flow rate of the ethylene release.

## 1. Introduction

Anthropogenic sources, especially industrial, have a major contribution to air pollution and security issues. However, these emissions remain poorly estimated at a high spatial resolution over heterogeneous scenes, like industrial plants.

Most of these emissions present a spectral signature in the thermal infrared domain. This is the reason why thermal hyperspectral imaging systems are deployed for their characterization. More, as such plume has a small extent they require a high spatial resolution imagery which can be achieved with existing airborne systems [1–3].

However, signature of gaseous effluents differs highly from usual targets since the plume modifies the spectral signature of the background: different pixels in the data cube that contain the same gaseous plume could have a totally

different spectral signature. At first order, spectral signature of these pixels will correspond to background spectra affected by either absorption or emission of the gas. This variability depends on background materials and temperature difference between the ground and the plume.

Existing approaches which use the spectral information of such sensor to characterize gas plume can be divided into two stages: endmember decomposition techniques to estimate the background properties [4–6] and trace element detection [7–10] or quantification methods [11–13] based on estimated gas differential signature (difference for each “on-plume pixel” between measured radiance and “off-plume” estimated radiance). Then it has been shown that background uncertainty and heterogeneity are one of the major sources of incertitude in gas quantification and detection limit [14–16]. Depending on the ground properties the same amount

of gas can have a signature; thus a retrieved concentration is modified by a factor of ten.

This paper aims to reduce the quantification error due to misestimation of background properties.

To deal with ground variability for heterogeneous scene, clustering was suggested to compute covariance matrices of different spatial classes composing the background [7, 11], thus creating independent classes on which detection algorithms are applied.

The major limitation of these methods is that clustering background step may be contaminated by the presence of the gas plume [4, 5, 17].

If existing in the reflective domain, for example, the very weak gas plume signature has little impact on the clustering stage [7, 8]. But for quite strong signature in the thermal domain, gases plume anomalous classes can appear.

To overcome such issues, the clustering phase should be achieved outside the spectral bands corresponding to the strong absorption of the gas to be detected. Some recent works [18] show that such Selected-Band approach can be used to estimate background radiance under the plume with an interesting precision for various scenes.

In this paper, we look for a background estimation method that will efficiently reduce the gas retrieval quantification error in the case of heterogeneous scene. In this work we introduce a novel method to estimate pixel by pixel the off-plume radiance under the plume and the specific additional spectral signature introduced by the gas plume using airborne hyperspectral data.

This method aims to overcome the difficulties that arise from the inherent mixture of the heterogeneous background and the gas plume spectra. We decompose the scene according to the spectral-spatial information, and, for each pixel of each cluster, we estimate differential gas signature taking into account background variability and gas spectral behavior.

This paper is structured as follows. Section 2 is dedicated to the description of the methodology. Then, Sections 3 and 4 evaluate the application of our method on synthetic data and Telops Hyper-Cam airborne platform data. Finally, concluding remarks are given in Section 5.

## 2. Methodology

*2.1. Plume Detection.* Plume detection is an important step for gas quantification process. It allows selecting the plume area, where the background radiance has to be estimated, and the off-plume area useful to getting background properties.

In the literature, several algorithms have been proposed to detect the presence of gas from hyperspectral data. Spectral Matched Filter (SMF) [4] was chosen in this study because it produced a good detection of the plume with a low number of false alarms.

Let  $\mathbf{X}$  be a hyperspectral image of  $N$  pixels and  $N_b$  bands, represented by an  $N \times N_b$  matrix. With  $\mathbf{T}$  being the gaseous target spectrum, we can write for the  $i$ th pixel  $\mathbf{x}_i$  of the hyperspectral image  $\mathbf{X}$ :

$$\mathbf{x}_i = \mathbf{T} \cdot \boldsymbol{\alpha}_i + \mathbf{d}, \quad (1)$$

where  $\boldsymbol{\alpha}$  is the target fit coefficients (abundances) and  $\mathbf{d}$  is the residual vector to be minimized. To retrieve the abundances  $\boldsymbol{\alpha}$ , we need to solve the unconstrained regression (see (1)). The analytic solution of this regression is

$$\boldsymbol{\alpha}_i = \frac{\mathbf{T}^T \boldsymbol{\Sigma}_X^{-1} \mathbf{x}_i}{\mathbf{T}^T \boldsymbol{\Sigma}_X^{-1} \mathbf{T}}, \quad (2)$$

where  $\boldsymbol{\Sigma}_X$  is the covariance matrix of this scene. An unbiased estimation of  $\boldsymbol{\Sigma}_X$  can be calculated as follows:

$$\boldsymbol{\Sigma}_X = \frac{1}{N-1} \cdot \sum_{i=1}^N (\mathbf{x}_i - \langle \mathbf{x} \rangle) (\mathbf{x}_i - \langle \mathbf{x} \rangle)^T. \quad (3)$$

We consider here the targeted gases as known. Hence, we use the spectra of targeted gases from the Pacific Northwest National Laboratory (PNNL) absorbance Library [19, 20] to construct  $\mathbf{T}$ . The detection performance can be improved by using an estimation of  $\boldsymbol{\Sigma}_X$  involving only plume-absent pixels.

Once the vector of abundances  $\boldsymbol{\alpha}$  is calculated, the plume mask is deduced by thresholding.

*2.2. Selected-Band Approach (SB).* The principal components analysis (PCA) was applied by many authors [10, 11, 21] in order to obtain a representation of the background radiance of plume-present pixels ( $L_{\text{bkg}}(\lambda)$ ). First, the principal vectors are computed using the plume-absent pixels radiances. Then, background radiances of plume-present pixels are assumed to lie in the subspace spanned by these principal vectors.

Niu et al. [18] go even further by developing an approach to estimate the background radiance. This approach is based on the fact that, in plume presence, the on-plume radiance ( $L_{\text{on}}(\lambda)$ ) is essentially equal to its background (off-plume) radiance over the most transparent spectral bands. Using this observation, they combine a Selected-Band algorithm to determine these transparent spectral bands with the PCA in order to estimate  $L_{\text{bkg}}$ .

Thereafter, in the present paper, we shall refer to this method simply as Selected-Band (SB).

After a plume detection on the hyperspectral image  $\mathbf{X}$ ,  $N_{\text{off}}$  pixels do not contain any plume gas. A  $N_{\text{off}} \times N_b$  matrix  $\mathbf{L}_{\text{off}}$  is constructed by arranging the off-plume measured radiance spectra. A PCA model is then given by

$$\mathbf{L}_{\text{off}} = \mathbf{U}_{\text{off}} \cdot \mathbf{P}^T + \mathbf{E}_{\text{off}}, \quad (4)$$

where  $\mathbf{U}_{\text{off}}$  is an  $N_{\text{off}} \times N_p$  matrix of coefficients for plume-absent pixels,  $\mathbf{P}$  is an  $N_b \times N_p$  of principal components, and  $\mathbf{E}_{\text{off}}$  is the residual matrix.  $N_p$  is the number of considered principal components. For the used data, we found  $N_p = 10$  to be an appropriate choice. It allows us to save more than 99.9% of the information.

Since the background radiances of plume-present pixels are assumed to lie in the subspace spanned by the principal components  $\mathbf{P}$ , the matrix  $\mathbf{L}_{\text{bkg}}$  of the background radiance spectra of the  $N_{\text{on}}$  plume-present pixels could be expressed as follows:

$$\mathbf{L}_{\text{bkg}} = \mathbf{U} \cdot \mathbf{P}^T + \mathbf{E}_{\text{bkg}}. \quad (5)$$

$\mathbf{U}$  is an  $N_{\text{on}} \times N_{\text{p}}$  matrix of unknown coefficients to be determined.  $\mathbf{E}_{\text{bkg}}$  is the residual matrix in this case.

For this purpose, a second PCA model is written for the  $N_{\text{on}}$  plume-present pixels, using only the  $N_{\text{SB}}$  bands, where the gas absorption coefficient is virtually nil:

$$\mathbf{L}_{\text{bkg}}^{\text{sb}} = \mathbf{L}_{\text{on}}^{\text{sb}} = \mathbf{U} \cdot \mathbf{P}^{\text{sbT}} + \mathbf{E}_{\text{on}}, \quad (6)$$

where  $\mathbf{L}_{\text{on}}^{\text{sb}}$  is an  $N_{\text{on}} \times N_{\text{SB}}$  matrix, containing the on-plume measured radiance spectra for the selected bands.  $\mathbf{P}^{\text{sbT}}$  is an  $N_{\text{SB}} \times N_{\text{p}}$  matrix of principal components;  $\mathbf{E}_{\text{on}}$  is the residual matrix.

By using the Moore-Penrose pseudoinverse of the matrix  $\mathbf{P}^{\text{sb}}$  ( $\mathbf{P}^{\text{sb}\dagger} = (\mathbf{P}^{\text{T}}\mathbf{P})^{-1}\mathbf{P}^{\text{T}}$ ), a least-square estimate for  $\mathbf{U}$  is given by

$$\mathbf{U} = \mathbf{L}_{\text{on}}^{\text{sb}} \cdot \mathbf{P}^{\text{sb}\dagger\text{T}}. \quad (7)$$

An estimation of the background radiances of plume-present pixels is thus obtained by the following expression:

$$\mathbf{L}_{\text{bkg}} = \mathbf{L}_{\text{on}}^{\text{sb}} \cdot \mathbf{P}^{\text{sb}\dagger\text{T}} \cdot \mathbf{P}^{\text{T}}. \quad (8)$$

The SB method has two leading limitations: the first comes from the assumption that  $\mathbf{L}_{\text{bkg}}^{\text{sb}} = \mathbf{L}_{\text{on}}^{\text{sb}}$ . This equality is not effective if the temperature of the plume is different from the ambient atmospheric temperature. Indeed, this temperature difference will have an impact on the transmission of atmospheric gases and therefore on the on-plume radiance outside gases signatures.

The second limitation relates to the case of heterogeneous soil. SB method as presented by Niu et al. can be limited if some background plume-present pixels are not well represented in plume-absent pixels. We propose otherwise to solve this second point using a classification of the scene.

### 2.3. Clustering-Based Selected-Band Method (CSB Method)

**2.3.1. Classification of the Scene.** Since Funk et al. [7] the classification of a hyperspectral scene is a main preliminary step of plume characterization through this scene. Funk et al. showed that classification improves the results of plume detection algorithms. They concluded that clustering data and removing the mean values could be seen as a type of automatic background suppression.

Moreover, the classification of the scene aims to carry off the disturbances on plume's quantification due to the heterogeneity of the soil [15].

In this subsection, we explain the classification process in order to enhance the background radiance estimation. A first classification is carried out on the plume-present pixels (a plume detection algorithm is executed upstream); another is done on the rest of the image.

This classification is organized in two stages: first, we perform a principal components transform [4] on the radiance spectra of the pixels of interest. Then, we just select the first components for further classification because the important background information is included in these components.

Finally, we carry out a classical  $k$ -means on these components to classify the scene.

The interest of this dimension reduction is to shorten the time processing of the  $k$ -means algorithm, without deteriorating its performances. The number of the retained components depends on the image to be treated. Usually, the use of the 3 first principal components is sufficient to have a good classification of the scene.

We choose the  $k$ -means algorithm for our classification, at one hand, because it is an unsupervised algorithm. Thus, it will be appropriate for a large number of different hyperspectral images. On the other hand, this algorithm is one of the fastest clustering algorithms.

At the end of this step, we obtain  $N_{\text{C}}$  classes in the area without plume and  $N_{\text{CP}}$  classes containing plume. The number of these clusters depends on the threshold  $D_{\text{max}}$ , used to specify the maximum distance of a pixel to the centroid of its cluster.

**2.3.2. Clustering-Based (CB) Background Radiance Estimation.** A first approach of Clustering-Based (CB) background radiance estimation we used consists in a classes matching between the plume-present and plume-absent regions.

The area under the plume has a petty spatial extent compared to the rest of the scene, whereof it only contains a small number of classes. In most cases it stands to reason to assume the classes under the plume as an extension of classes outside the plume and we assume that the presence of gas does not change the main properties of background. Indeed, the threshold  $D_{\text{max}}$  is selected such that pixels belonging to the same class have nearly the same characteristics (ground temperature and emissivity, atmospheric profiles). Thus, within a class, the off-plume radiance  $L_{\text{off}}$  is very close from one pixel to another.

For each plume-present class  $\text{CP}_i$ , the average spectrum of its pixels is calculated; it is then compared to the average spectra of all plume-absent classes  $(\text{C}_j)_{1 \leq j \leq N_{\text{C}}}$ . Readers will note that the comparison is performed only on bands where the target gases absorption coefficients are very small. Class  $\text{C}_{j^*}$  with the minimal distance from the plume-present class  $\text{CP}_i$  and the latter are considered to be the same. For a pixel  $\mathbf{x}_{\text{p}}$  in this class  $\text{CP}_i$ , we consider that its background radiance  $L_{\text{bkg}}(\mathbf{x}_{\text{p}})$  is equal to the mean radiance of pixels belonging to class  $\text{C}_{j^*}$ .

The CB method bypasses the soil heterogeneity limitation of the method SB. However, it does not take into account the intraclass variability of the background radiance. In the following paragraph we will present another Clustering-Based method that appropriates the benefits of SB and CB methods of  $L_{\text{bkg}}$  estimation, without their shortcomings.

**2.3.3. Clustering-Based Selected-Band Method (CSB Method).** In order to improve the background radiance estimation given by the Selected-Band approach (see Section 2.2) and the Clustering-Based method (see Section 2.3.2), we propose to perform this method on each cluster stemming from the classification (Section 2.3.1).

After a plume detection, classifications of the scene are realized separately for plume-absent pixels and for plume-present pixels; then each class of plume-present pixels is associated with a plume-absent pixels class. For each plume-present class  $CP_i$ , the Selected-Band approach is performed using (8) with a matrix  $\mathbf{P}_{C_{j^*}}^T$  derived from a PCA involving the pixels of the class  $C_{j^*}$ . Recall that the latter corresponds to the plume-absent class with the minimal distance from the plume-present class  $CP_i$ :

$$\mathbf{L}_{\text{bkg}}^{CP_i} = \mathbf{L}_{\text{on}}^{\text{sb } CP_i} \cdot \mathbf{P}_{CP_i}^{\text{sb}^T} \cdot \mathbf{P}_{CP_i}^T \quad (9)$$

In the following sections, we will present the improvement of background radiance estimation for plume-present pixels due to this new method, both on synthetic and real scenes.

### 3. Application on Synthetic Data

**3.1. Presentation of the Synthetic Data.** To evaluate the performances of background radiance estimation, synthetic data of an industrial scene were used. These data were simulated using a tool we have developed in order to provide a comprehensive test where the “truth” is known.

The dimensions of the simulated images are  $200 \times 200 \times 107$  (rows by columns by spectral dimension). The wavenumber range used is  $800$  to  $1330 \text{ cm}^{-1}$  with a resolution of  $5 \text{ cm}^{-1}$ . In this subsection, we describe the process of synthetic data generation.

**3.1.1. Ground Simulation.** We first defined the distribution of soil composition. Several materials frequently present in industrial scenes (asphalt, copper, aluminum, grass, etc.) were chosen (see Figure 1). Then we attributed for each pixel of the image the appropriate physical properties (emissivity and temperature), according to the present material.

The emissivities were taken from ASTER data base [22]. Figure 2(b) represents the emissivities of the different materials present through the synthetic scene.

The ground temperature varies widely depending on weather conditions, soil composition, orientation of the surfaces, and the relief of the scene (shadow effect). It is therefore very difficult to have a realistic estimate of this quantity. The values we have chosen are close to those measured during the CAPITOUL [23] experiment.

In order to take into account the intraclass variability of the ground temperature, a Gaussian white noise was added to this parameter with a standard deviation of  $1\text{--}3 \text{ K}$  according to the material. In contrast, we did not take into account the intraclass variability of ground emissivity.

**3.1.2. Atmospheric Profiles Integration.** We assume that the scene dimensions are small enough to consider a spatially uniform atmosphere over the image. The atmospheric species (especially water vapor and ozone), the pressure, and the temperature profiles are set for the different altitudes of the atmospheric layers. For this purpose we have used models derived from radiosonde measurements.

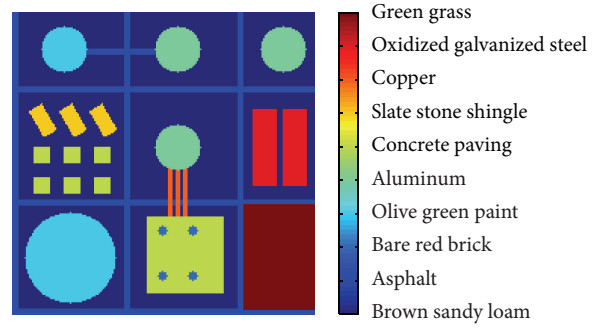


FIGURE 1: Spatial distribution of the different ground materials composing the scene.

At this stage, we generate a free-plume hyperspectral image of the scene, based on MODTRAN calculations, using COMANCHE software [24].

**3.1.3. Gas Signature.** The different gas species absorb light at various wavelengths. This phenomenon depends on the electronic, vibrational, and rotational bands of the gas molecules.

In this study, we selected two pollutant gases with very different radiative behavior. The sulfur dioxide ( $\text{SO}_2$ ) has a spread absorption spectrum on the  $7.5\text{--}12.5 \mu\text{m}$  band as shown in Figure 4, while the ammonia ( $\text{NH}_3$ ) presents several narrow spectral bands, especially for the wavelengths  $10.42 \mu\text{m}$  and  $10.75 \mu\text{m}$ , which correspond to  $960 \text{ cm}^{-1}$  and  $930 \text{ cm}^{-1}$  in terms of wavenumber.

The absorption spectra of Figure 4 are taken from the high resolution library of the PNNL. These spectra were reduced to a  $5 \text{ cm}^{-1}$  spectral resolution to be consistent with typical sensor spectral resolution.

**3.1.4. Plume Distribution Simulation.** In order to introduce the plume’s radiative impact to the free-plume signal, we have to model the 3D plume distribution in the scene, which is to define for each pixel of the plume the vertical profile of the present gases.

ADMS-Aircraft (Atmospheric Dispersion Modelling System) code [25] was used to generate a Gaussian plume based on the Brigg equation for plume dynamics [26]. The use of ADMS-Aircraft code requires the specification of some inputs related to the scene geometry, the atmospheric and meteorological conditions (in particular the wind speed and direction), and the plume initial conditions like the release rate/velocity/temperature.

Figure 5 shows the distribution of integrated concentration of a simulated  $\text{SO}_2$  plume with the following parameters:

- (i) outflow rate ( $\text{SO}_2$ ):  $222 \text{ g/s}$ ,
- (ii) outflow rate ( $\text{NH}_3$ ):  $11.39 \text{ g/s}$ ,
- (iii) stack height:  $20 \text{ m}$ ,
- (iv) stack radius:  $3 \text{ m}$ ,
- (v) plume ejection speed:  $2 \text{ m/s}$ ,

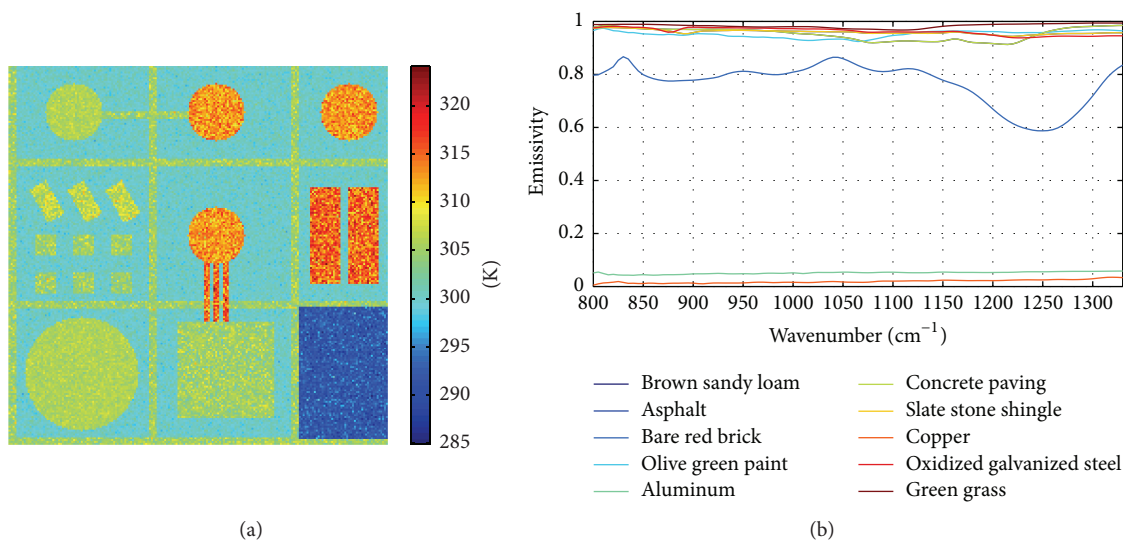


FIGURE 2: Ground parameters simulation. (a) Ground temperature map. (b) Emissivity spectra of materials present in the synthetic scene.

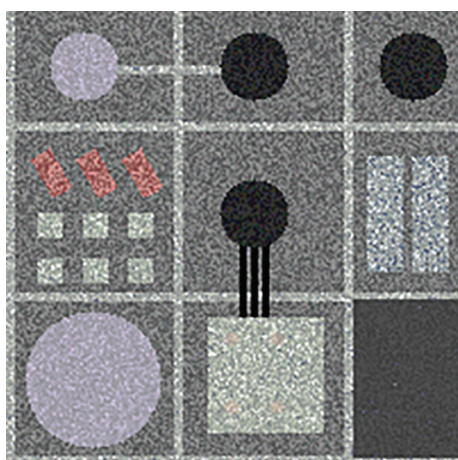


FIGURE 3: Synthetic refinery scene without plume. Image in RGB colors, representing the bands (R:  $820\text{ cm}^{-1}$ , G:  $965\text{ cm}^{-1}$ , and B:  $1165\text{ cm}^{-1}$ ).

- (vi) plume ejection direction: vertical,
- (vii) wind speed: 2 m/s.

A plume temperature distribution simulation is also needed to introduce the plume's radiative impact on the free-plume signal. To introduce plume temperature distribution needed to estimate the plume's radiative impact on the free-plume signal, we only set the gas exit temperature assuming that  $\Delta T$ , the difference between the plume temperature ( $T_p$ ) and the initial ambient temperature ( $T_a$ ), follows the same distribution compared to the gas concentration [11]. In our simulation we fixed  $\Delta T$  at the emission source to 300 K.

The radiance signal of the plume-present scene is represented in Figure 6 and that of the plume-absent scene in Figure 3. This signal is obtained using COMANCHE software that takes into account all the parameters described above.

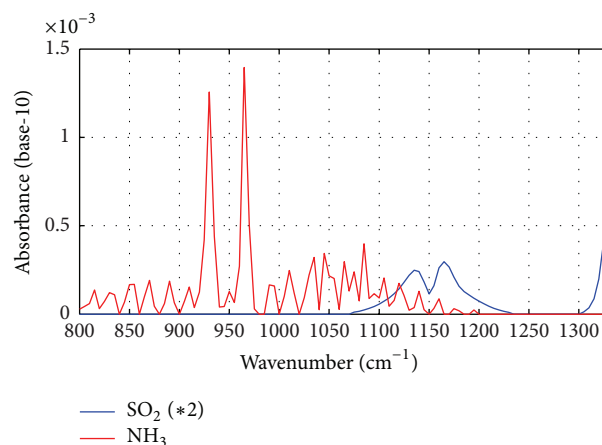


FIGURE 4: Absorptive coefficient spectra of sulfur dioxide (blue curve) and ammonia (red curve).

### 3.2. Results and Discussion

**3.2.1. Plume Detection.** The first step performed is the plume detection. The SMF algorithm was applied twice: the first time for detecting  $\text{SO}_2$ . The absorbance of this gas was used to model the associated target vector  $\mathbf{T}$ . The second time the vector  $\mathbf{T}$  was taken equal to the absorbance of  $\text{NH}_3$ . After two thresholding operations on these results, we consider that the plume region is the union of the two masks. Note that a morphological opening operation was performed in order to remove the detection artifacts.

Figure 7 represents the plume mask obtained at the end of these treatments.

**3.2.2. Classification of the Synthetic Scene.** In this subsection, we evaluate the efficiency of the proposed classification method. For this purpose, the confusion matrix and the Cohen kappa coefficient are used.

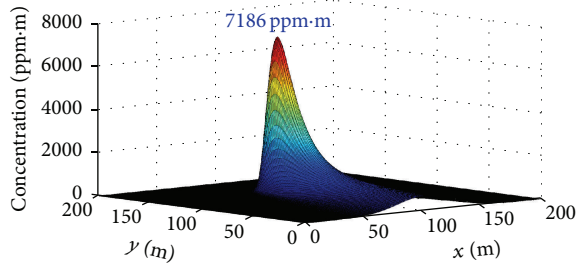


FIGURE 5: Distribution of  $\text{SO}_2$  concentration of the simulated plume, with an outflow rate of 222 g/s and a wind speed of 2 m/s.

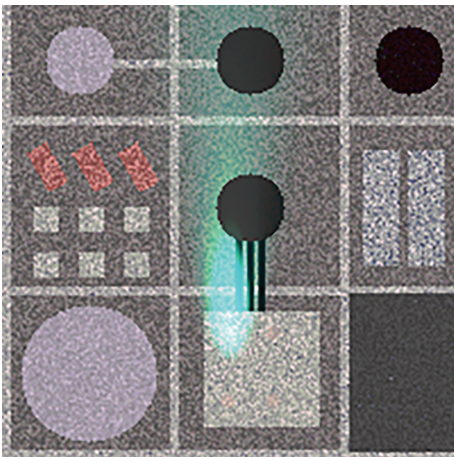


FIGURE 6: Synthetic refinery scene with a Gaussian plume of  $\text{SO}_2$  and  $\text{NH}_3$ . Image in RGB colors, representing the bands (R:  $820 \text{ cm}^{-1}$ , G:  $965 \text{ cm}^{-1}$ , and B:  $1165 \text{ cm}^{-1}$ ).

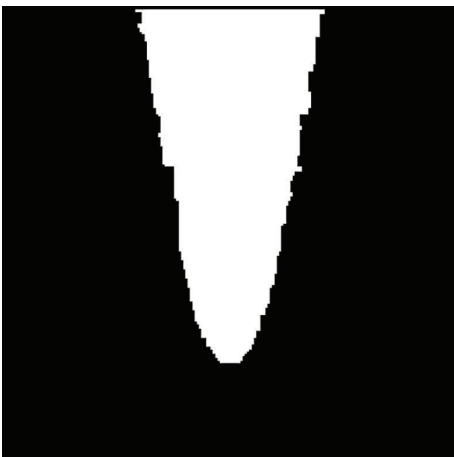


FIGURE 7: Plume detection mask for the synthetic refinery scene.

In Figure 8, we illustrated the classification results on the synthetic refinery scene, both for the plume-absent area (Figure 8(a)) and the plume-present area (Figure 8(b)).

Otherwise, in Table 1, we figured the confusion matrix of the two classifications realized. This matrix represents, for each material present in the synthetic scene, its distribution

TABLE 1: Confusion matrix of the classifications performed on the synthetic refinery scene.

(a)					
Material	Classes of the plume-absent area				
	1	2	3	4	5
Green grass	3149	141	0	0	0
Brown sandy loam	3	15241	121	0	0
Olive green paint	0	15	3165	350	0
Asphalt	0	410	2543	999	0
Bare red brick	0	0	51	36	0
Concrete paving	0	206	1695	891	0
Slate stone shingle	0	380	220	3	0
Oxidized galvanized steel	14	686	734	198	0
Aluminum	0	0	0	0	709
(b)					
Material	Classes of the plume-present area				
	1	2	3	4	
Brown sandy loam	5145	9	0	0	
Asphalt	128	612	0	0	
Bare red brick	0	29	0	0	
Concrete paving	46	373	0	0	
Copper	0	0	60	220	
Aluminum	0	0	0	1418	

according to the obtained clusters. The classification of the plume-absent region yields to 5 clusters, while the plume-present classification leads to 4 clusters.

From Figure 8 and Table 1, one can notice that materials could be sorted into three different families: Green grass, {Aluminum + Copper}, and the other materials of the scene. This result is consistent with the ground parameters distribution: the surface temperature of the Green grass is lower than the temperature of other materials (see Figure 2(a)). Moreover, aluminum and copper are reflective materials, unlike the other materials (see Figure 2(b)).

Inside the two last families of materials, the discrimination is quite difficult to achieve. Indeed, the radiances of those materials are very close. Nevertheless, the performed classifications are rather successful. The Cohen kappa coefficient is equal to 0.61 for the plume-absent classification; the latter equals 0.81 for the plume-present classification. According to the characterization done by Landis and Koch [27] on the values of the kappa coefficient, our classifications present a substantial (0.61) agreement and an almost perfect agreement (0.81).

*3.2.3. Comparison of Background Radiance Estimation Methods.* In order to compare the performance of the three methods used to estimate the background radiance, four pixels through the plume were picked out. These pixels, belonging

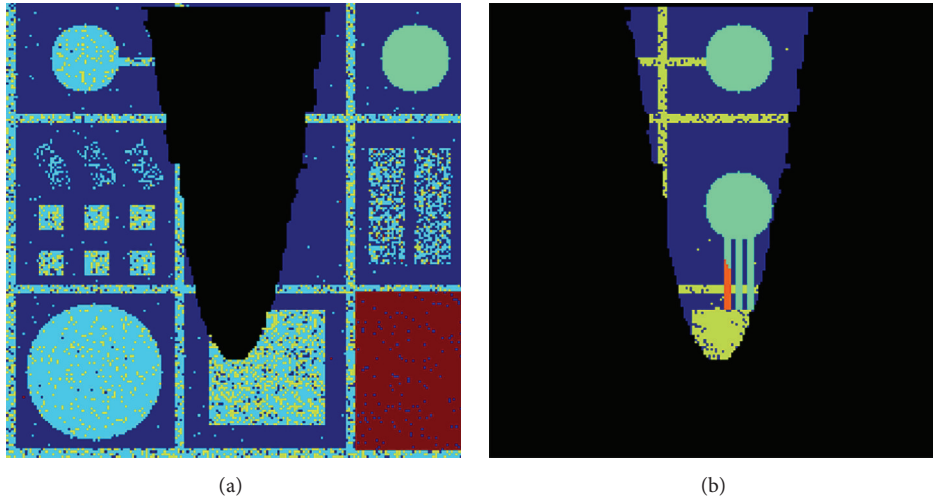


FIGURE 8: Classification results on the synthetic refinery scene. (a) Plume-absent region. (b) Plume-present region.

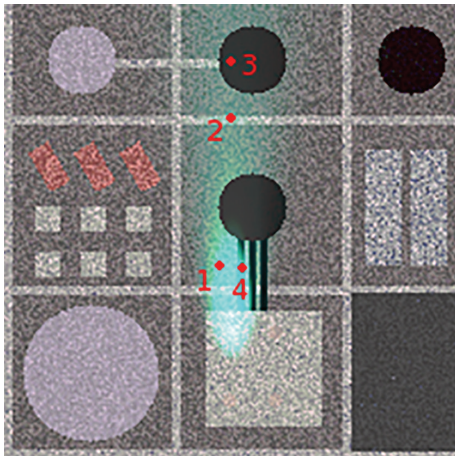


FIGURE 9: Positions of used pixels in the background radiance estimation methods comparison.

to different classes derived from the classification (see Section 3.2.2), are figured hereafter in Figure 9. The ground of these pixels is composed, respectively, of brown sandy loam, asphalt, aluminum, and copper.

Figure 10 summarizes the results of background radiance estimation using the three methods: SB, CB, and CSB. For each of the selected pixels are represented the on-plume radiance (red), the real off-plume radiance (dotted green), and the estimation of  $L_{\text{bkg}}$  using SB (cyan), CB (blue), and CSB (magenta).

The cluster of brown sandy loam is the most present among plume-absent pixels. Thus, the background properties of the latter are strongly represented in the principal vectors derived from the PCA. It is therefore obvious that the SB method gives an accurate estimate of the background radiance for pixels of this cluster (Figure 10(a)).

Furthermore, the background radiances of asphalt cluster pixels are pretty close to the background radiances of brown

sandy loam cluster pixels. That is why  $L_{\text{bkg}}$  estimate given by SB approach remains rather effective for this cluster (Figure 10(b)).

Nonetheless, reflective materials clusters have a background radiance much far from the main plume-absent cluster, which affects significantly the accuracy of the background radiance estimation using SB, as we notice in Figures 10(c) and 10(d).

We observe in these two last figures that, for such materials, SB method reproduces approximately the high frequency variations. However, there is a component similar to the main cluster background radiance, which adds up to the estimation.

These curves indicate at one hand that the Selected-Band approach yields an accurate estimate of the background radiance, for the pixels of the most represented class among plume-absent pixels. But on the other hand, for other classes, the less the class is represented outside the plume, the less its background radiance is correctly estimated. From these observations, we deduce that SB method does not manage well the case of heterogeneous background estimation.

Figure 10 shows that the introduction of a classification to the background radiance estimation process improves the results, especially for the minority classes of the scene. For those pixels (Figures 10(c) and 10(d)), the two classification-based methods (CB and CSB) give a more accurate estimation than SB does.

One can note that, for pixel 4, there is a slight difference between the real  $L_{\text{bkg}}$  radiance and the estimated one using CB or CSB. This difference comes from the fact that the class #4 is not represented at all in the plume-absent region. Thus, it is assimilated during the classification with the class #3.

Regarding to the pixels 1 and 2, the results of the method CB are less specific than those of the SB method. Indeed, CB method does not take into account the intraclass variability by assimilating to each plume-present pixel the mean radiance of plume-absent pixels belonging to the same class of the latter. To this limitation, we must add the errors due to

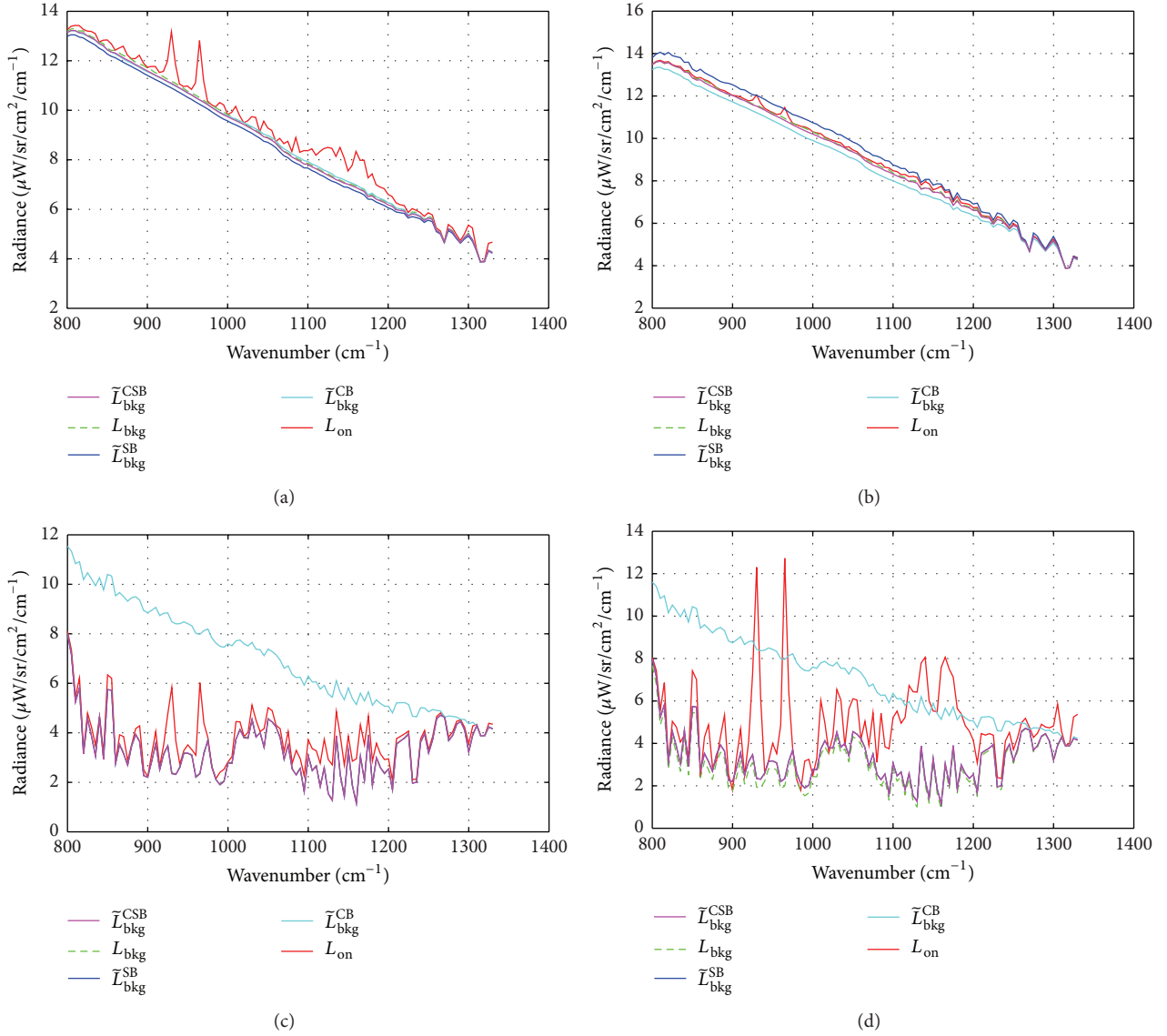


FIGURE 10: Comparison of background radiance estimation methods, for four different pixels through the plume. The red curves stand for the on-plume radiances; the dotted green ones are the real background radiances. The cyan, blue, and magenta curves represent, respectively, the background radiance estimated by the SB, CB, and CSB methods. (a) Results for pixel 1 (brown sandy loam), (b) results for pixel 2 (asphalt), (c) results for pixel 3 (aluminum), and (d) results for pixel 4 (copper).

the missclassification. Despite these two sources of errors, the CB background radiance estimation is still acceptable.

Concerning the CSB method, the estimation coincides perfectly with the real background radiance, for those pixels. This method manages well the intraclass variability.

In order to have a spatial visualization of the estimation error of the three compared methods, we illustrated in Figure 11 the mean error of background radiance estimation. This mean error was expressed in terms of brightness temperature.

Figure 11 upholds the undermentioned results. As expected, with the SB approach, we obtain a mean error less than 5 K for the classes which are the most represented among plume-absent pixels (#1 and #2). This result confirms the efficiency of the approach on homogeneous scene. However,

for the two other classes, which are poorly (#3) or not (#4) represented among the plume-absent pixels, we reach more than 45 K of error.

In the case of Clustering-Based methods, the mean error obtained for the minority clusters is far smaller than the error gotten with SB approach. Through class #4 the mean error is less than 4.5 K, both for CB and CSB methods, despite the fact that the latter is not represented among the plume-absent pixels.

For the other classes, even class #3 which presents more than 35 K of error with the SB approach, we hardly reach less than 2.5 K of error (CSB method). With the CB method, some pixels have a mean error reaching 5.5 K, but those pixels are very few.

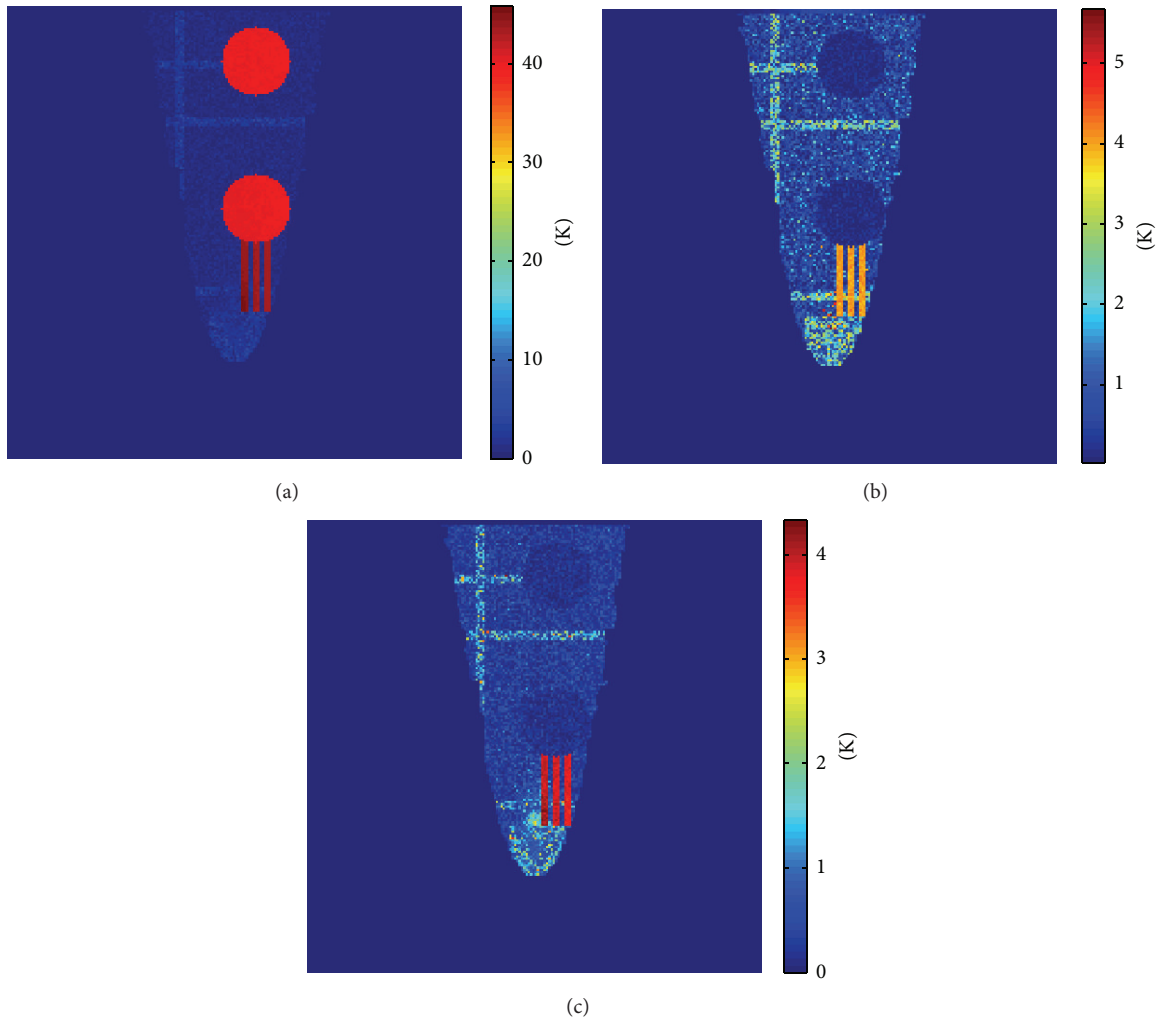


FIGURE 11: Mean error of background radiance estimation, expressed in terms of brightness temperature. (a) Mean error obtained with the Selected-Band estimation method. (b) Mean error obtained with the Clustering-Based estimation method. (c) Mean error obtained with the Clustering-Based Selected-Band estimation method.

To assess the overall performance of these three methods, the average error was calculated over the plume. As expected, the CSB method is the best of the three methods: the mean error obtained over the plume is equal to 0.48 K. With the CB method, the mean error remains low; it equals 0.80 K. However, the SB method gives a mean error of 9.55 K over the plume. This is explained by the large error of estimation for classes #3 and #4.

After carrying out the three methods on synthetic data, we can conclude that CSB approach provides better results than CB and SB approaches, particularly regarding materials not well, or not at all, represented among the plume-absent pixels.

## 4. Application on Real Data

*4.1. Presentation of Telops Hyper-Cam Acquisition.* The Telops Hyper-Cam LW is a lightweight and compact imaging instrument which uses Fourier Transfer Infrared (FTIR)

technology. The spectral resolution is user-selectable up to  $0.25 \text{ cm}^{-1}$  over the  $7.7$  to  $11.7 \mu\text{m}$  spectral range. The ground-based Telops Hyper-Cam is installed on a stabilization platform equipped with a global positioning system (GPS) and inertial motion unit (IMU). In a FTS imaging system, signal modulation is achieved using a Michelson interferometer. Acquiring a full interferogram typically lasts about one second. Therefore, an image motion compensation mirror uses GPS/IMU data to compensate efficiently for the aircraft movements during data acquisition.

This flight was carried out using a Hyper-Cam LW sensor at an altitude of 685 meters and a speed of 110 knots leading to a ground pixel size of  $0.057 \text{ m}^2/\text{pixel}$ . A spectral resolution of  $6 \text{ cm}^{-1}$  was used which gives a total of 90 spectral bands equally spaced over the whole range cover by the focal plane array detector. Outside temperature, wind speed, and relative humidity at ground level were  $21^\circ\text{C}$ ,  $15 \text{ km/h}$ , and  $37\%$ , respectively.

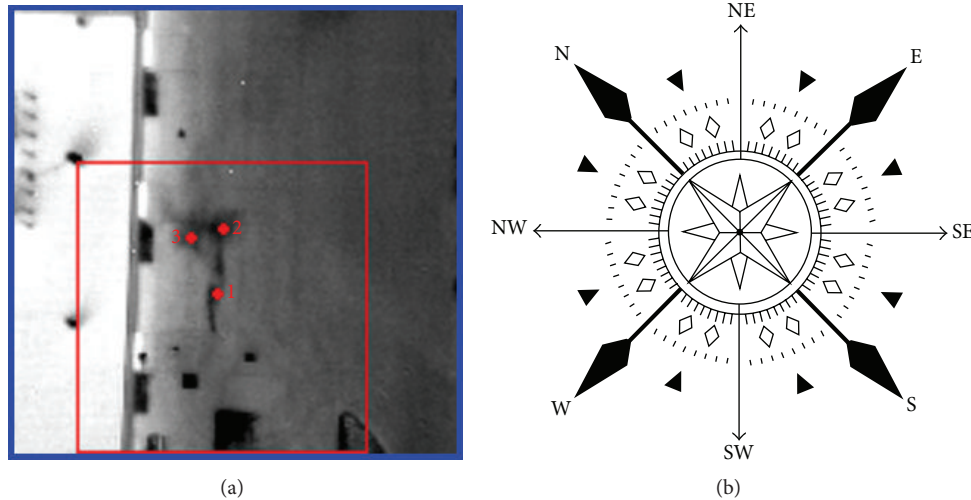


FIGURE 12: Illustration of subimage and pixels used in the background radiance estimation methods comparison.

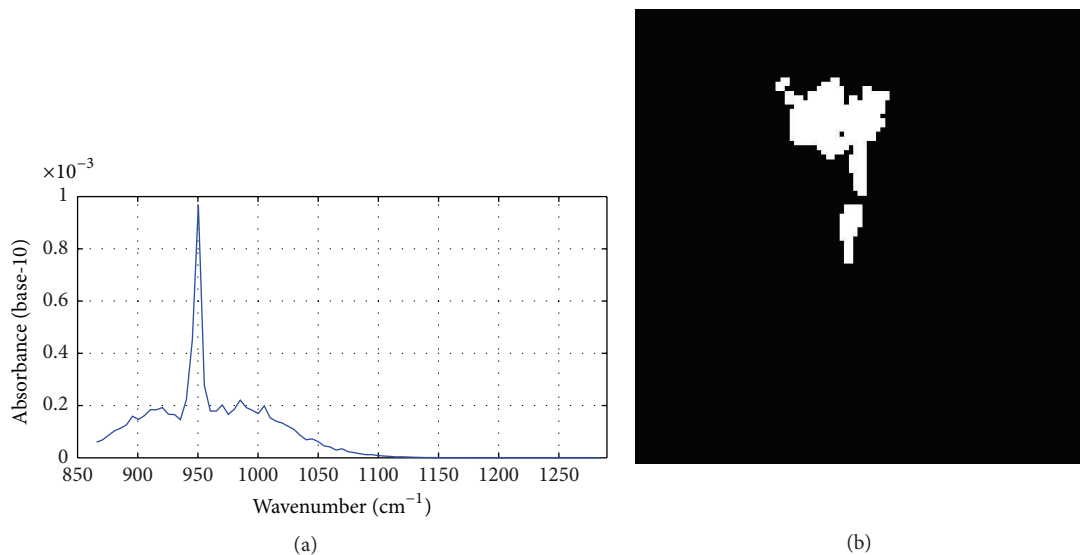


FIGURE 13: Ethylene release detection. (a) Absorptive coefficient spectrum of ethylene (from PNNL). (b) Plume detection mask for Telops parking scene.

Airborne hyperspectral infrared measurements were carried out above a pure ethylene gas released. Ethylene is a flammable gas massively used worldwide in the production of many polymer materials. During this experiment, gas was released at a constant flow rate of approximately 20 L/min.

**4.2. Ground Radiance Estimation.** Since the ethylene plume covers a ground composed entirely of asphalt, we reduced the size of the image to be processed, in order to limit the number of classes obtained in the plume-absent area. This  $100 \times 100$  subimage is represented by the red square in Figure 12.

**4.2.1. Ethylene Presence Detection.** The SMF algorithm was applied on the Telops acquisition in order to define the ethylene release spatial extension. The ethylene's absorbance

curve, illustrated in Figure 13(a), was used to model the target vector  $\mathbf{T}$  (see Section 2.1).

A plume mask (Figure 13(b)) is obtained after the application of a threshold on the abundances image  $\alpha$ . In addition, we performed a morphological opening operation, in order to take away the detection artifacts.

Unfortunately the applied morphological opening removes some plume-present pixels, which are localized at the frontier of the plume.

**4.2.2. Classification of Telops parking Scene.** As opposed to the synthetic scene case, we cannot have a quantitative evaluation of the classification. Thus, only a qualitative description of it is given thereafter.

On this acquisition performed around 11 a.m., one can notice the presence of a temperature gradient along the

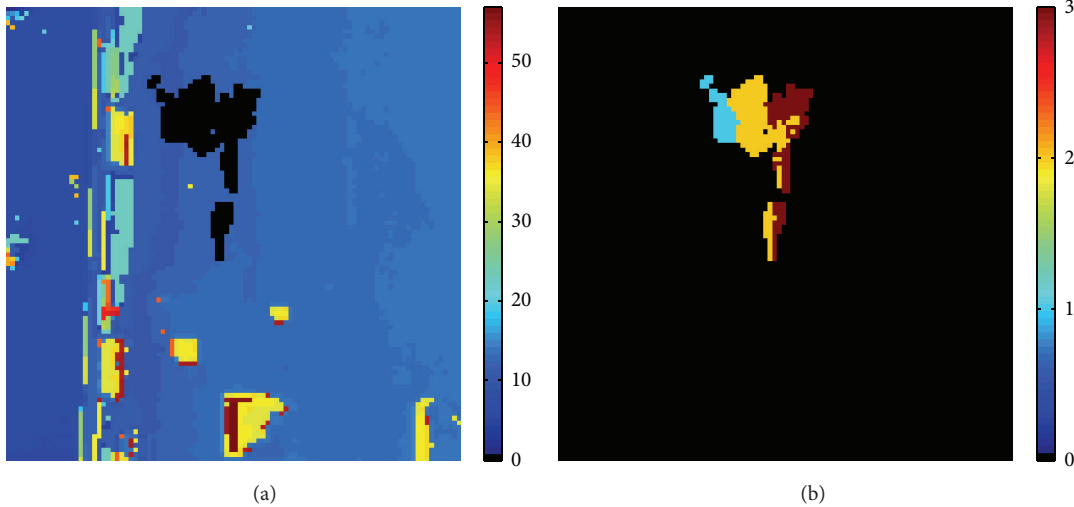


FIGURE 14: Classification results on Telops parking scene. (a) Plume-absent region. (b) Plume-present region.

southeast to northwest direction. Indeed, the sun, while rising in the sky, heated gradually the scene. Thus, even if two pixels are composed from the same material, they could have two different ground temperature, according to their location in the scene. Consequently, those pixels should be classified into two different clusters.

Figure 14 shows the classification results obtained on Telops' parking scene. The classification on the plume-absent region is illustrated in Figure 14(a), while the classification involving the plume-present region is illustrated in Figure 14(b).

The plume-present region was clustered into 3 classes, while the plume-absent region was clustered into 57 classes.

From these two figures, we notice that the classification complies with the temperature gradient. Note however that the classification in the plume-present region is more accurate than the second classification. Indeed, the plume-absent classes corresponding to the plume-present classes #2 (yellow) and #3 (brown) were merged into the same class. This can be explained by the fact that we used a threshold on the size of class ( $D_{\max}$ ) higher in the plume-absent case, in order to reduce the number of classes.

**4.2.3. Comparison of Background Radiance Estimation Methods.** For this scene, we do not have any *a priori* knowledge of the background radiance. But, by observing the scene, we can notice that it seems to be homogeneous along the vertical direction. In other words, it is justified to assume that  $L_{\text{bkg}}$  is vertically constant. Hence, for a given plume-present pixel, we approximate its background radiance by the mean spectra of some plume-absent pixels located at the same column than the latter. This radiance will be designated by the term  $\langle L_{\text{off}} \rangle$ .

Figure 15 shows the results of background radiance estimation using the three methods: SB, CB, and CSB. For the three selected pixels, we figured the on-plume measured radiances (red curve), the expected off-plume radiances (dotted green curve), and the estimation of  $L_{\text{bkg}}$  using SB (cyan), CB (blue), and CSB (magenta).

The first point we can deduce from Figure 15 is the relevance of the radiance  $\langle L_{\text{off}} \rangle$  to model the background radiance. One can notice that it agrees quite well with the on-plume radiance on bands where the absorbance of ethylene is close to zero. Moreover, the difference between  $\langle L_{\text{off}} \rangle$  and  $L_{\text{on}}$  on bands of ethylene absorption follows the same variation then the absorption curve of ethylene.

For the three chosen pixels, the background radiance estimation obtained by both CB and CSB methods is rather consistent with  $\langle L_{\text{off}} \rangle$ . Nonetheless, the SB estimate does not match well with the expected radiance. For pixels #1 and #2 SB approach underestimates the background radiance, while it overestimates  $L_{\text{bkg}}$  for pixel #3.

Those estimation errors are distributed over the whole spectral range. They are more important for ethylene absorption features.

So as to get an idea of the error magnitude for each method, two parameters measuring this error with respect to the expected radiance were defined: the root mean square of the brightness temperature error ( $\sigma_{T_b}$ ) is calculated, for each pixel, as follows:

$$\sigma_{T_b} (\text{K}) = \sqrt{\frac{1}{N_B} \cdot (\overline{T_{\text{bkg}}} - \langle T_{\text{off}} \rangle) \cdot (\overline{T_{\text{bkg}}} - \langle T_{\text{off}} \rangle)^T}, \quad (10)$$

where  $\overline{T_{\text{bkg}}}$  is the background brightness temperature estimated by one of the three methods, for the concerned pixel.  $\langle T_{\text{off}} \rangle$  is the expected background brightness temperature, for pixel in question.

Moreover, we define the relative root mean square error on radiance ( $\sigma_L$ ) by

$$\sigma_L (\%) = \sqrt{\frac{1}{N_B} \cdot \left( \frac{\overline{L_{\text{bkg}}} - \langle L_{\text{off}} \rangle}{\langle L_{\text{off}} \rangle} \right) \cdot \left( \frac{\overline{L_{\text{bkg}}} - \langle L_{\text{off}} \rangle}{\langle L_{\text{off}} \rangle} \right)^T}, \quad (11)$$

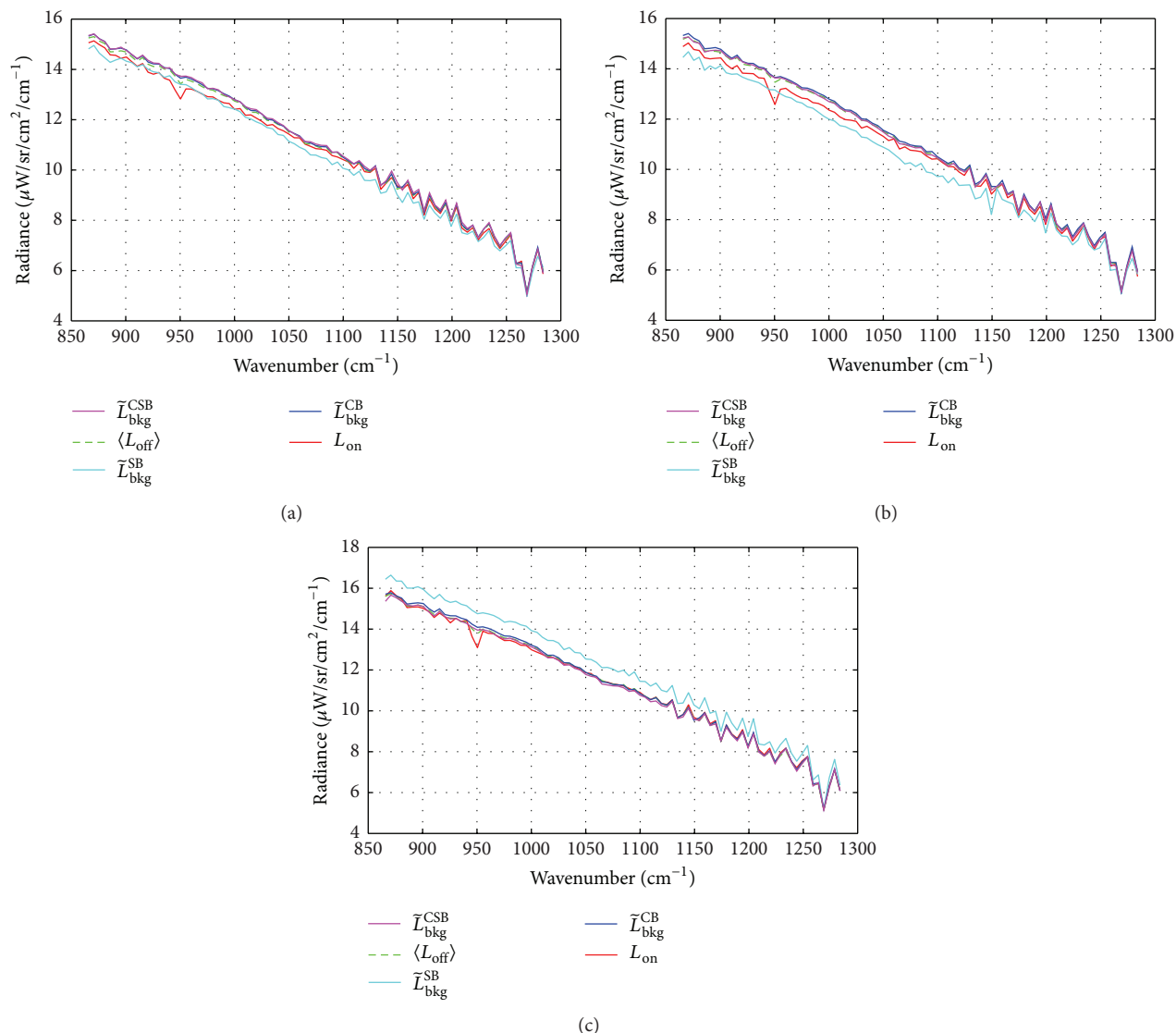


FIGURE 15: Comparison of background radiance estimation methods, for three different pixels through the plume. The red curves stand for the on-plume radiances; the dotted green ones are the expected background radiances. The cyan, blue, and magenta curves represent, respectively, the background radiance estimated by the SB, CB, and CSB methods. (a) Results for pixel 1, (b) results for pixel 2, and (c) results for pixel 3.

where  $\widetilde{L}_{\text{bkg}}$  is the background radiance estimated by one of the three methods, for the concerned pixel.

We figured the obtained results, for each of the three pixels, in Table 2.

Table 2 validates the conclusions deduced from Figure 15. The SB method gives a less accurate estimation than the Clustering-Based methods. If for pixel #1, the mean error calculated is three times higher with the SB method, it becomes ten times higher for pixels #2 and #3. Otherwise, the CB method has a background radiance estimation almost as similar as the CSB method estimation. Beside for pixel #1, the estimation obtained by the CB method is better than that obtained by CSB method. Moreover, the average error of all plume-present pixels is equal to 0.64 K for the CB method, while it is equal to 0.68 K for the CSB method. However the two methods remain of the same order of magnitude.

Recall, nevertheless, that  $\langle L_{\text{off}} \rangle$  is just an approximation of the real  $L_{\text{off}}$ . Thus, the result presented below does not induce necessarily that CB method is better than CSB method.

Figure 16 illustrates a comparison of different radiances at the ethylene most absorptive band ( $950.4 \text{ cm}^{-1}$ ), for pixels along a horizontal cross section. Pixels from 35 to 55 are plume-present pixels. Therefore, the radiances comparison is restricted to those pixels.

Figure 16 shows that the SB approach miscalculates the background radiance, comparing to the other methods. On a part of plume-present pixels, it overestimates  $L_{\text{bkg}}$ , while it underestimates this term on the other parts of plume-present pixels. The estimation error reaches at most 10% for this band. Recall that this band is the most important for the ethylene quantification (see Figure 13(a)).

TABLE 2: Evaluation of the difference between expected background radiance and estimated background radiance, using one of the three methods used in this paper. The first table presents the root mean square of the brightness temperature error ( $\sigma_{T_b}$ ), while the second summarizes the results in terms of the relative root mean square error on radiance ( $\sigma_L$ ).

(a)			
$\sigma_{T_b}$ (K)	Selected pixels		
	1	2	3
SB	1.96	3.32	3.94
CB	0.36	0.44	0.46
CSB	0.5	0.29	0.4

(b)			
$\sigma_L$ (%)	Selected pixels		
	1	2	3
SB	3.1	5.06	6.21
CB	0.55	0.69	0.68
CSB	0.95	0.5	0.67

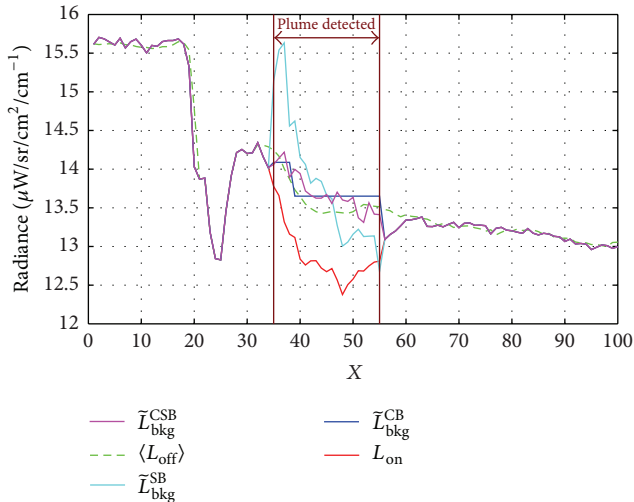


FIGURE 16: Comparison of different radiances at the ethylene absorptive band ( $950.4\text{ cm}^{-1}$ ), along a horizontal cross section containing some plume-present pixels. The red curve stands for the on-plume radiances; the green dotted one is the expected background radiances. The cyan, blue, and magenta curves represent, respectively, the background radiances estimated by the SB, CB, and CSB methods.

As expected, the radiance estimated using CB method is a constant piecewise function. We can see that, for the first class (from the left), the estimated radiance is consistent with the mean of the expected radiance ( $\langle L_{\text{off}} \rangle$ ) of concerned pixels. But for the second class, which is the result of merging of two classes (see Figure 14), the estimated radiance does not match perfectly with the mean of  $\langle L_{\text{off}} \rangle$ . Using a better classification of the plume-absent region, it is possible to sort this second class into two classes, which improves the estimation yielded by CB method.

In Figure 16, we observe that CSB method takes into consideration the intraclass variability, which allows getting better estimation with this method than CB method. For the concerned band, CSB method does not exceed 3% of estimation error.

In order to generalize those observations to the all plume-present pixels, we illustrated in Figure 17 a comparison of the background radiance estimation obtained by each of the three methods. This comparison is performed at the band  $950.4\text{ cm}^{-1}$ .

One can notice that at the frontier of the plume, some plume-present pixels have a relatively low radiance (dark pixels). This is due to a bad plume detection in this region as we already explained it above. For those pixels, the radiance represented in Figure 17 is  $L_{\text{on}}$  and not  $L_{\text{bkg}}$ .

Figure 17(a) shows that SB method overestimates the background radiance on a part of plume-present pixels (bright area of the plume). On another part of plume-present pixels,  $L_{\text{bkg}}$  is underestimated (dark area of the plume). This is due to the presence in the plume-absent region of more or less shiny materials than the plume-present pixels. The signal of those materials is then integrated in the principal components derived from the PCA.

The Clustering-Based methods use only the signal of plume-absent pixels having the same background properties than the plume-present pixels. The use of only pertinent information for the background radiance estimation therefore allows improving its accuracy.

This is clearly visible in Figure 17, since we note a certain homogeneity between the value of the plume-present and the plume-absent radiance.

**4.3. Gas Concentration Estimation.** From the scene described in Figure 12, we first compute an atmospheric compensation; then we apply a linear algorithm to estimate ethylene concentration for each background estimation.

Atmospheric compensation stage has two goals: first it aims to avoid the introduction of a probable bias from atmospheric nontarget gases on the retrieval; then it allows the estimation of the atmospheric ground level temperature and water vapor concentration. We assume here that atmosphere properties are homogeneous over the scene. We applied a Spectral Smoothness (SpSm) algorithm [28, 29] on a homogeneous subimage to estimate atmospheric profiles (temperature, water vapor), surface emissivity, and surface temperature.

The SpSm algorithm from a set of initial guess is used to reduce retrieved emissivity spectral variability on homogeneous area of concrete material. The initial set is composed with an atmospheric profile of temperature and water vapor from “Quebec meteorological center” fitted with local measurement (294.15 K for atmospheric ground temperature and 37% for relative humidity) and ground temperature obtained from the highest value of spectral brightness temperature measured on the scene. We use 150 tiny variations of atmospheric profiles and 150 different ground level temperatures to find the optimal set of parameters which leads to low spectral variation of retrieved spectral emissivity. For this concrete subimage the corresponding retrieved spectral emissivity is

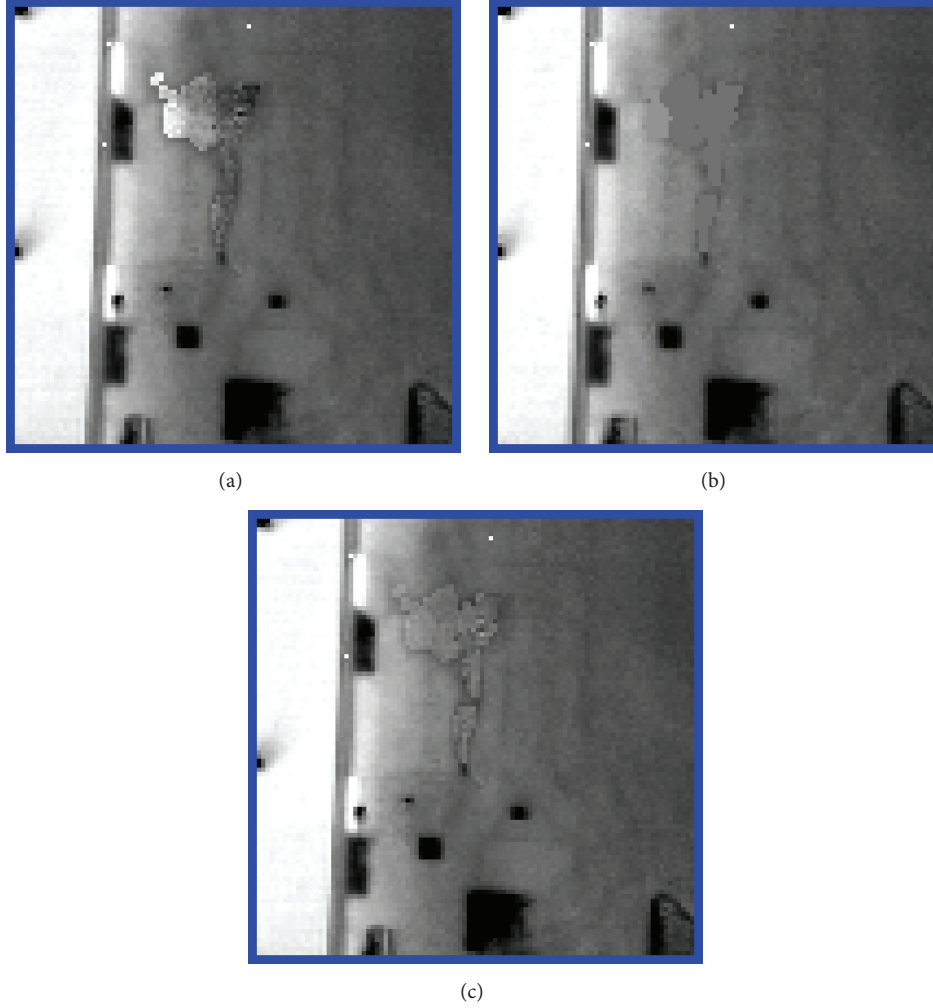


FIGURE 17: Comparison of the three background radiance estimations according to the band  $950.4 \text{ cm}^{-1}$ , where the ethylene absorbance is the most important. (a) Selected-Band approach. (b) Clustering-Based method. (c) Clustering-Based Selected-Band method.

shown in Figure 18. The corresponding ground temperature, ground level atmospheric temperature, and water vapor concentration are, respectively, 316.5 K, 296.6 K, and 10200 ppm.

From this atmospheric profile we compute atmospheric transmission and atmospheric radiance used for the atmospheric correction pixel by pixel.

Finally, the simple quantification algorithm used is from a linear model of the differential signature:

$$\Delta \mathbf{L} = \mathbf{L}_{\text{on}} - \mathbf{L}_{\text{off}} = \rho \cdot \mathbf{A}(\lambda) \cdot (\mathbf{B}(\mathbf{T}_{\text{plume}}, \lambda) - \mathbf{L}_{\text{off}}), \quad (12)$$

where  $\mathbf{T}_{\text{plume}}$  is the plume temperature,  $\rho$  is the column integrated concentration (ppm-m), and  $\mathbf{B}(\mathbf{T}, \lambda)$  is the Planck function. One can estimate the concentration applying for each pixel by the following equation:

$$T = \mathbf{A}(\lambda) \cdot (\mathbf{B}(\mathbf{T}_{\text{plume}}, \lambda) - \mathbf{L}_{\text{off}}), \quad (13)$$

$$\rho = \frac{\mathbf{T}^T \Sigma_{\mathbf{X}}^{-1} \Delta \mathbf{L}}{\mathbf{T}^T \Sigma_{\mathbf{X}}^{-1} \mathbf{T}}.$$

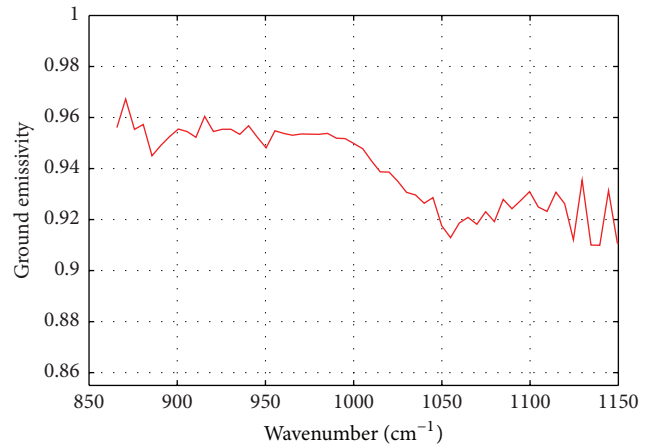


FIGURE 18: Mean ground spectral emissivity retrieved through the subimage.

Plume temperature is assumed to be homogeneous and equal to ground level atmospheric temperature estimated

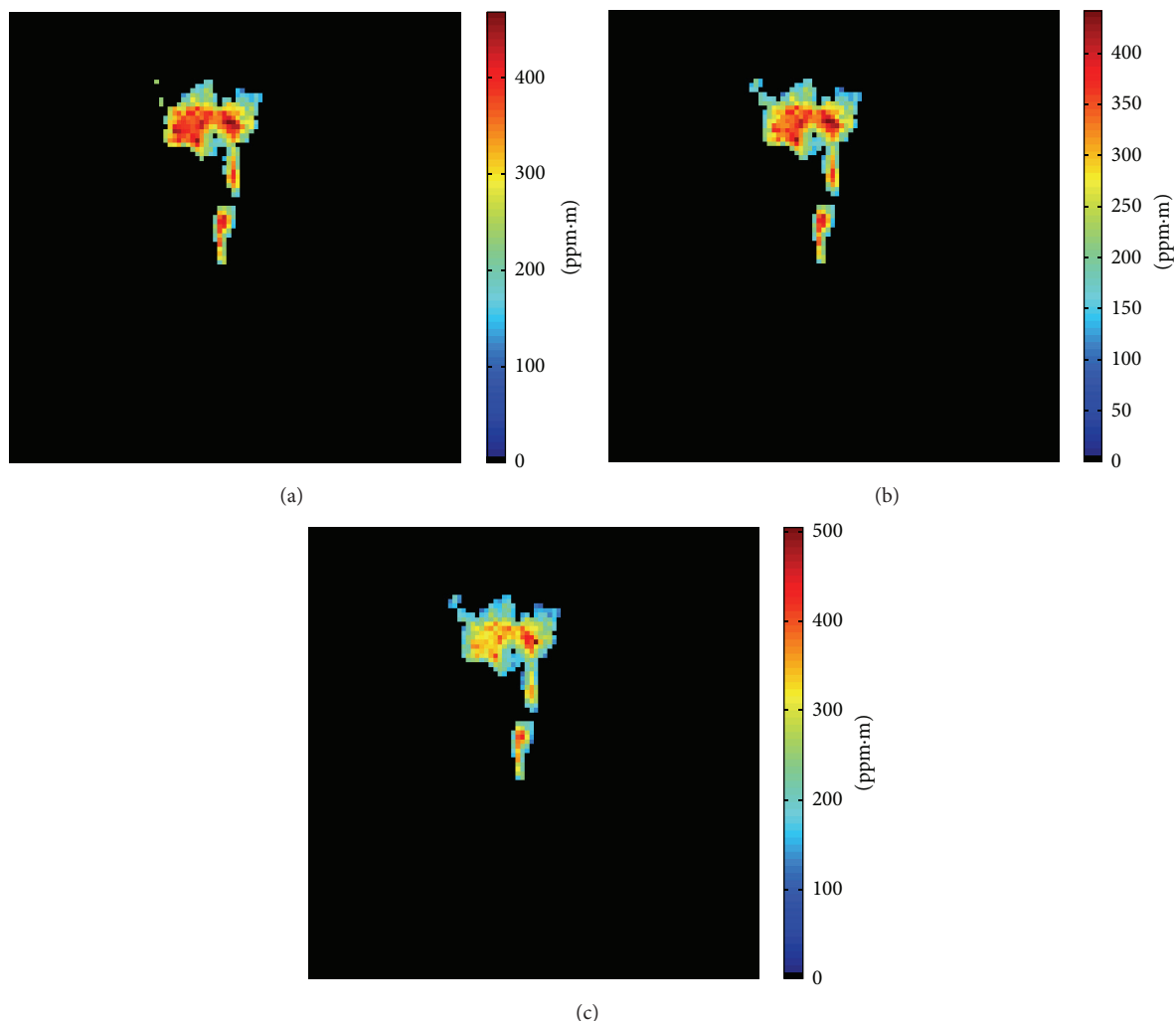


FIGURE 19: Retrieved ethylene concentration (ppm·m) from the three estimated  $L_{\text{off}}$  images. (a) Selected-Band approach. (b) Clustering-Based method. (c) Clustering-Based Selected-Band method.

to be 296.65 K. One can notice that neither pixel-by-pixel emissivity nor ground temperature is needed here to estimate gas concentration.

The different stages described above are applied to the estimated  $L_{\text{off}}$  images shown in Figure 17.

Figures 20 and 19 shows ethylene concentration retrieved from Hyper-Cam data using the three estimated background methods outlined above and their differences. The mean retrieved integrated concentration is about 200 ppm by CSB method. One can notice that ground radiance main differences are translated into retrieved concentration differences. In particular, the upper left corner of the plume where the background radiance was overestimated by about 10% by SB method leads to the highest differences in concentration (up to 200 ppm·m). Then, class borders used for CB method where radiance difference was the highest with CSB method lead to local differences of about 40 ppm·m. The mean difference between CB and CSB methods is less than 10% in concentration whereas it climbs up to 20% between SB and CSB methods. As pixel ground level size is about 23 cm

the plume mean width size  $l$  orthogonal to wind direction is calculated to 4 m and average mass in one-meter long slice of the plume is calculated to be 0.986 g assuming ethylene molar weight  $w_m$  of 28 g/mol. The flow rate  $d$  can be estimated to be 4.2 g/s assuming a wind speed value of 4.3 m/s and using the following equation where  $\rho$  (in ppm·m) is the mean integrated column concentration in an orthogonal slice of one meter thick and 4 m width. This results fits well with the true value of 20 L/min which corresponds to 3.15 g/s assuming that ethylene volume weight is 567.65200 kg/m<sup>3</sup>:

$$d = \rho \cdot l \cdot 10^3 \cdot \frac{w_m}{22.71}. \quad (14)$$

## 5. Summary and Conclusions

Gas trace plume remote sensing above industrial scene requires both high spectral and spatial resolution. Using airborne FTS imaging techniques it becomes possible to detect and quantify gas traces. However retrieval accuracy depends on both pixel-by-pixel background under plume

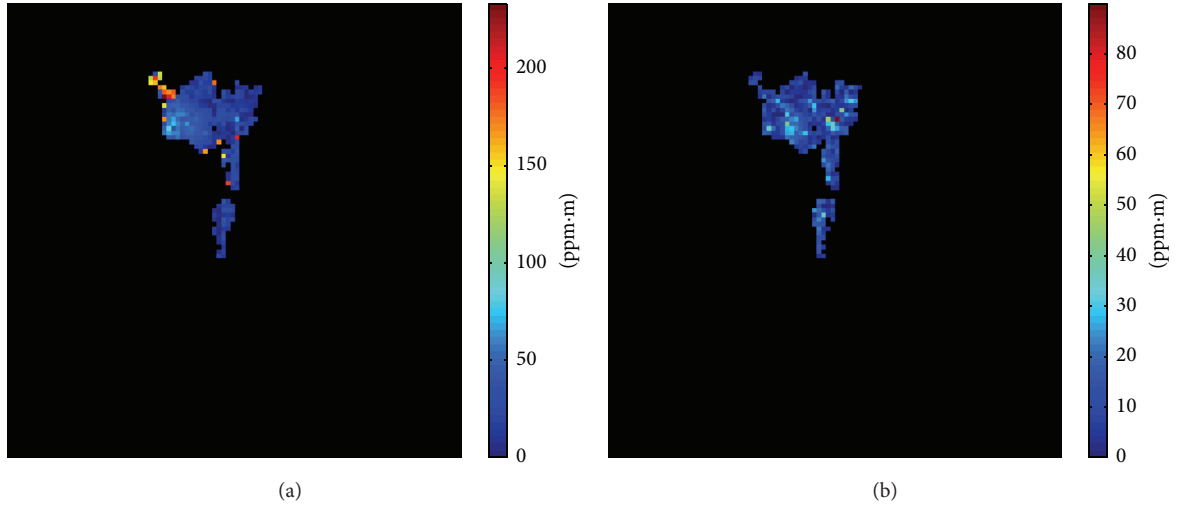


FIGURE 20: Comparison between retrieved concentration from the different approaches. (a) Difference between retrieved concentration from SB background estimation and CSB background estimation. (b) Difference between retrieved concentration from CB background estimation and CSB background estimation.

estimation and good enough spectral resolution around target gas absorption peak. In this paper we propose a method to estimate ground radiance pixel by pixel taking into account scene variability spectral behavior. The CSB method described above is a Clustering-Based method which aims to associate statistical spectral properties from classes nonimpacted by the plume to classes below the target gas plume. This method is based on SB method algorithm [18] extended to a clustering approach. We have shown that introducing an initial classification of the scene improves background radiance estimation for nonhomogeneous scene in comparison with classical SB method or simple Clustering-Based method. Results based on simulations show more than 10 K in brightness temperature for low emissivity material and up to 3 K for high emissivity material.

The CSB method applied to airborne Hyper-Cam LW data acquired above an ethylene release of 20 L/min shows that the CSB method can reduce background radiance uncertainty from 5 to 1% or from 3 to 1 K in terms of brightness temperature uncertainty, for a high emissivity material such as concrete. This improvement leads to a mean difference of about 10% on ethylene plume retrieved concentrations in this particular “easy” scene.

Finally we propose in this paper an end-to-end method using a single hyperspectral image to estimate (i) ground radiance and properties (emissivity and temperature); (ii) atmospheric ground level temperature and water vapor content; and (iii) trace gas plume concentration with an encouraging accuracy. Indeed the retrieved flow rate is close to mean flow rate during the gas release.

The method outlined above must now be tested on industrial scenes where expected improvement should be higher as it deals well with a very high number of materials, with intraclass variability such as shadow and temperature gradient and with low emissivity materials.

## Symbols

### Plume Detection

- $N$ : Number of pixels
- $N_B$ : Number of spectral bands
- $\mathbf{X}$ : Hyperspectral image matrix [ $N \times N_B$ ].  $\mathbf{X}$  could represent radiance ( $\mathbf{L}$ ) or brightness temperature ( $T_b$ )
- $\mathbf{x}$ : A pixel of  $\mathbf{X}$
- $\langle \mathbf{x} \rangle$ : Mean spectrum of  $\mathbf{X}$
- $\Sigma_{\mathbf{X}}$ : Covariance of  $\mathbf{X}$
- $\mathbf{T}$ : The gaseous target spectrum
- $\boldsymbol{\alpha}$ : Target fit coefficients (abundances)
- $\mathbf{d}$ : Residual vector.

### Selected-Band Approach

- $N_{\text{on}}$ : Number of plume-present pixels
- $N_{\text{off}}$ : Number of plume-absent pixels
- $N_{\text{SB}}$ : Number of selected bands
- $N_p$ : Number of the used principal components
- $L_{\text{on}}(\lambda)$ : On-plume radiance: measured radiance for a plume-present pixel
- $L_{\text{off}}(\lambda)$ : Off-plume radiance: measured radiance for a plume-absent pixel
- $L_{\text{bkg}}(\lambda)$ : Background (plume-free) radiance for a pixel.

### Classification

- $D_{\text{max}}$ : Threshold on the size of a class
- $N_C$ : Number of classes without plume
- $N_{\text{CP}}$ : Number of classes containing plume.

## Competing Interests

The authors declare that they have no competing interests.

## References

- [1] M. Schlerf, G. Rock, P. Lagueux et al., "A hyperspectral thermal infrared imaging instrument for natural resources applications," *Remote Sensing*, vol. 4, no. 12, pp. 3995–4009, 2012.
- [2] J. A. Hackwell, D. W. Warren, R. P. Bongiovi et al., "LWIR/MWIR imaging hyperspectral sensor for airborne and ground-based remote sensing," in *Imaging Spectrometry II*, vol. 2819 of *Proceedings of SPIE*, pp. 102–107, Denver, Colo, USA, November 1996.
- [3] Y. Ferrec, S. Théas, J. Primot et al., "Sieleters, an airborne imaging static fourier transform spectrometer: design and preliminary laboratory results," in *Proceedings of the Imaging and Applied Optics Congress*, Paper FMID-3, OSA, Arlington, Va, USA, June 2013.
- [4] D. W. Messinger, S. S. Shen, and P. E. Lewis, "Gaseous plume detection in hyperspectral images: a comparison of methods," in *Proceedings of the SPIE, Algorithms and Technologies for Multispectral, Hyperspectral, and Ultraspectral Imagery X*, vol. 5425, pp. 592–603, Orlando, Fla, USA, August 2004.
- [5] L. Chilton and S. Walsh, "Detection of gaseous plumes using basis vectors," *Sensors*, vol. 9, no. 5, pp. 3205–3217, 2009.
- [6] E. Hirsch and E. Agassi, "Detection of gaseous plumes in IR hyperspectral images using hierarchical clustering," *Applied Optics*, vol. 46, no. 25, pp. 6368–6374, 2007.
- [7] C. C. Funk, J. Theiler, D. A. Roberts, and C. C. Borel, "Clustering to improve matched filter detection of weak gas plumes in hyperspectral thermal imagery," *IEEE Transactions on Geoscience and Remote Sensing*, vol. 39, no. 7, pp. 1410–1420, 2001.
- [8] A. K. Thorpe, D. A. Roberts, P. E. Dennison, E. S. Bradley, and C. C. Funk, "Point source emissions mapping using the airborne visible/infrared imaging spectrometer (AVIRIS)," in *Proceedings of the 18th Annual Conference on Algorithms and Technologies for Multispectral, Hyperspectral, and Ultraspectral Imagery*, vol. 8390, Baltimore, Md, USA, April 2012.
- [9] C. M. Gittins, "Detection and characterization of chemical vapor fugitive emissions by nonlinear optimal estimation: theory and simulation," *Applied Optics*, vol. 48, no. 23, pp. 4545–4561, 2009.
- [10] N. B. Gallagher, B. M. Wise, and D. M. Sheen, "Estimation of trace vapor concentration-pathlength in plumes for remote sensing applications from hyperspectral images," *Analytica Chimica Acta*, vol. 490, no. 1-2, pp. 139–152, 2003.
- [11] S. J. Young, "Detection and quantification of gases in industrial-stack plumes using thermal-infrared hyperspectral imaging," Tech. Rep. ATR-2002(8407)-1, The Aerospace Corporation, 2002.
- [12] C. S. Turcotte and M. R. Davenport, "Gas plume quantification in downlooking hyperspectral longwave infrared images," in *Image and Signal Processing for Remote Sensing XVI*, vol. 7830 of *Proceedings of SPIE*, Toulouse, France, September 2010.
- [13] P. Heasler, C. Posse, J. Hylden, and K. Anderson, "Nonlinear Bayesian algorithms for gas plume detection and estimation from Hyper-spectral thermal image data," *Sensors*, vol. 7, no. 6, pp. 905–920, 2007.
- [14] S. Walsh, L. Chilton, M. Tardiff, and C. Metoyer, "Effect of the temperature-emissivity contrast on the chemical signal for gas plume detection using thermal image data," *Sensors*, vol. 8, no. 10, pp. 6471–6483, 2008.
- [15] N. B. Gallagher, B. M. Wise, and D. M. Sheen, "Error analysis for estimation of trace vapor concentration pathlength in stack plumes," *Applied Spectroscopy*, vol. 57, no. 6, pp. 614–621, 2003.
- [16] S. E. Golowich and D. G. Manolakis, "Cramer-Rao bounds for long-wave infrared gaseous plume quantification," *Optical Engineering*, vol. 53, no. 2, 2014.
- [17] J. Theiler, B. R. Foy, and A. M. Fraser, "Nonlinear signal contamination effects for gaseous plume detection in hyperspectral imagery," in *Defense and Security Symposium*, vol. 6233 of *Proceedings of SPIE*, 2006.
- [18] S. Niu, S. E. Golowich, V. K. Ingle, and D. G. Manolakis, "New approach to remote gas-phase chemical quantification: selected-band algorithm," *Optical Engineering*, vol. 53, no. 2, Article ID 021111, 2014.
- [19] S. W. Sharpe, R. L. Sams, T. J. Johnson, P. M. Chu, G. C. Roderick, and F. R. Guenther, "Creation of 0.10 cm<sup>-1</sup> resolution, quantitative, infrared spectral libraries for gas samples," in *Vibrational Spectroscopy-Based Sensor Systems*, vol. 4577 of *Proceedings of SPIE*, pp. 12–24, Boston, Mass, USA, October 2001.
- [20] S. W. Sharpe, T. J. Johnson, R. L. Sams, P. M. Chu, G. C. Roderick, and P. A. Johnson, "Gas-phase databases for quantitative infrared spectroscopy," *Applied Spectroscopy*, vol. 58, no. 12, pp. 1452–1461, 2004.
- [21] A. Hayden, E. Niple, and B. Boyce, "Determination of trace-gas amounts in plumes by the use of orthogonal digital filtering of thermal-emission spectra," *Applied Optics*, vol. 35, no. 16, pp. 2802–2809, 1996.
- [22] A. M. Baldridge, S. J. Hook, C. I. Grove, and G. Rivera, "The ASTER spectral library version 2.0," *Remote Sensing of Environment*, vol. 113, no. 4, pp. 711–715, 2009.
- [23] V. Masson, L. Gomes, G. Pigeon et al., "The Canopy and Aerosol Particles Interactions in TOulouse Urban Layer (CAPITOUL) experiment," *Meteorology and Atmospheric Physics*, vol. 102, no. 3-4, pp. 135–157, 2008.
- [24] C. Miesch, L. Poutier, V. Achard, X. Briottet, X. Lenot, and Y. Boucher, "Direct and inverse radiative transfer solutions for visible and near-infrared hyperspectral imagery," *IEEE Transactions on Geoscience and Remote Sensing*, vol. 43, no. 7, pp. 1552–1561, 2005.
- [25] D. J. Carruthers, R. J. Holroyd, J. C. R. Hunt et al., "UK-ADMS: a new approach to modelling dispersion in the earth's atmospheric boundary layer," *Journal of Wind Engineering and Industrial Aerodynamics*, vol. 52, pp. 139–153, 1994.
- [26] J. R. Schott and C. Y. Chang, "Synthetic image generation of chemical plumes for hyperspectral applications," *Optical Engineering*, vol. 39, no. 4, pp. 1047–1056, 2000.
- [27] J. R. Landis and G. G. Koch, "The measurement of observer agreement for categorical data," *Biometrics*, vol. 33, no. 1, pp. 159–174, 1977.
- [28] C. C. Borel, "Surface emissivity and temperature retrieval for a hyperspectral sensor," in *Proceedings of IEEE Conference on Geoscience and Remote Sensing*, pp. 504–509, IEEE, July 1998.
- [29] K. Kanani, L. Poutier, F. Nerry, and M. P. Stoll, "Directional effects consideration to improve out-doors emissivity retrieval in the 3–13 μm domain," *Optics Express*, vol. 15, no. 19, pp. 12464–12482, 2007.

## Research Article

# Optical Estimation on Pollution Level of Respirable Dust Based on Infrared Transmitting Behavior in Coalmine Fully Mechanized Working Face

Wen-Zheng Wang,<sup>1,2</sup> Yan-Ming Wang,<sup>1,2</sup> and Guo-Qing Shi<sup>1,2</sup>

<sup>1</sup>Key Laboratory of Coal Methane and Fire Control, Ministry of Education, China University of Mining and Technology, Xuzhou 221116, China

<sup>2</sup>School of Safety Engineering, China University of Mining and Technology, Xuzhou 221116, China

Correspondence should be addressed to Yan-Ming Wang; [cumtwangym@163.com](mailto:cumtwangym@163.com)

Received 22 January 2016; Revised 9 March 2016; Accepted 20 March 2016

Academic Editor: Arnaud Cuisset

Copyright © 2016 Wen-Zheng Wang et al. This is an open access article distributed under the Creative Commons Attribution License, which permits unrestricted use, distribution, and reproduction in any medium, provided the original work is properly cited.

Respirable coal particle generated during underground mining is the main cause for gas-dust explosions and coal workers' pneumoconiosis (CWP) which needs accurate monitoring especially on its concentration. Focusing on the coal dust pollution in the fully mechanized working face of Huangbaici coalmine, coal particle was sampled for further industrial analysis and FT-IR test to obtain its chemical composition and optical constant. Combined with the simulated spatial distribution of airborne dust, the spectral transmission characteristics of coal dust within wavelengths of 2.5 to 25  $\mu\text{m}$  under different operating conditions were obtained. The simulation results show that the transmittance and aerosol optical depth (AOD) of coal dust are closely linked and obviously influenced by the variation of dust generation source (intensity of dust release, position of coal cutting, and the wetting of the coal seam) and airflow field (wind speed and direction of ventilation). Furthermore, an optical channel of 1260–1280  $\text{cm}^{-1}$  (7.937–7.813  $\mu\text{m}$ ) which is almost only sensitive to the variation of dust concentration but dull to the diameter change of coal dust was selected to establish the correlation of dust concentration and infrared transmittance. The fitting curve was then applied to retrieve the equivalent dust concentration based on optical information, and the comparison results demonstrate that the estimated pollution level is consistent with field measurement data in engineering practice.

## 1. Introduction

With the development of coal cutting mechanisms and ventilation technology, an increasing amount of coal is extracted from underground mines. A significant amount of coal dust is generated and dispersed into the mine atmosphere during coal crushing, extracting, exploding, and conveying in mining operations with the flow of the mine ventilation system [1–3]. Epidemiological studies have shown that exposure to coal dust is the main reason of coal workers' pneumoconiosis (CWP) [4]. Meanwhile, the presence of coal dust can be a serious explosion threat to coal mines which can cause a gas-dust explosion or coal dust explosion under certain conditions of temperature, oxygen concentration, and physical and chemical properties with or without methane

[5]. The threat of coal dust is closely linked to the coal dust concentration in the whole working face which needs to be monitored continuously. Thousands of lives are lost because of coal dust related accidents every year in underground mines in China [6, 7]. Hence, it is critical to strengthen the theoretical and experimental research on the monitoring of dust concentration in underground coal mines to evaluate coal dust pollution in fully mechanized working face of coal mine.

Numerous studies have been carried out on the behavior of dust in a mine atmosphere; two main approaches are generally adopted to investigate the dust distribution in an underground coal mine, namely, field measurement and computer numerical simulation. The method of field measurement mainly depends on sampling and sampling analysis, which is

widely used for dust evaluation in an underground coal mine [8, 9]. However, the method of field measurement cannot monitor dust particles in real time in an underground coal mine. Meanwhile, it is difficult and costly for the field measurement method to give the variation of dust distribution under different working conditions and influencing factors. With the development of computer technology, computer numerical simulation in particular, the computational fluid dynamics (CFD) method has been widely used to study the dispersion and spatial distribution of dust particles in recent years [10]. Extensive CFD modeling work on dust dispersion in various workplaces in underground mines has been carried out considering different airflows, particle sizes, dust sources, and mechanisms of dust transport [11–13]. The numerical simulation results agree well with the field data, which can serve as a basis for evaluating and monitoring dust pollution in underground coal mines.

In recent years, particulate matter (PM) pollution in the open atmosphere has become more and more serious [14]. A great amount of research has been carried out to achieve accurate monitoring of PM, among which the optical detection technology is the most effective and widely used method [15, 16]. The attenuation and radiative transfer properties of PM including transmittance or aerosol optical depth can be obtained by satellite and ground-based optical remote sensing detection technologies which can be used as the optical signal to evaluate PM pollution [17]. The fully mechanized working face of the coal mine is a relatively confined cubic space that has a length that ranges from one hundred meters to thousands of meters; the optical sensing method can be modified and then adopted to monitor coal dust pollution in fully mechanized working face.

Nowadays, some portable instantaneous monitoring equipment and methods were used to evaluate dust pollution mainly based on the absorption and scattering properties of dust particle system in underground mine [18]. These kinds of portable monitoring equipment and methods mainly consider the dust particle system to be homogeneous and uniform in its detection space [19, 20]; actually, the dust concentration and diameter distribution are nonuniform which varies obviously especially in the whole fully mechanized working face. Meanwhile, the monitoring of dust particles through portable monitoring equipment is discrete and discontinuous. It is necessary to strengthen the study on the radiation and transfer characteristics of dispersion coal dust to achieve the accurate and real-time optical monitoring in the whole fully mechanized working face.

In this study, aiming at the coal dust pollution in the fully mechanized working face of Huangbaici coal mine which is located in Wuda coalfield, northwest China, the CFD method was adopted to simulate the spatial distribution of coal dust under different dust sources and airflow fields. Combined with Mie scattering and heat flux method, the radiation properties and transmission characteristics of coal dust in the fully mechanized working face of a coal mine under different influence factors were obtained and analyzed. Further spectral analysis was conducted to select the optical

channel for dust concentration evaluation and finally an evaluation method of dust concentration in the fully mechanized working face of Huangbaici coal mine was presented.

## 2. Spatial Distribution of Coal Dust Hazard

*2.1. Field Condition and Model Configuration.* The Huangbaici coal mine in our study is located in the Wuda Coal District of Inner Mongolia Autonomous Region, northwest China [21]. The Wuda District holds a large amount of coal reserve which consists of coal-bearing strata of Pennsylvanian and Permian ages. Approximately, 80% of the coal mined in China comes from Pennsylvanian coal seams including Pennsylvanian Benxi Formation, the Pennsylvanian Taiyuan Formation, the Early Permian Shanxi Formation, and Xiashihezi Formation and the Late Permian Shangshihezi Formation [22, 23]. The fully mechanized working face of Huangbaici in our study is located at the NO. 15 coal seam of Pennsylvanian Taiyuan Formation. The width and height of the fully mechanized working face are 4 and 3 m, respectively, while the length varies dynamically with the advance of coal mining activity. The coal cutting machine and numerous kinds of supporting equipment and cable trays operate at the same time to ensure the safety of coal mining activity.

Based on the field condition of the fully mechanized working face of Huangbaici coalmine, a geometric model was set up for CFD simulation. Because of the complex working equipment in fully mechanized working face, it is impossible to establish an exact geometric model. Thus, the geometric model was simplified to be a cuboid calculation area of  $100\text{ m} \times 4\text{ m} \times 3\text{ m}$ , a coal cutting machine of  $5\text{ m} \times 2\text{ m} \times 1.2\text{ m}$ , with the supporting equipment represented by four cylinders with heights of 4 m and diameters of 0.15 m.

The air-dust coupled flow mathematical description was established to study the dispersion and distribution of coal dust particles in a fully mechanized working face. Three-dimensional steady incompressible Navier-Stokes equations were adopted to describe the airflow in a mine atmosphere. The  $k-\varepsilon$  model of Reynolds was applied to describe the turbulence effect, ignoring heat transfer. Given that the airflow model was established, a discrete phase model (DPM) was adopted to take dust movement into account, tracking dust movement by solving a differential equation for a discrete second phase in Lagrangian time. The second phases are spherical particles that are dispersed in a continuous phase. This model considers the coupling effect between the phases and its impact on both the discrete phase trajectories and the continuous phase flow. Such mathematical model and equations have been established in our previous study [24].

*2.2. Simulation Performance and Result.* In order to determine the simulation parameter and validate our CFD simulation results, coal dust distribution in the fully mechanized working face of Huangbaici coal mine was measured and obtained by field measurement method. According to the GB5748-85 (determination method of dust in the air of workplace) jointly issued by the Ministry of Health and Ministry of

Labor and Personnel of China [25], the concentration of rock dust can be determined when rock dust was sampled based on the weight gain of membrane and the intake air volume into Filter Dust Analyzer as follows  $S = (W_2 - W_1)/Q_N$ , where  $S$  is the concentration of rock dust,  $W_1$  and  $W_2$  are the weight of membrane before and after sampling, and  $Q_N$  is the intake air volume into Filter Dust Analyzer. The dust concentration distribution along the fully mechanized working face at three heights (0.5 m, 1.5 m, and 2.5 m) was obtained. Meanwhile, the coal dust particle generated in coal cutting area was sampled to obtain its diameter distribution by further analysis in laboratory. The dust diameter distribution test was carried out by graded sieves with different mesh. The test results of dust diameter distribution by quality at the generation source in fully mechanized working face are as follows: 0–5  $\mu\text{m}$  (11.94%), 5–10  $\mu\text{m}$  (14.69%), 10–20  $\mu\text{m}$  (24.84%), and >20  $\mu\text{m}$  (48.53%).

Thus, a typical simulation based on the normal condition in underground working face was conducted whose main parameters and boundary conditions were determined as follows. The coal dust in the simulation was bituminous coal particles, whose diameter distribution by quality is 0–5  $\mu\text{m}$  (10%), 5–10  $\mu\text{m}$  (15%), 10–20  $\mu\text{m}$  (25%), 20–50  $\mu\text{m}$  (30%), and >50  $\mu\text{m}$  (20%) as tested in our experiment with a flow rate of 0.01 kg/s. The inlet boundary type was set to be a velocity inlet with a magnitude of 2.5 m/s. The direction of ventilation is positive. The coal cutting machine is 5 m away from the intake of working face. The outlet boundary type was set to be outflow. The DPM condition and shear condition of the walls were set to be rebound with a recovery coefficient of 0.25 and no slip, respectively.

By conducting the CFD simulation, the distribution of the coal dust concentration and diameter in the central axis (1.5 m high) along the fully mechanized working face was obtained. Since the dust diameter distribution is an important input in Mie scattering model, which needs integral processing for number density function as nonuniform particles as shown in (3) and (4), then, the Rosin-Rammler function which is widely used in the statistics of coalmine dust particles [26, 27] was adopted in our study. The diameter distribution of coal dust was represented by the Rosin-Rammler function  $W(D)$  [28];  $R^2$  is the correlation coefficient of the Rosin-Rammler function:

$$W(D) = 100 \exp(-\beta * D^n), \quad (1)$$

where  $W(D)$  is the Rosin-Rammler function representing the cumulative distribution of the quality of coal particles greater than a certain diameter  $D$  and  $\beta$  and  $n$  are the coefficients related to the diameter distribution of coal particles. The numerical results of coal dust dispersion were shown in Table 1.

The dust diameter distribution at every sampling point was fitted to Rosin-Rammler function which can be further used in Mie scattering model as handled in (6). Meanwhile, the correlation coefficient of the fitting at every sampling point was also given.

Then, the simulation results of dust concentration distribution were validated by our field measurement result as

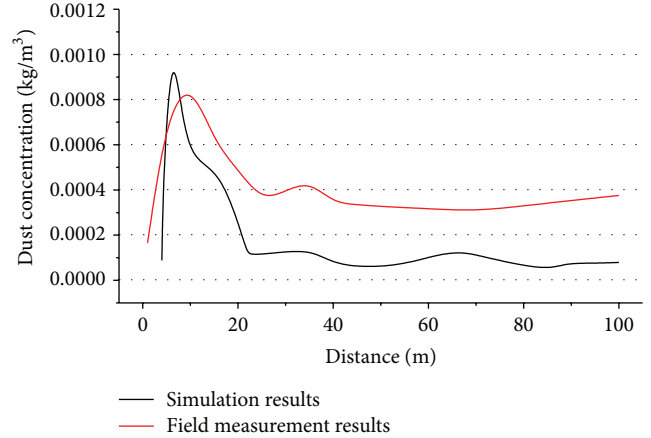


FIGURE 1: Validation of CFD simulation results by field measurement.

described above. Adopt the dust concentration distribution at 1.5 m height along the working face to analyze the difference, as presented in Figure 1.

Figure 1 presents that both the simulation results and field measurement results are firstly increased sharply with the increase of distance and then drop dramatically until 25 m; eventually, the dust concentration gradually keeps stable. This illustrates that the CFD simulation results and field measurement results agree well to a certain extent. However, the peak point of simulation result and field measurement result are a bit deviating, and an obvious difference on dust concentration can be observed when the dust concentration keeps stable especially when the distance comes to 25 m. This is mainly due to the fact that (a) the parameters in CFD simulation are controllable and constant, while, during field measurement, the wind speed may vary a little considering the working condition of fan and the dust release intensity may change a bit with the advance of coal cutting. The uncontrollable factor in field measurement is one of the reasons for such difference. (b) The CFD method just considers the main force between airflow and particles including drag force, gravity, Saffman lift force, thermophoresis force, and brown force. But the interaction of airflow and particles, the rebound of dust particles on ground and wall, the influence of water on dust particles sedimentation (the humidity is quite high in underground coalmine), and the influence of dust particles on airflow are hard to consider but important. The combined effect of these factors results in the difference of dust concentration when distance comes to 25 m. As a whole, the CFD simulation gives an acceptable result especially when considering that it is hard and costly to conduct field measurement under different working conditions (different wind speed, dust release intensity, direction ventilation, etc.).

Apart from the calculation above, the distribution of coal particles under different intensities of dust release (0.002, 0.005, and 0.01 kg/s), different positions of coal cutting (coal cutting machine 5, 30, and 60 m from intake), different wettings of coal seams (original coal seam and coal seam of water injection), different wind speeds (1, 2.5, and 4 m/s), and different directions of ventilation (positive and negative

TABLE 1: Distribution of the coal particle concentration and diameter.

Distance/m	Dust concentration/(kg/m <sup>3</sup> )	Diameter distribution by Rosin-Rammler $W(D) = 100 \exp(-\beta * D^n)$		
		$\beta$	$n$	$R^2$
4.0	8.83E - 05	0.0125	1.0103	0.9718
4.4	5.31E - 04	0.0261	0.8960	0.9733
6.2	1.04E - 03	0.0294	0.8173	0.9744
8.0	7.68E - 04	0.0101	1.0873	0.9871
10.2	5.24E - 04	0.0201	0.9932	0.9905
16.4	4.92E - 04	0.0230	0.9565	0.9876
21.8	1.35E - 04	0.0198	1.0012	0.9877
22.2	1.10E - 04	0.0156	1.1846	0.9838
27.6	1.21E - 04	0.0146	1.4109	0.9753
35.8	1.37E - 04	0.0185	1.2583	0.9764
40.6	5.96E - 05	0.0322	1.0115	0.9730
53.2	5.83E - 05	0.0217	1.1752	0.9878
62.0	1.17E - 04	0.0246	1.1307	0.9865
67.6	1.26E - 04	0.0480	0.9245	0.9490
71.6	1.03E - 04	0.0506	0.9608	0.9509
84.8	4.22E - 05	0.0434	1.0070	0.9632
88.6	7.58E - 05	0.0212	1.4730	0.9781
94.6	7.56E - 05	0.0259	1.3287	0.9794
100.0	7.95E - 05	0.0095	1.6982	0.9865

ventilation) were also simulated; the calculation results of dust distribution were further used in the simulation of transmission properties under different influencing factors in Section 4.

### 3. Complex Refractive and Transmission Properties of Coal Dust

*3.1. Scattering and Optical Constants of Coal Dust Particles.* The dispersion and distribution of coal dust particles in the fully mechanized working face of a coal mine can be obtained according to the simulation of the air-dust coupled flow mathematical model. Based on the simulation results of the coal dust distribution, a Mie scattering model was adopted to obtain the spectral radiation characteristics at wavelength  $\lambda$  of coal dust particles [29]:

$$Q_e(m, \chi) = \frac{C_e}{G} = \frac{2}{\chi^2} \sum_{n=1}^{\infty} (2n+1) \operatorname{Re}(a_n + b_n)$$

$$= \frac{4}{\chi^2} \operatorname{Re}\{S_0\} \quad (2)$$

$$Q_s(m, \chi) = \frac{C_s}{G} = \frac{2}{\chi^2} \sum_{n=1}^{\infty} (2n+1) [ |a_n|^2 + |b_n|^2 ],$$

where  $m$  is the optical constant of particle  $m = n - ik$ ,  $n$  and  $k$  are the refractive index (single refractive index) and absorption index, respectively,  $\chi$  is the size parameter  $\chi = \pi D/\lambda$ ,  $G$  is the geometric projection area of the spherical

TABLE 2: Industrial and elemental analysis of coal particles.

Industrial analysis (%)					Elemental analysis (%)				
M	A	V	Fc	C	H	O	N	S	Others
2.67	24.96	29.63	42.74	58.53	3.60	9.09	0.84	0.31	27.63

particle  $G = \pi D^2/4$  ( $\mu\text{m}^2$ ),  $\operatorname{Re}$  is the real component of complex number,  $a_n$  and  $b_n$  are the Mie scattering coefficients, and  $S_0$  is the prior amplitude functions.

The scattering calculation of coal dust requires both the spatial distribution and the optical constants of coal particles. Thus, the coal dust particles were sampled from the fully mechanized working face of Huangbaici coal mine which is located in Wuda coalfield, northwest China. Then, the industrial and elemental analysis and FT-IR experiment were conducted on the coal particles sampled in underground coal mine to obtain the chemical composition and spectral transmittance of coal dust, as shown in Table 2 and Figure 2. The experimental method and equipment of the industrial analysis and FT-IR test for rock dust have been given in our previous study [30].

Thus, the coal dust particles in the fully mechanized working face can be determined to be bituminous coal particles according to the degree of coal metamorphism based on the industrial and elemental analysis of the coal sample.

In order to conduct FT-IR test, the sampled coal dust particles were firstly pulverized to less than 200 mesh ( $74 \mu\text{m}$ ) and dried at  $105^\circ\text{C}$  for 4 h according to the requirement of

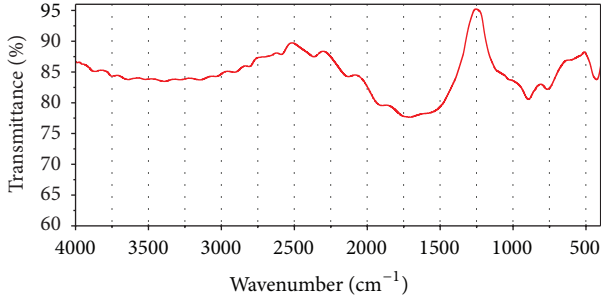


FIGURE 2: Spectral transmittance of coal dust from FT-IR test.

FT-IR test. Then, coal dust particles were suspended and pressed in a KBr matrix with the thickness of 1 mm and the proportion of 1:100 under the pressure of 10 t/cm<sup>2</sup> for 3 min. The well prepared KBr matrix was subsequently measured on its spectral transmittance within the spectral region 400–4000 cm<sup>-1</sup>, as shown in Figure 2. The FT-IR equipment used in this test is Bruker Vertex 80v which is manufactured in Germany. The main performance indexes of Bruker Vertex 80v are as follows: spectral range, 8000–350 cm<sup>-1</sup>; spectral resolution, 0.06 cm<sup>-1</sup>; sensitivity, under the condition of full spectrum of linear accuracy better than 0.7%, peak-peak noise value < 8.6 × 10<sup>-6</sup> Abs, signal-to-noise ratio better than 55000:1 (peak to peak); linearity, 0.07%; interferometer, high precision dynamic calibration Mayer interferometer.

Based on the spectral transmittance of coal dust particles, combined with the properties of KBr matrix preparation, Kramers-Kronig (K-K) relation was adopted to retrieve the optical constant of rock index [31, 32]. Through the simulation, the optical constant of bituminous coal dust was obtained as shown in Figure 3.

**3.2. Transmitting Behavior of Coal Dust.** The particle swarms of coal dust in any location along the fully mechanized working faces are composed of a series of different scale particles. The optical radiation parameters of a nonuniform particle swarm can be given by the following formula:

$$\beta = \int_0^{\infty} C_e(D) N(D) dD \quad (3)$$

$$\sigma_s = \int_0^{\infty} C_s(D) N(D) dD \quad (4)$$

$$\omega = \frac{\sigma_s}{\beta}, \quad (5)$$

where  $D$  is the diameter of particle,  $\mu\text{m}$ ;  $C_e(D)$  and  $C_s(D)$  are the attenuation and scattering cross section of a particle with a diameter of  $D$ ;  $N(D)$  is the particle number density distribution, in  $\text{m}^{-3} \cdot \mu\text{m}^{-1}$ ; and  $\omega$  is the scattering albedo:

$$N(D) = -\frac{dW(D)}{dD} \cdot \frac{\rho_a}{\rho_b (4/3) \pi D^3}, \quad (6)$$

where  $\rho_a$  and  $\rho_b$  are the quantity concentration of the total dust and actual density of coal, respectively. Because of

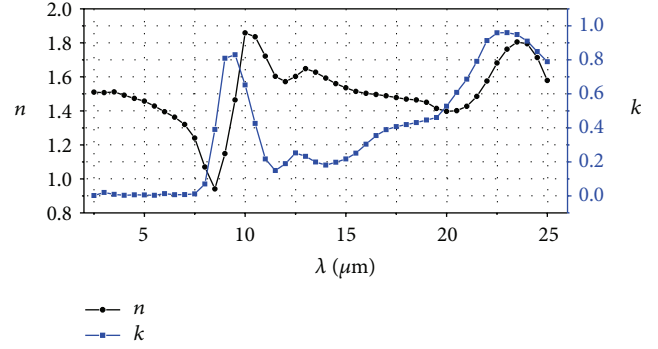


FIGURE 3: The optical constant of coal particles.

the common industrial analysis of coal dust, nonuniform particles are generally divided into several size ranges for statistics. Then, discrete integration was employed to approximate the Rosin-Rammler function in this paper, and the middle diameters of each particle group were selected as equivalent diameters for calculation to approximate the above equations.

Based on the optical scattering and extinction properties of coal dust obtained from Mie scattering calculation, aimed at the transmission characteristics and aerosol optical depth (AOD) of dust particles, the numerical method of radiative transfer was applied [33–38]. Here, considering a gray medium condition, the one-dimensional radiative transfer equation (RTE) at the wavelength  $\lambda$  on the direction  $\theta$  can be written as follows:

$$\begin{aligned} \cos \theta \frac{dI(\tau)}{d\tau} &= (1 - \omega) I_b(\tau) - I(\tau) \\ &+ \frac{\omega}{2} \int_0^{\pi} I(\tau, \theta_i) \Phi(\theta, \theta_i) \sin \theta_i d\theta_i, \end{aligned} \quad (7)$$

where  $\tau$  is the spectral optical thickness;  $I$  is the intensity of the radiation, in  $\text{W}/(\text{m}^2 \cdot \text{sr})$ ; and  $I_b$  is the radiation intensity of blackbody. Considering isotropic scattering ( $\Phi \equiv 1$ ), the two-flux method was applied to calculate and analyze the spectral radiation intensity and spectral transmission characteristics of the dust particle system in a one-dimensional direction [39]. Assume the radiation intensity in positive and negative directions to be a constant value and assume it has nothing to do with the angle. Thus,

$$\begin{aligned} \frac{1}{2} \frac{dI^+}{d\tau} &= (1 - \omega) I_b - I^+ + \frac{\omega}{2} (I^- + I^+) \\ -\frac{1}{2} \frac{dI^-}{d\tau} &= (1 - \omega) I_b - I^- + \frac{\omega}{2} (I^- + I^+). \end{aligned} \quad (8)$$

The corresponding boundary conditions are  $I^+ = 0$  for  $\tau = 0$  and  $I^- = 0$  for  $\tau = \tau_L$ ;  $I^-$  and  $I^+$  are the radiation intensities in positive and negative direction, respectively, in  $\text{W}/(\text{m}^2 \cdot \text{sr})$ . Then, the average apparent transmittance of coal dust at the wavelength  $\lambda$  can be given as

$$\gamma = \frac{2\pi I^+}{E_b}, \quad (9)$$

where  $E_b$  is the radiation of blackbody.

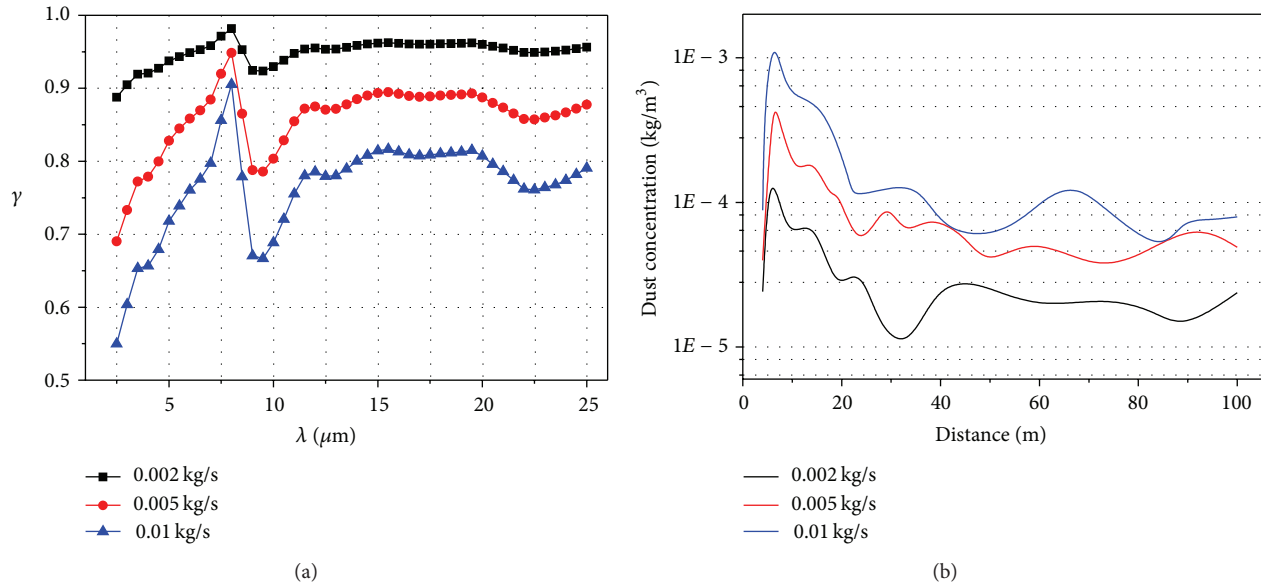


FIGURE 4: Influence of the dust release intensity on (a) spectral transmittance and (b) dust concentration.

#### 4. Results of Dust Optical Characteristics under Different Operating Conditions

The distribution of coal particles in a fully mechanized working face is mainly affected by the dust source and airflow field. Aimed at different influencing factors of the dust source (intensity of dust release, position of coal cutting, and the wetting of the coal seam) and airflow field (wind speed and direction of ventilation), combined with the optical constant of coal dust in Figure 2, the transmission characteristics and AOD of the coal particles were simulated and analyzed by solving Mie scattering model and heat flux method. The optical constant of coal dust obtained and the radiative transfer equation solved are all at the ambient temperature (300 K) of underground coal mine.

**4.1. Influence of the Intensity of Dust Release.** The intensity of coal dust release is closely linked to the cutting speed, cutting depth, and lead angle of the coal cutting machine, which further affects the distribution of the coal particles in fully mechanized working face. Based on the CFD simulation results of dust distribution under different dust release intensities (0.002, 0.005, and 0.01 kg/s) in combination with the heat flux method, the transmission characteristics of coal particles were calculated and analyzed.

As can be seen from Figure 4(a), the transmittance of coal dust increases sharply with the increasing wavelength, reaching a maximum at 8  $\mu\text{m}$  and then decreasing rapidly, reaching a minimum at 9.5  $\mu\text{m}$ . Eventually, the transmittance rises gently and remains stable when the wavelength is 12  $\mu\text{m}$ . The transmittance is obviously decreased with increasing dust release intensity; the degree of decrease is relatively much smaller for 8  $\mu\text{m}$ . This is because the concentration of coal dust is greatly increased with increasing dust release intensities, as seen from Figure 4(b), resulting in the weakened

transmission characteristics of coal particles in Figure 4(a). The spectral transmittance is the strongest for 8  $\mu\text{m}$ , which weakens the influence of dust concentration, thus causing the degree of transmittance decrease that is relatively much smaller for 8  $\mu\text{m}$ .

**4.2. Effect of the Position of Coal Cutting.** With advances in coal mining activities in a fully mechanized working face, a coal cutting machine would move from one side of the coal seam to another side. Coal particles generated during the process of coal cutting mainly disperse in the downward airflow of the coal cutting machine; the atmosphere in the upward airflow of the coal cutting machine is mainly fresh air with few contaminants (the dust concentration was set to be  $1 \times 10^{-5} \text{ kg}/\text{m}^3$  according to Wang and Ren [1]). Thus, three positions of coal cutting (coal cutting machine is 5, 30, and 60 m from the intake of the working face) were adopted in this section to simulate the transmission characteristics of the coal particles. The transmittance of coal dust under the position of coal cutting that is 30 m from the intake is divided by that of 5 m and 60 m to obtain the dimensionless ratio ( $\gamma_{5\text{m}}/\gamma_{30\text{m}}$  and  $\gamma_{60\text{m}}/\gamma_{30\text{m}}$ ) for further analysis, as shown in Figure 5.

Figure 5(a) shows that the dimensionless ratio  $\gamma_{5\text{m}}/\gamma_{30\text{m}}$  is less than 1, while the ratio  $\gamma_{60\text{m}}/\gamma_{30\text{m}}$  is greater than 1 under the waveband of 2.5 to 25  $\mu\text{m}$ , which indicates that the transmittance characteristics are increased with the advance of coal mining activity. This is because, with the advance of coal mining activity, the coal cutting machine gradually moves from the intake to the outtake of the working face; the downwind region is heavily polluted by coal dust and is gradually diminished but the upwind region, which is relatively fresher, is enlarged, causing the decrease of coal dust pollution as a whole in a fully mechanized working face.

An obvious trend that approximates a constant value of 1 is observed at the waveband from 7 to 9  $\mu\text{m}$  for  $\gamma_{5\text{m}}/\gamma_{30\text{m}}$

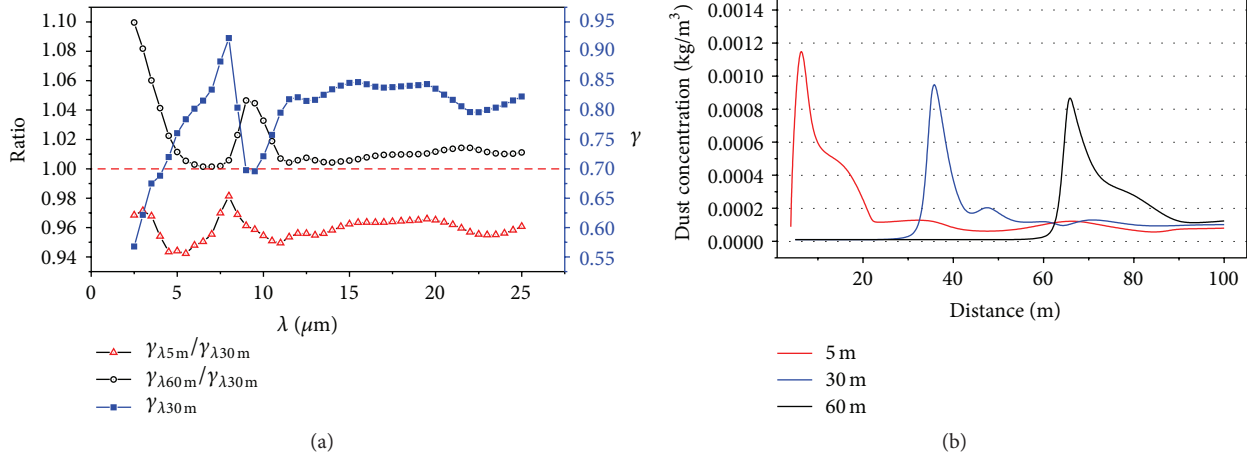


FIGURE 5: Effect of the position of coal cutting on (a) spectral transmittance and (b) dust concentration.

and from 6 to 8  $\mu\text{m}$  for  $\gamma_{60\text{m}}/\gamma_{30\text{m}}$ , indicating that variations of transmittance with different coal cutting positions are weakened. This is because the spectral transmittance of coal dust is the strongest at the wavelength of approximately 8  $\mu\text{m}$ ; the influence of dust distribution on transmission characteristics is obviously reduced at 8  $\mu\text{m}$  compared to other wavebands.

**4.3. Impact of Wind Speed and the Wetting of the Coal Seam on AOD.** The ventilation system of a coal mine mainly aims to provide fresh air for the underground workers by carrying contaminants (e.g., methane, carbon monoxide, and dust) away from the coal mine. Coal particles spread outwards in a fully mechanized working face, mainly relying on the effect of airflow. Meanwhile, wetting technology has been widely used in most coal mines by water injection before the extraction of the coal seam. Relevant studies have shown that the distributions of coal particles' concentration and diameter are directly affected by wind speed and the use of water injection technologies, further affecting the transmission characteristics of coal particles. The speed of airflow in a fully mechanized working face is confined within 0.25 to 4 m/s according to the safety regulations in coal mines in China. Thus, with the original coal seam under different wind speeds (1, 2.5, and 4 m/s) and the wetting coal seam under wind speed of 2.5 m/s, the AOD of coal particles was simulated and analyzed, as shown in Figure 6.

Figure 6 indicates that the AOD of coal dust is obviously decreased with the increasing wind speed in a fully mechanized working face. This is because airflow is the main cause for the outward spread of coal particles; the settlement of coal particles under different wind speeds varies greatly when there is an optimal speed for dust settlement. Before the optimal speed, coal particles are more prone to settle with increasing wind speed. All of the wind speeds (1, 2.5, and 4 m/s) that were set up in our study are under the optimal speed presented in Figure 7(a), causing a decreased distribution of coal dust as well as a decreased AOD of coal particles.

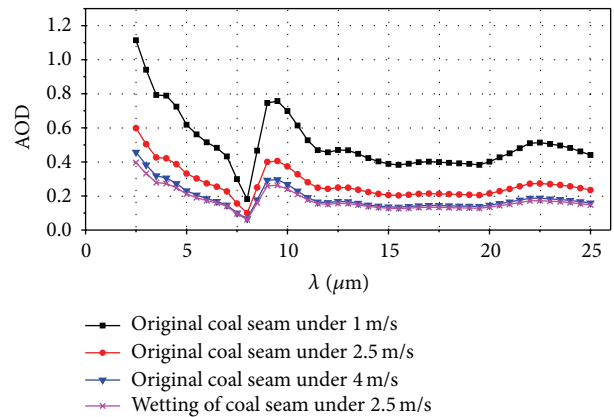


FIGURE 6: Spectral AOD of coal dust under different wind speeds and wettings of the coal seam.

The AOD of coal particles is obviously decreased by adopting the water injection technology of the coal seam. The moisture of the coal seam can be increased with the use of water injection technology, which is against the generation of coal particles during the process of coal cutting. Small particles can form larger particles under the effect of increased moisture causing much easier settlement. Thus, the concentration of coal particles in Figure 7(b) is decreased with the use of water injection technology, resulting in the decreased AOD of coal particles in the fully mechanized working face.

**4.4. Effect of the Direction of Ventilation on AOD.** The ventilation in the fully mechanized working face can be divided into positive ventilation and negative ventilation considering the direction of coal cutting and airflow. The coal cutting and airflow have the same direction for positive ventilation and the opposite direction for negative ventilation. Based on the CFD simulation results under positive and negative ventilation, the AOD of coal particles in the fully mechanized

TABLE 3: Spectral AOD versus direction of ventilation.

$\lambda/\mu\text{m}$	AOD	AOD	$\lambda/\mu\text{m}$	AOD	AOD	$\lambda/\mu\text{m}$	AOD	AOD
	Positive direction	Negative direction		Positive direction	Negative direction		Positive direction	Negative direction
3	0.52062	0.60375	11	0.28086	0.31968	19	0.20359	0.23151
4	0.43089	0.49614	12	0.23811	0.27075	20	0.21137	0.2406
5	0.33751	0.38509	13	0.24519	0.2788	21	0.23871	0.27215
6	0.27493	0.31253	14	0.21768	0.2472	22	0.27067	0.30879
7	0.21937	0.24891	15	0.2002	0.22729	23	0.26736	0.30463
8	0.09544	0.10727	16	0.20257	0.23017	24	0.25376	0.28889
9	0.40835	0.47070	17	0.21023	0.23911	25	0.23153	0.26354
10	0.37973	0.43616	18	0.20673	0.23511			

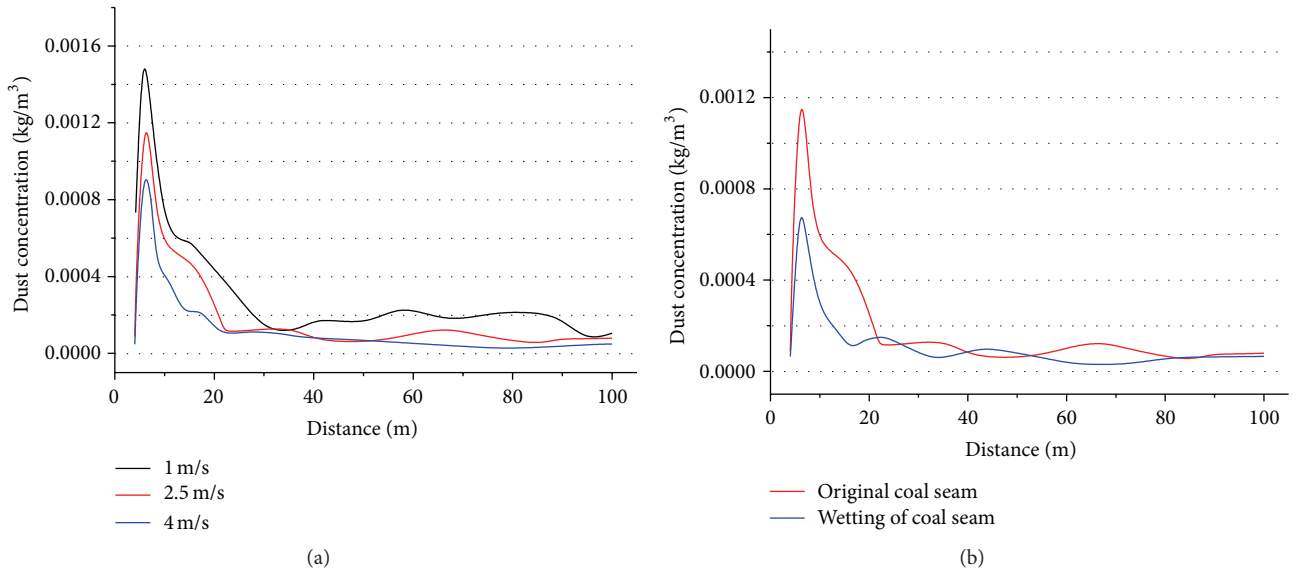


FIGURE 7: Dust concentration under different (a) wind speeds and (b) wettings of the coal seam.

working face was simulated and analyzed, as presented in Table 3.

Table 3 shows that the AOD of coal particles under positive and negative directions has a similar variation law versus wavelength. However, the AOD under positive ventilation is slightly weaker than that under negative ventilation. This is because the turbulence effect of airflow would be slightly enhanced under negative ventilation as a whole, which is against the settlement of coal dust; the average concentration of coal dust is  $1.90E - 4 \text{ kg/m}^3$  for negative ventilation and is  $1.307E - 4 \text{ kg/m}^3$  for positive ventilation, as seen from Figure 8.

## 5. Waveband Selection and Field Application

As can be concluded from the simulation and analysis above, the transmission properties of coal dust in fully mechanized working face vary obviously under different working conditions and influencing factors which reflect the variation of the dust concentration and dust diameter distribution in essence. An anomalous point of transmittance around  $8 \mu\text{m}$  was observed in Section 4 which varies minimally under

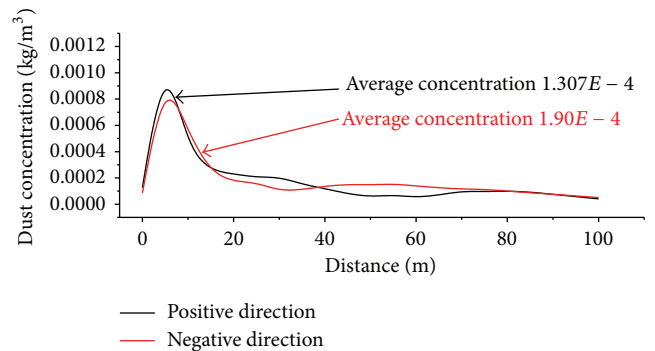


FIGURE 8: Dust concentrations under different directions of ventilation.

different influencing factors. Aiming at the evaluation of dust concentration level in the whole working face, the influencing effect of dust diameter on the transmittance signal should be determined first.

*5.1. Influence of Dust Diameter on Transmittance.* To study the influence of diameter, a formula,  $\gamma_{\text{ratio-s}} = (\gamma_m - \gamma_s)/\gamma_m$ ,

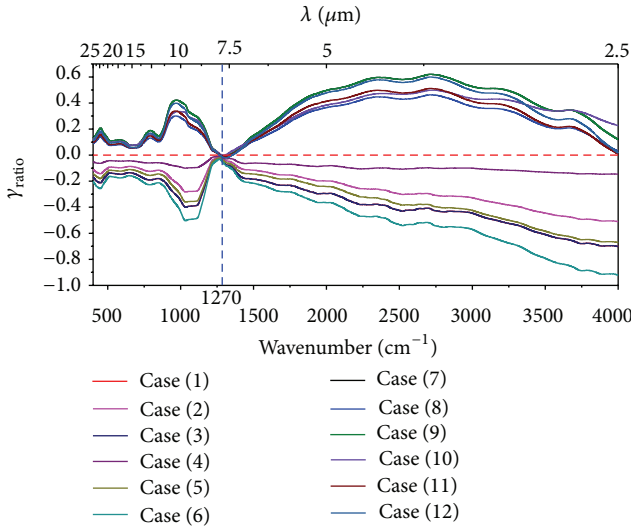


FIGURE 9: Influence of diameter on transmittance under different cases (uniform dust diameter, dust release intensity, position of coal cutting, wind speed, whether there is wetting of coal seam or not, and direction of ventilation): (1)  $5 \mu\text{m}$ ,  $0.005 \text{ kg/s}$ ,  $5 \text{ m}$ ,  $2.5 \text{ m/s}$ , no, positive; (2)  $5 \mu\text{m}$ ,  $0.005 \text{ kg/s}$ ,  $5 \text{ m}$ ,  $4 \text{ m/s}$ , no, positive; (3)  $5 \mu\text{m}$ ,  $0.01 \text{ kg/s}$ ,  $5 \text{ m}$ ,  $2.5 \text{ m/s}$ , no, positive; (4)  $5 \mu\text{m}$ ,  $0.005 \text{ kg/s}$ ,  $5 \text{ m}$ ,  $2.5 \text{ m/s}$ , yes, positive; (5)  $5 \mu\text{m}$ ,  $0.005 \text{ kg/s}$ ,  $30 \text{ m}$ ,  $2.5 \text{ m/s}$ , no, positive; (6)  $5 \mu\text{m}$ ,  $0.005 \text{ kg/s}$ ,  $5 \text{ m}$ ,  $2.5 \text{ m/s}$ , no, negative; (7)  $50 \mu\text{m}$ ,  $0.005 \text{ kg/s}$ ,  $5 \text{ m}$ ,  $2.5 \text{ m/s}$ , no, positive; (8)  $50 \mu\text{m}$ ,  $0.005 \text{ kg/s}$ ,  $5 \text{ m}$ ,  $4 \text{ m/s}$ , no, positive; (9)  $50 \mu\text{m}$ ,  $0.01 \text{ kg/s}$ ,  $5 \text{ m}$ ,  $2.5 \text{ m/s}$ , no, positive; (10)  $50 \mu\text{m}$ ,  $0.005 \text{ kg/s}$ ,  $5 \text{ m}$ ,  $2.5 \text{ m/s}$ , yes, positive; (11)  $50 \mu\text{m}$ ,  $0.005 \text{ kg/s}$ ,  $30 \text{ m}$ ,  $2.5 \text{ m/s}$ , no, positive; (12)  $50 \mu\text{m}$ ,  $0.005 \text{ kg/s}$ ,  $5 \text{ m}$ ,  $2.5 \text{ m/s}$ , no, negative.

was put forward, where  $\gamma_{\text{ratio-s}}$  represents the influence of the transmittance of coal dust with uniform diameter ( $\gamma_s$ ) on that of a mixture of dust ( $\gamma_m$ ),  $\gamma_m$  is the transmittance of mixture dust, and  $\gamma_s$  is the transmittance of coal dust with uniform diameter ( $5 \mu\text{m}$  (representing small particle) and  $50 \mu\text{m}$  (representing large particle)) based on the same concentration of the CFD simulation. The influence of dust diameter on transmittance under different working conditions and influencing factors was calculated and summarized, as shown in Figure 9.

Figure 9 indicates that the spectral variations of  $\gamma_{\text{ratio-s}}$  under different intensities of dust release and wind speed are similar, except for the difference in concrete magnitude.  $\gamma_{\text{ratio-}5 \mu\text{m}}$  under different intensities of dust release and wind speed are all positive, while  $\gamma_{\text{ratio-}50 \mu\text{m}}$  are all negative, which indicates that the transmittance of coal dust is obviously enhanced with increasing diameter under the same distribution of dust concentration. With the decrease of the dust release intensity and the increase of wind speed, the spectral variations of  $\gamma_{\text{ratio-s}}$  gradually become relatively stable.

The spectral variations of  $\gamma_{\text{ratio-s}}$  fluctuate greatly under wavebands of  $400\text{--}4000 \text{ cm}^{-1}$  ( $25\text{--}2.5 \mu\text{m}$ ) among which an anomalous waveband around  $1270 \text{ cm}^{-1}$  whose absolute value reaches the minimum point of zero (all within 0.05) can be obviously observed. Such waveband indicates that the

transmittance of coal dust is almost not sensitive to the variation of dust diameter under around  $1270 \text{ cm}^{-1}$ ; considering the variation of transmittance under different influencing factors listed in Section 4 under around  $1270 \text{ cm}^{-1}$ , it can be deduced that the transmittance is the only function of dust concentration under the permissible error for engineering application.

5.2. Correlation of Dust Concentration and Infrared Transmittance. According to the above discussions, the optical channel of  $1260\text{--}1280 \text{ cm}^{-1}$  ( $7.937\text{--}7.813 \mu\text{m}$ ) is selected in this case study to evaluate the dust concentration level in fully mechanized working face; for that, the transmission signal is almost only sensitive to the variation of dust concentration. By adopting the equivalent transmittance within the optical channel of  $1260\text{--}1280 \text{ cm}^{-1}$  ( $7.937\text{--}7.813 \mu\text{m}$ ) and equivalent dust concentration of the whole working face, the variation law of dust concentration and the optical transmittance in whole working face was further calculated and analyzed. Here, considering the irrelevance between the transmittance within  $1260\text{--}1280 \text{ cm}^{-1}$  and particle size as demonstrated in Figure 9, a mean diameter  $20 \mu\text{m}$  representing the nonuniform particles was adopted in the Mie calculations according to the analysis in Section 2.2. The equivalent transmittance within  $1260\text{--}1280 \text{ cm}^{-1}$  ( $7.937\text{--}7.813 \mu\text{m}$ ) can be calculated by

$$\bar{\gamma} = \frac{\int_{\lambda_1}^{\lambda_2} \gamma E_b d\lambda}{\int_{\lambda_1}^{\lambda_2} E_b d\lambda}. \quad (10)$$

The dust concentration can be obtained by the one-to-one relationship between dust concentration and optical transmittance presented in Figure 10(a) if the optical transmittance was determined. Meanwhile, considering dust suppression method and equipment, there is a maximum limit of dust concentration in the working face. Thus, only some points marked in Figure 10(a) are valid which can be used for the evaluation of dust concentration in underground working face. The invalid points exceed the dust concentration level in working face which is useless and meaningless in this study. Further analysis on the valid data was conducted by fitting the curve to obtain the corresponding function, as shown in Figure 10(b).

For the engineering application, the function and control variables should not be too complex; meanwhile, the function must agree well with the curve and points. Thus, a polynomial with two polynomial orders was used to fit the curve and points in Figure 10(b). The fitting results agree well with the original points whose correlation coefficient reaches 0.99995 and the residual sum of squares is  $1.04373E - 4$ . Thus, an effective fitting function was put forward and given as follows:

$$C = 2.06214 * \bar{\gamma}^2 - 6.44759 * \bar{\gamma} + 4.39114. \quad (11)$$

5.3. Field Application in Huangbaici Coal Mine. Simulation study gives the function of dust concentration and optical transmittance under the optical channel of  $1260\text{--}1280 \text{ cm}^{-1}$  ( $7.937\text{--}7.813 \mu\text{m}$ ) for its dullness of dust diameter variation.

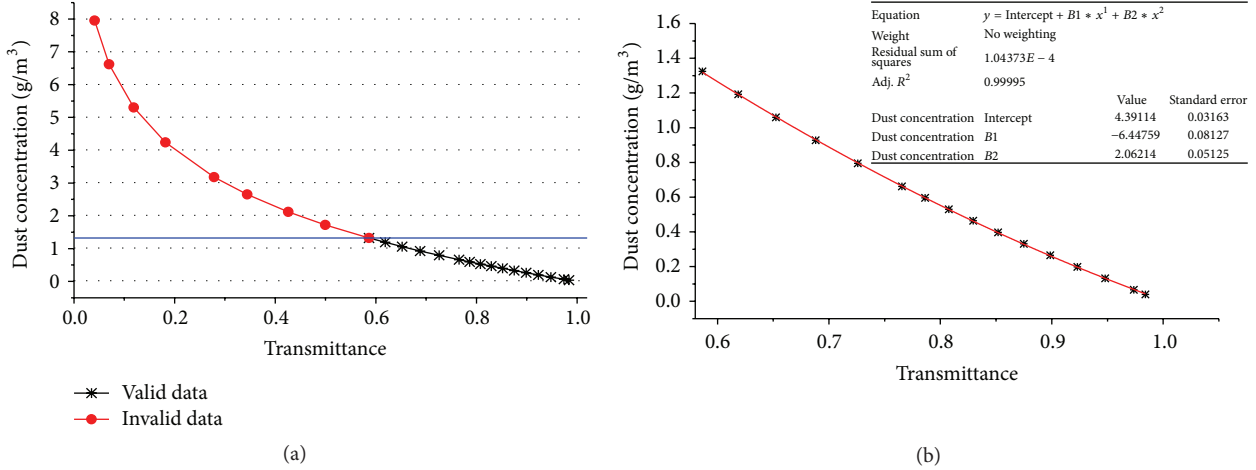


FIGURE 10: The correlation between dust concentration and transmittance.

TABLE 4: Dust concentration distribution along the working face.

Distance/m	Dust concentration/(g/m <sup>3</sup> )		
	0.5 m	1.5 m	2.5 m
1	0.24021	0.16605	0.06150
5	0.74450	0.72991	0.12454
10	0.93809	0.88750	0.19890
15	0.51265	0.61281	0.24133
20	0.41177	0.48878	0.29447
25	0.32211	0.35261	0.32579
30	0.33073	0.39576	0.33696
35	0.33935	0.43890	0.34812
40	0.32293	0.34323	0.28529
45	0.31482	0.33517	0.28121
50	0.30671	0.32711	0.27713
60	0.29748	0.31686	0.27264
70	0.28825	0.30661	0.26816
80	0.30564	0.32971	0.26749
90	0.32303	0.35282	0.26683
100	0.34042	0.37592	0.26617

Then, the fitting function obtained was used in field underground working face of Huangbaici coal mine to evaluate the dust concentration level.

The field measurement experiments on coal dust distribution have been carried out and described in Section 2.2. Then, the coal dust distribution measured samples at three heights above the ground (0.5 m, 1.5 m, and 2.5 m) were shown in Table 4.

Based on the field data of dust distribution in three sampling lines (0.5 m, 1.5 m, and 2.5 m high along the working face), the optical transmittance of the three lines was calculated. The transmittance within the optical channel of 1260–1280 cm<sup>-1</sup> (7.937–7.813 μm) was listed in Table 5.

Then, the equivalent transmittance of three lines was loaded into (11) to retrieve the equivalent dust concentration in the fully mechanized working face. Meanwhile, the

equivalent dust concentration was also directly calculated from the field data. The directly calculated dust concentration and retrieved dust concentration were compared to get the relative error, as listed in Table 6.

The retrieved data is a little greater than field data but all within the relative error of 0.1. The error is mainly due to the fact that the transmittance within optical channel of 1260–1280 cm<sup>-1</sup> (7.937–7.813 μm) is still slightly influenced by the diameter distribution which cannot be totally removed. Meanwhile, small error still exists in the fitting function which is hard to eliminate especially for engineering application. However, such results with all the relative errors within 0.1 can also be accepted for engineering application which can be used for dust concentration evaluation in the fully mechanized working face of Huangbaici coal mine.

#### 5.4. Limitation of the Methodology for Retrieving Dust Concentration.

The coal dust concentration in underground working face can be retrieved by the methodology presented in this paper. Meanwhile, obvious shortcomings and limitations still exist concerning this method mainly including the following: (a) the optical channel of 1260–1280 cm<sup>-1</sup> (7.937–7.813 μm) was adopted in this study to correlate dust concentration and transmittance, when dust concentration is high to a certain extent which may cause the optical signal to be invalid. Such occasion does not exist because there is a maximum limit of dust concentration under normal mining conditions that cannot lead the optical signal to be invalid which have been discussed in Section 5.2. Meanwhile, when the dust concentration is low to a certain extent which leads to quite high transmittance, in this occasion, the transmittance is not sensitive to the variation of dust concentration. Take transmittance 0.995 as an example; according to our correlation, the equivalent dust concentration was obtained as low as 0.01735 g/m<sup>3</sup> (17.35 mg/m<sup>3</sup>). When dust concentration is lower than 0.01735 g/m<sup>3</sup> which may be caused by lower dust release intensity, larger wind speed, or farther distance of coal cutting from the intake, it is hard to detect the variation of dust concentration from transmittance. (b) The

TABLE 5: The transmittance of coal dust under the optical channel of 1260–1280  $\text{cm}^{-1}$ .

Height/m	Transmittance			
	1260 $\text{cm}^{-1}$	1270 $\text{cm}^{-1}$	1280 $\text{cm}^{-1}$	Equivalent
0.5	0.79357634	0.78322529	0.76093461	0.779245413
1.5	0.77153042	0.76953047	0.74345684	0.761505907
2.5	0.83354416	0.84187375	0.83086851	0.835428809

TABLE 6: The comparison of field data and retrieved data.

Height/m	Equivalent dust concentration/( $\text{g}/\text{m}^3$ )		
	Field data	Retrieved data	Relative error
0.5	0.583638	0.619065	0.060700756
1.5	0.626850	0.677079	0.080129348
2.5	0.410757	0.443890	0.080663723

transmittance under 1260–1280  $\text{cm}^{-1}$  (7.937–7.813  $\mu\text{m}$ ) was considered as the only function of dust concentration and almost not influenced by dust diameter distribution. Actually, small impact of dust diameter variation on transmittance still exists which is one of the main reasons for the relative error in Table 6. Thus, if there exists any, more appropriate optical detection channel should be searched in other bands, like terahertz wave and millimeter wave. (c) The mean diameter of nonuniform particles was set to be 20  $\mu\text{m}$  for the correlation of dust concentration and transmittance. When the diameters of all the particles are greater than the mean diameter (20  $\mu\text{m}$ ) by an order of magnitude or more, the transmittance under 1260–1280  $\text{cm}^{-1}$  (7.937–7.813  $\mu\text{m}$ ) may be changed to be sensitive to the variation of dust diameter which may result in the failure of (11). Such occasion does not exist in underground coal mine for there is a limited range of dust diameter. Special attention should be paid in extreme cases.

## 6. Conclusions

Aiming at the respirable coal dust pollution in the fully mechanized working face of Huangbaici coal mine, the coal particles were sampled to conduct the industrial analysis and FT-IR test in order to obtain the chemical composition and optical constants of coal particles. The spatial distribution of coal dust in working face was also measured by field measurement method. The variation of dust spatial distribution under different influencing factors of dust sources (intensity of dust release, position of coal cutting, and the wetting of the coal seam) and airflow fields (wind speed and direction of ventilation) was simulated. Based on the optical constants of coal dust obtained from FT-IR experiment, combined with the Mie scattering and heat flux method, the transmission characteristics and AOD of coal dust were analyzed and summarized. Simulation results show that (a) the transmission characteristics of coal dust are greatly decreased with the increasing dust release intensity but are slightly enhanced with the advance of the coal mining activity. The AOD of coal dust is obviously decreased with the wetting of the

coal seam. (b) The spectral AODs of coal dust are obviously decreased with increasing wind speeds under the threshold of the optimal wind speed. The AOD of coal dust under negative ventilation is slightly greater than that under positive ventilation.

Furthermore, an optical channel of 1260–1280  $\text{cm}^{-1}$  (7.937–7.813  $\mu\text{m}$ ) was observed in the transmittance under different influencing factors and further analyzed on its sensitivity of dust diameter variation. The analysis proved that the transmittance of coal dust under the optical channel of 1260–1280  $\text{cm}^{-1}$  (7.937–7.813  $\mu\text{m}$ ) is almost not influenced by the variation of dust diameter and can be considered as the only function of dust concentration. Then, a fitting function was given based on the correlation of dust concentration and optical transmittance considering the dust pollution level in underground working face. Based on the field measurement data on the dust pollution in this working face, the optical transmittance was calculated and then loaded into the corresponding fitting function in our study to get the retrieved equivalent dust concentration. The field dust concentration and retrieved dust concentration agree well considering the engineering application and all the relative errors are within 0.1. Such method including the optical channel and fitting function can be used for the monitoring of the equivalent dust concentration in the fully mechanized working face of Huangbaici coal mine.

## Competing Interests

The authors declare that they have no competing interests.

## Acknowledgments

This research is supported by the Outstanding Youth Science Foundation of NSFC (no. 51522601) and Program for New Century Excellent Talents in University (NCET-13-0173).

## References

- [1] Z. Wang and T. Ren, "Investigation of airflow and respirable dust flow behaviour above an underground bin," *Powder Technology*, vol. 250, pp. 103–114, 2013.
- [2] E. Petavratzi, S. Kingman, and I. Lowndes, "Particulates from mining operations: a review of sources, effects and regulations," *Minerals Engineering*, vol. 18, no. 12, pp. 1183–1199, 2005.
- [3] S. Su, H. Chen, P. Teakle, and S. Xue, "Characteristics of coal mine ventilation air flows," *Journal of Environmental Management*, vol. 86, no. 1, pp. 44–62, 2008.

- [4] R. K. Eckhoff, "Does the dust explosion risk increase when moving from  $\mu\text{m}$ -particle powders to powders of nm-particles?" *Journal of Loss Prevention in the Process Industries*, vol. 25, no. 3, pp. 448–459, 2012.
- [5] Y. Xue, F. Gao, and X. Liu, "Effect of damage evolution of coal on permeability variation and analysis of gas outburst hazard with coal mining," *Natural Hazards*, vol. 79, no. 2, pp. 999–1013, 2015.
- [6] A. M. Donoghue, "Occupational health hazards in mining: an overview," *Occupational Medicine*, vol. 54, no. 5, pp. 283–289, 2004.
- [7] D. E. Gildfind and R. G. Morgan, "A new shock tube configuration for studying dust-lifting during the initiation of a coal dust explosion," *Journal of Loss Prevention in the Process Industries*, vol. 29, no. 1, pp. 198–208, 2014.
- [8] M. Onder and S. Onder, "Evaluation of occupational exposures to respirable dust in underground coal mines," *Industrial Health*, vol. 47, no. 1, pp. 43–49, 2009.
- [9] K. Vizayakumar and P. K. J. Mohapatra, "Environmental impact analysis of a coalfield," *Journal of Environmental Management*, vol. 34, no. 2, pp. 79–103, 1992.
- [10] R. Klemens, P. Kosinski, P. Wolanski et al., "Numerical study of dust lifting in a channel with vertical obstacles," *Journal of Loss Prevention in the Process Industries*, vol. 14, no. 6, pp. 469–473, 2001.
- [11] J. Toraño, S. Torno, M. Menéndez, and M. Gent, "Auxiliary ventilation in mining roadways driven with roadheaders: validated CFD modelling of dust behaviour," *Tunnelling and Underground Space Technology*, vol. 26, no. 1, pp. 201–210, 2011.
- [12] M. Liu, G. Shi, Z. Guo, Y. Wang, and L. Ma, "3-D simulation of gases transport under condition of inert gas injection into goaf," *Heat and Mass Transfer*, 2016.
- [13] T. Ren, Z. Wang, and G. Cooper, "CFD modelling of ventilation and dust flow behaviour above an underground bin and the design of an innovative dust mitigation system," *Tunnelling and Underground Space Technology*, vol. 41, no. 1, pp. 241–254, 2014.
- [14] S. Wang and J. Hao, "Air quality management in China: issues, challenges, and options," *Journal of Environmental Sciences*, vol. 24, no. 1, pp. 2–13, 2012.
- [15] E. Emili, C. Popp, M. Petitta, M. Riffler, S. Wunderle, and M. Zebisch, "PM10 remote sensing from geostationary SEVIRI and polar-orbiting MODIS sensors over the complex terrain of the European Alpine region," *Remote Sensing of Environment*, vol. 114, no. 11, pp. 2485–2499, 2010.
- [16] Z. Ruan, Y. Yuan, X. Zhang, Y. Shuai, and H. Tan, "Determination of optical properties and thickness of optical thin film using stochastic particle swarm optimization," *Solar Energy*, vol. 127, pp. 147–158, 2016.
- [17] Y. Yuan, Y. Shuai, X.-W. Li, B. Liu, and H.-P. Tan, "Using a new aerosol relative optical thickness concept to identify aerosol particle species," *Atmospheric Research*, vol. 150, pp. 1–11, 2014.
- [18] K. Lebecki and M. Małachowski, "Optical method for continuous monitoring of dust deposition in mine's entry," *Archives of Mining Sciences*, vol. 57, no. 3, pp. 517–534, 2012.
- [19] P. Lilienfeld and J. Dulchinos, "Portable instantaneous mass monitor for coal mine dust," *American Industrial Hygiene Association Journal*, vol. 33, no. 3, pp. 136–145, 1972.
- [20] A. H. Lehocky and P. L. Williams, "Comparison of respirable samplers to direct-reading real-time aerosol monitors for measuring coal dust," *American Industrial Hygiene Association Journal*, vol. 57, no. 11, pp. 1013–1018, 1996.
- [21] Y. Liang, H. Liang, and S. Zhu, "Mercury emission from coal seam fire at Wuda, Inner Mongolia, China," *Atmospheric Environment*, vol. 83, pp. 176–184, 2014.
- [22] C. Kuenzer, J. Zhang, Y. Sun, Y. Jia, and S. Dech, "Coal fires revisited: The Wuda coal field in the aftermath of extensive coal fire research and accelerating extinguishing activities," *International Journal of Coal Geology*, vol. 102, pp. 75–86, 2012.
- [23] S. Dai, D. Ren, Y. Tang, L. Shao, and S. Li, "Distribution, isotopic variation and origin of sulfur in coals in the Wuda coalfield, Inner Mongolia, China," *International Journal of Coal Geology*, vol. 51, no. 4, pp. 237–250, 2002.
- [24] W. Z. Wang, Y. M. Wang, and G. Q. Shi, "Forward research on transmission characteristics of near-surface particulate-matter-polluted atmosphere in mining area combined with CFD method," *Optics Express*, vol. 23, no. 15, pp. A1010–A1023, 2015.
- [25] H. Liu, *Coal Mine Safety Regulation, Expert Interpretation*, China University of Mining and Technology Press, Xuzhou, China, 2006 (Chinese).
- [26] J. Yang, X. Wu, J. Gao, and G. Li, "Surface characteristics and wetting mechanism of respirable coal dust," *Mining Science and Technology*, vol. 20, no. 3, pp. 365–371, 2010.
- [27] H. S. G. Tucker, "The particle size of some Witwatersrand mine dust," *British Journal of Applied Physics*, vol. 9, no. 3, pp. 98–102, 1958.
- [28] S. E. Allaire and L.-E. Parent, "Size guide number and rosinrammler approaches to describe particle size distribution of granular organic-based fertilisers," *Biosystems Engineering*, vol. 86, no. 4, pp. 503–509, 2003.
- [29] W.-Z. Wang, Y.-M. Wang, G.-Q. Shi, and D.-M. Wang, "Numerical study on infrared optical property of diffuse coal particles in mine fully mechanized working combined with CFD method," *Mathematical Problems in Engineering*, vol. 2015, Article ID 501401, 10 pages, 2015.
- [30] W. Z. Wang, Y. M. Wang, and G. Q. Shi, "Experimental investigation on the infrared refraction and extinction properties of rock dust in tunneling face of coal mine," *Applied Optics*, vol. 54, no. 35, pp. 10532–10540, 2015.
- [31] X. Huang, X. Chen, Y. Shuai et al., "Heat transfer analysis of solar-thermal dissociation of  $\text{NiFe}_2\text{O}_4$  by coupling MCRTM and FVM method," *Energy Conversion and Management*, vol. 106, pp. 676–686, 2015.
- [32] H. Tan, L. Liu, H. Yi, J. Zhao, H. Qi, and J. Tan, "Recent progress in computational thermal radiative transfer," *Chinese Science Bulletin*, vol. 54, no. 22, pp. 4135–4147, 2009.
- [33] H.-L. Yi, C.-H. Wang, and H.-P. Tan, "Transient radiative transfer in a complex refracting medium by a modified Monte Carlo simulation," *International Journal of Heat and Mass Transfer*, vol. 79, pp. 437–449, 2014.
- [34] L. Ma, F. Wang, C. Wang, C. Wang, and J. Tan, "Monte Carlo simulation of spectral reflectance and BRDF of the bubble layer in the upper ocean," *Optics Express*, vol. 23, no. 19, pp. 24274–24289, 2015.
- [35] Y.-S. Sun, J. Ma, and B.-W. Li, "Spectral collocation method for convective-radiative transfer of a moving rod with variable thermal conductivity," *International Journal of Thermal Sciences*, vol. 90, pp. 187–196, 2015.
- [36] J. Ma, Y. Sun, B. Li, and H. Chen, "Spectral collocation method for radiative-conductive porous fin with temperature dependent properties," *Energy Conversion and Management*, vol. 111, pp. 279–288, 2016.

- [37] Z.-X. Jia, Y. Shuai, S.-D. Xu, and H.-P. Tan, "Optical coherent thermal emission by excitation of magnetic polariton in multilayer nanoshell trimer," *Optics Express*, vol. 23, no. 19, pp. A1096–A1110, 2015.
- [38] W. Z. Wang, Y. M. Wang, and G. Q. Shi, "Waveband selection within 400–4000  $\text{cm}^{-1}$  of optical identification of airborne dust in coal mine tunneling face," *Applied Optics*, vol. 55, no. 11, pp. 2951–2959, 2016.
- [39] P. Sadooghi and C. Aghanajafi, "Two-flux method for transient thermal analysis in a layer of polymer fiber," *Journal of Applied Polymer Science*, vol. 101, no. 4, pp. 2277–2283, 2006.

## Research Article

# Atmospheric Aerosols Detection Research with a Dual Field of View Lidar

Lv Lihui,<sup>1,2</sup> Zhang Tianshu,<sup>1</sup> Liu Cheng,<sup>2</sup> Dong Yunsheng,<sup>1</sup> Chen Zhenyi,<sup>1</sup>  
Fan Guangqiang,<sup>1</sup> Liu Yang,<sup>1,2</sup> and Liu Wenqing<sup>1,2</sup>

<sup>1</sup>Key Laboratory of Environmental Optics and Technology, Anhui Institute of Optics and Fine Mechanics,  
Chinese Academy of Sciences, Hefei, Anhui 230031, China

<sup>2</sup>University of Science and Technology of China, Hefei, Anhui 230031, China

Correspondence should be addressed to Liu Cheng; [chliu81@ustc.edu.cn](mailto:chliu81@ustc.edu.cn)

Received 25 August 2015; Revised 5 December 2015; Accepted 16 December 2015

Academic Editor: Dean S. Venables

Copyright © 2015 Lv Lihui et al. This is an open access article distributed under the Creative Commons Attribution License, which permits unrestricted use, distribution, and reproduction in any medium, provided the original work is properly cited.

A dual field of view lidar system with two independent receivers is described to realize the detection of atmospheric aerosols. A CCD camera is attached to a backscatter lidar as a receiver to complement the data in the near-field range affected by the incomplete overlap between the laser beam and the receiver field of view. The signal detected by the CCD camera is corrected and finally glued with the signal of the backscatter lidar to retrieve the aerosol extinction coefficient with Fernald algorithm. The aerosol extinction profile and visibilities measured by the dual field of lidar had been compared with the results measured by another general backscatter lidar and a surface aerosol instrument, respectively. The results suggested that the dual field of view lidar based on a CCD camera is feasible and reliable. It could obtain the data both in the near and in the far range simultaneously, improving the detection accuracy of the lidar system effectively.

## 1. Introduction

The atmospheric aerosols, especially the aerosols near-ground, have a large impact on the local and regional air quality and visibility, as well as the human health and public transport safety directly and indirectly. Therefore, it is of vital importance to detect the vertical distribution of atmospheric aerosols near the ground. As a powerful tool to detect the spatial distribution of atmospheric aerosols, lidar has been widely used in the field of atmospheric and environmental monitoring [1]. However, the incomplete overlap between the laser beam and the receiver field of view of the backscatter lidar significantly affects the observation of aerosol optical properties in the near-field range. So the backscatter lidar has a shortcoming in the lower hundreds of meters because of the geometric overlap factor [2]. In this paper, the problem is overcome by a dual field of view lidar based on a CCD camera.

Welsh and Gardner had verified the feasibility of a bistatic lidar that uses a CCD camera as the receiver in 1989 [3]. Then, the lidar based on a CCD camera is gradually used in the near-ground atmospheric aerosols detection [4–6]. However,

the application of the standard charge-coupled device camera lidar is limited in the near range. In this paper, a CCD camera is attached to a backscatter lidar to expand the detection range of the atmospheric aerosols in the near range. The CCD camera with large FOV is mainly used to detect the atmosphere in the near range and the receiver of the backscatter lidar is mainly used to detect the atmosphere in the far range. At last, the signals of the two receivers are glued and used to retrieve the whole range aerosol extinction properties.

## 2. System Structure

The configuration of the dual field of view lidar is shown in Figure 1 and the key specifications are given in Table 1. As illustrated in Figure 1, the CCD camera and telescope are separated by a distance  $D$  and the CCD camera is parallel to the axis of the telescope. The laser source was a pulsed Nd:YAG laser operating at a wavelength of 532 nm with a pulse repetition rate of 20 Hz. The CCD camera with  $3358 \times 2536$  active pixels was cooled to  $-10^\circ\text{C}$  to improve

TABLE 1: Key specifications of the dual field of view lidar.

Feature	Specification
<i>Laser: Nd:YAG</i>	
Wavelength	532 nm
Transmitter	Pulse energy 200 mJ
	Repetition frequency 20 Hz
	Divergence 0.5 mrad
<i>CCD camera</i>	
CCD:QHY9	
Pixels	3358 × 2536 (860 million)
Pixel size	5.4 μm × 5.4 μm
Active area	19.7 * 15.04 mm
Peak Quantum Efficiency	56%
Receiver	Wide-angle lens
	Angular field 114°
	Focal length 14 mm
	Max aperture F2.8
<i>Telescope: Cassegrain</i>	
Diameter	230 mm
Detector	PMT
Data acquisition	Photo counter
Range resolution	7.5 m

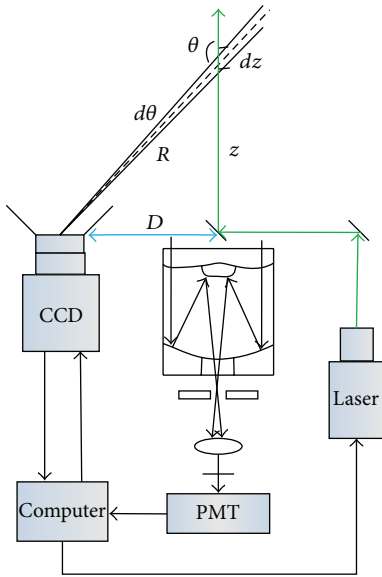


FIGURE 1: Configuration of the dual field of view lidar.

the resolution and reduce the noise. The FOV of the receiver which consists of a CCD and a wide-angle lens is about 75.4°.

In the dual field of view lidar system, the laser beam is emitted into the atmosphere vertically and then the scattered signal is detected by two receivers. The CCD camera records

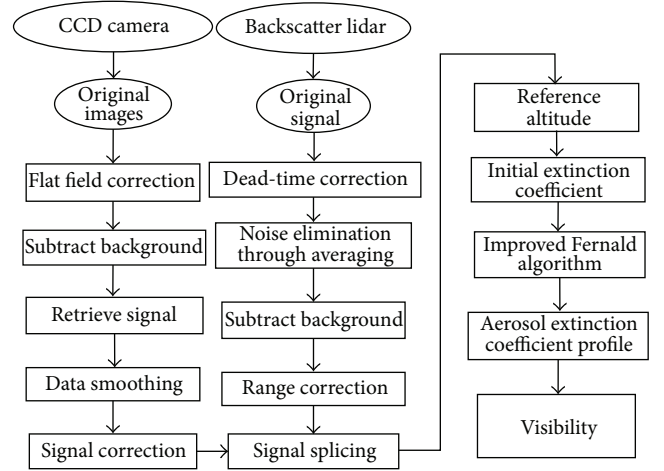


FIGURE 2: The flow chart of the data processing.

the signal in the form of image. From geometry, the resolution of the signal detected by the CCD camera is given simply by

$$z = -\frac{D}{\tan \theta}, \quad (1)$$

$$dz = \frac{R^2 d\theta}{D},$$

where  $d\theta$  is the FOV of each pixel. The CCD camera with large FOV is mainly used to detect the signal in the near range while the backscatter lidar with small FOV is mainly used to detect the signal in the far range. Finally, the signals are glued to retrieve the aerosol profiles.

### 3. Method

In the dual field of view lidar technique, some important parameters should be assumed in the CCD camera data retrieval and the most significant one is the exposure time, which has an important influence on the signal-to-noise ratio (SNR). Wang et al. [7] have pointed out the relationship between the signal-to-noise ratio (SNR) and exposure time of an astronomical CCD camera. It revealed that the SNR of the astronomical cooled CCD was proportional to the exposure time  $t$  when the exposure time  $t < t_c$  ( $t_c$  is approximately 3 s) while proportional to the square root of the exposure time  $t$  when the exposure time  $t > t_c$ . Besides, according to the signal theory, the SNR is proportional to the square root of the number of repetitions. All the analyses show that signal exposure mode with longer exposure time is more suitable when the total exposure time is ascertained. However, the signal will be saturated if the exposure time is too long. The exposure time in our experiment is set as 50 s.

The flow chart of the data processing is shown in Figure 2. First, a flat field calibration is applied to the images recorded by the CCD camera. Then the background is subtracted from the image with scattered signal to remove the influence of

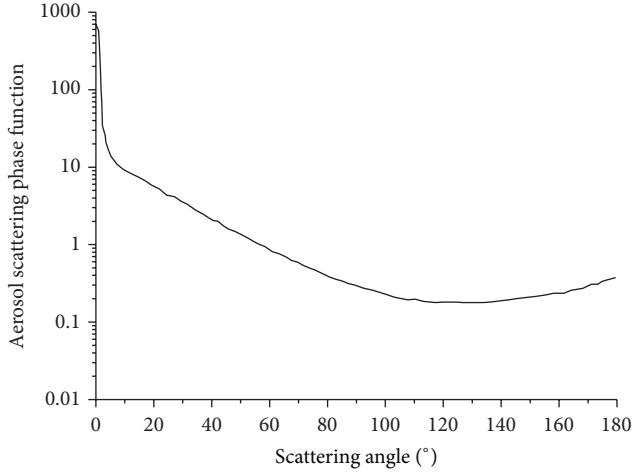
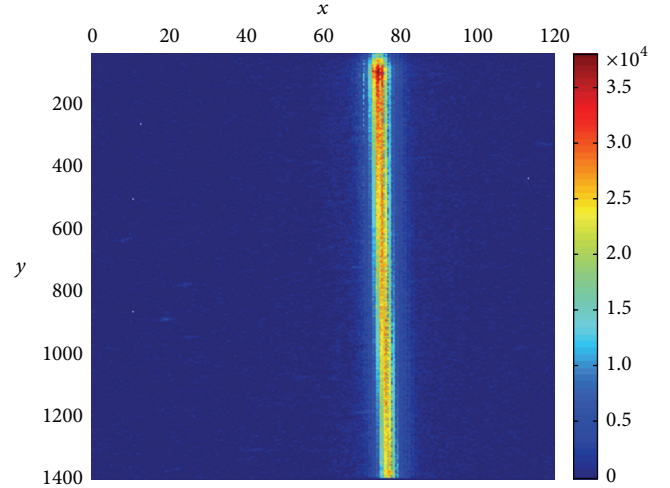


FIGURE 3: The curve of continental aerosol scattering phase function.

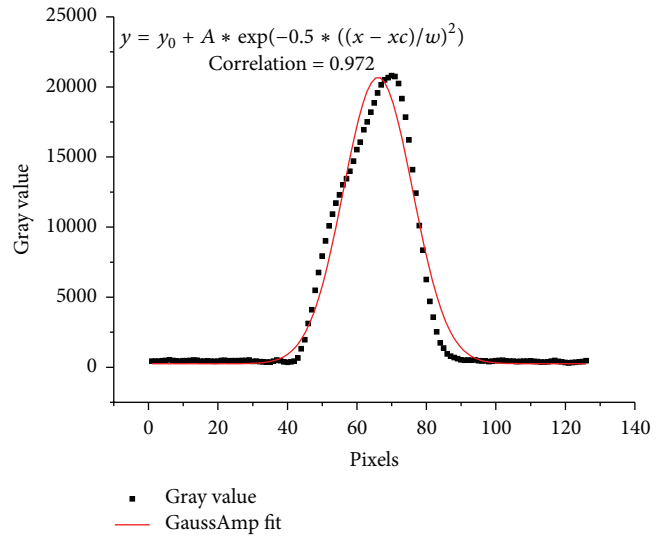
the background. The gray scale at each pixel is summed in the direction perpendicular to the telescope axis within a certain range to provide information of the atmospheric scattering. The altitude of the scattered signal is derived from the geometry of the laser and CCD camera locations. The signals detected by the CCD camera, unlike ones from the backscatter lidar, vary dramatically with the scattering angle  $\theta$  (it is always  $180^\circ$  for a backscatter lidar, whereas in the CCD technique, it varies with altitude), so the signals should be corrected based on the aerosol scattering phase function. Here we use the aerosol scattering phase function [8] (calculated from the second simulation of the satellite signal in the solar spectrum) which is shown in Figure 3. In the dual field of view lidar system, the CCD camera receives the scattering signal in the range  $143^\circ \sim 180^\circ$ . The signal detected by the CCD camera is converted to the  $180^\circ$  with the aerosol scattering phase function and then glued with the signal acquired by the backscatter lidar.

The signal gluing theory is an ideal method to solve the problems of signal saturation in the near range and low SNR in the far range [9] in the backscatter lidar. Here the signal detected by the CCD camera and the photo counting signal detected by the backscatter lidar are glued. The main steps of the signal splicing procedure can be summarized as follows [10]: first, the fitting area where both the signals have higher SNR and better linearity should be selected; then the best gluing area is chosen with standards of justification to fit the two groups of signals and finally the signals are spliced with the parameters obtained from the linear fitting curve.

In order to guarantee the SNR of the signal in fitting area, the range of signals depends on the effective detection range of the CCD camera and the backscatter lidar. Some research has suggested that the distribution function of the laser beam images recorded by the CCD is characteristic of Gaussian curve, so the SNR at each altitude can be calculated with the Gaussian distribution formula [11]. The two-dimensional image of the laser beam is shown in Figure 4(a), in which the beam direction is parallel to the  $y$  axis and the color level



(a)



(b)

FIGURE 4: (a) Two-dimensional image of the laser beam. (b) The scatter diagram of the pixels and its corresponding gray scales perpendicular to the direction of the laser beam.

represents the intensity of the received signal. Figure 4(b) shows the scatter diagram of the pixels and its corresponding gray scales at some altitude. We can obtain the SNR of the signal received by the CCD camera by fitting the scatter plot with Gaussian formula. The SNR can be calculated as

$$\text{SNR} = \frac{N_s}{N_n} = \frac{\sqrt{2\pi}Aw}{\sqrt{2\pi}w\gamma_0} = \frac{A}{\gamma_0}. \quad (2)$$

In the fitting area, the correlation coefficient is calculated with a sliding window to select the best splicing area where the correlation is the highest. We should point out that the backscatter lidar has constant resolution of 7.5 m, whereas the resolution of the CCD imaging lidar varies with altitudes. So we need to compare the resolution of the two groups of signals and interpolate the lower one to another before

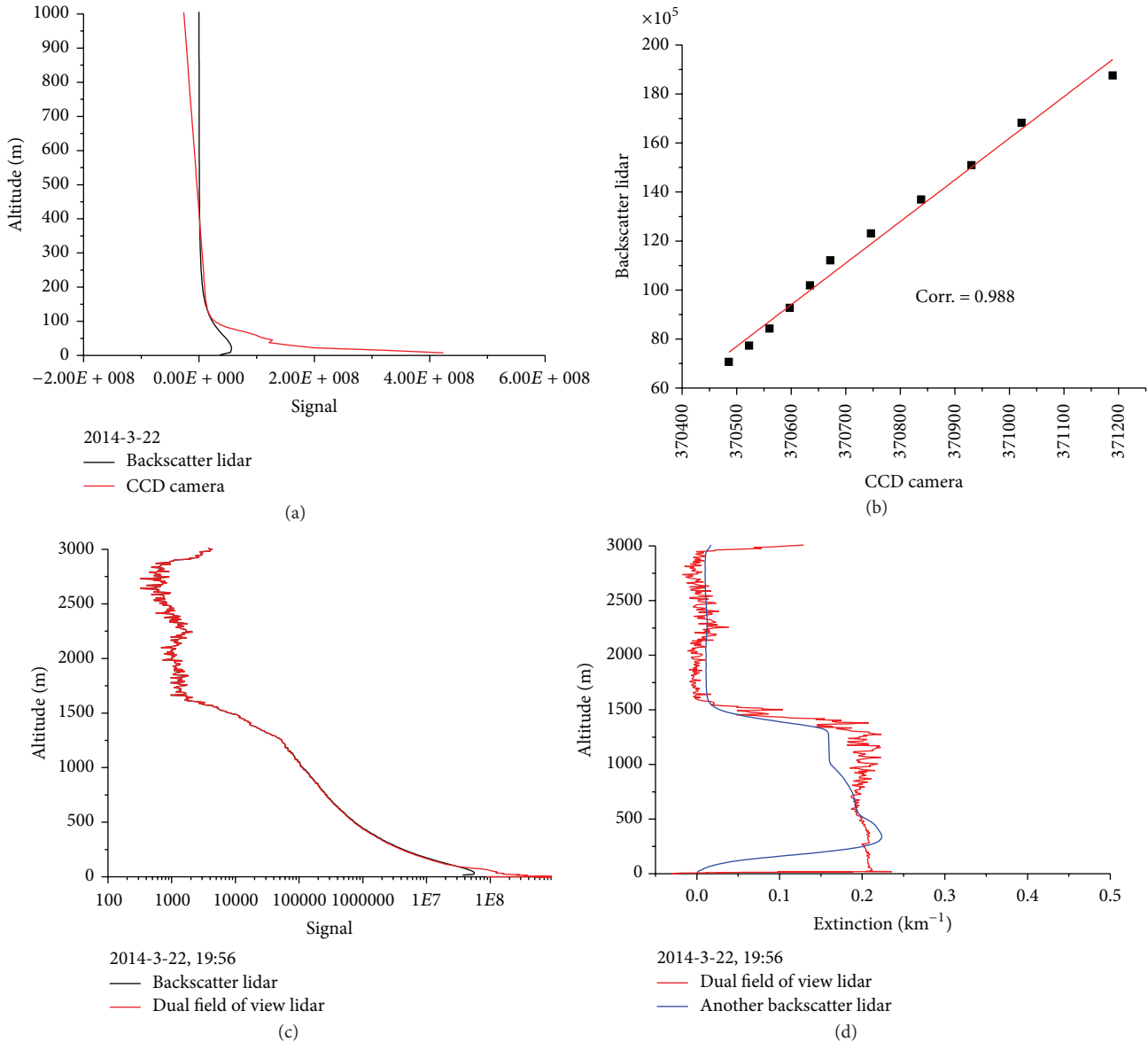


FIGURE 5: (a) The original signals received by the two receivers of the dual field of view lidar. (b) The correlation analysis in the range of 220–300 m. (c) Comparison of the gluing signal and original backscatter lidar signal received by the telescope. (d) Comparison of extinction coefficient profiles.

calculating the correlation coefficient of each window. Finally, the two groups of signals are fitted in the best splicing area and the fitting parameters are applied to the whole signal of the CCD camera to splice it with the photo counting signal received by the backscatter lidar. The spliced signal not only includes the near-ground data, but also takes the detection range into account, so the method can detect the distribution of atmospheric aerosols effectively.

The Fernald algorithm is usually used to invert the aerosol profiles [12]. The key point of the algorithm is to determine the reference point and its initial value. The conventional Fernald algorithm often selects the clear aerosol-free altitude of the atmosphere as the reference point and calculates its initial value with the standard atmospheric model.

But sometimes the clear altitude does not exist in the detection path, so here an improved Fernald algorithm is utilized to invert the aerosol extinction coefficient. Specifically the subslope method is used to determine the reference point and its initial value, and then the result is substituted into the Fernald formula to solve the aerosol profile [13].

#### 4. Experimental Results

The observation experiment was carried out at night to avoid the impact of background. Figure 5(a) shows the original signals received by the two receivers of the dual field of view lidar. As shown in Figure 5(a), the signals of the two receivers have a good agreement in the range of 220–300 m.

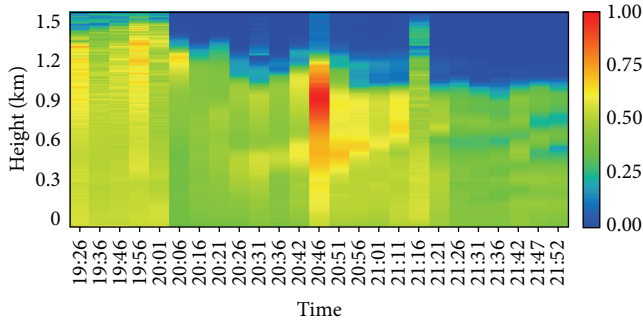


FIGURE 6: The distribution of aerosol extinction coefficient on March 22.

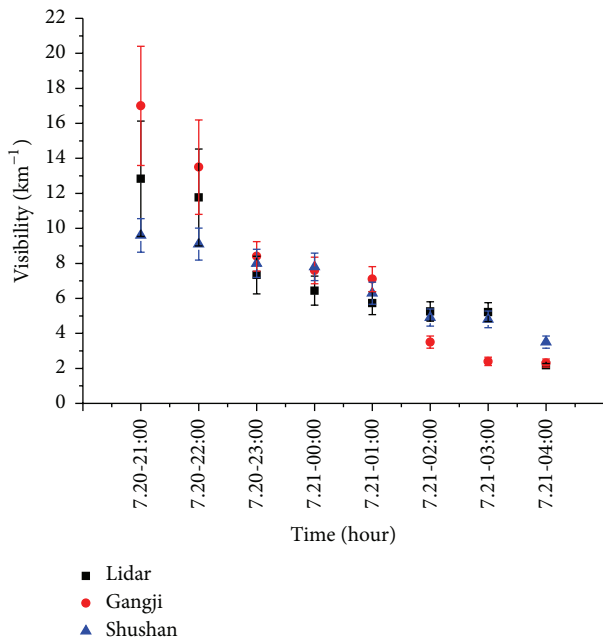
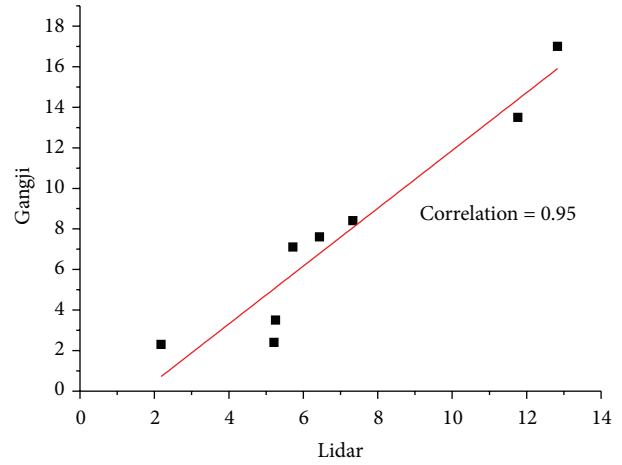


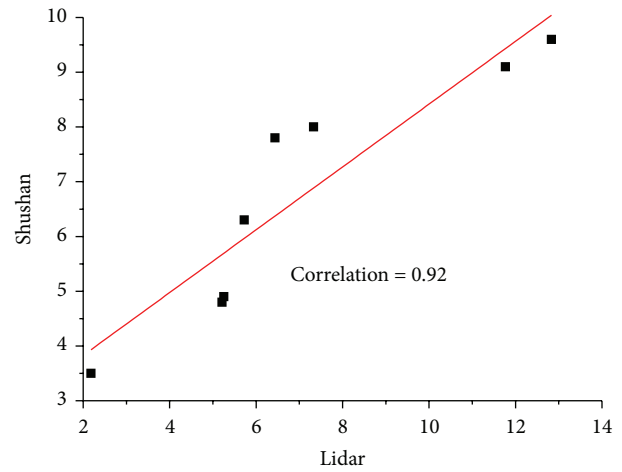
FIGURE 7: The comparison diagram of the visibility measured by the dual field of view lidar and forward scatter visibility meter.

The correlation analysis result shown in Figure 5(b) suggests that this area can be selected as the fitting area. Figure 5(c) shows the comparison of the gluing signal and the original backscatter lidar signal received by the telescope. Figure 5(d) shows the profiles of aerosol extinction coefficient retrieved by the dual field of view lidar system and another backscatter lidar which was placed near the dual field of view lidar. The final result shows that the splicing signal can inverse the aerosol distribution effectively in the near range.

Figure 6 presented the distribution of aerosol extinction coefficient from 19:30 to 22:00 on March 22. During the experiment the extinction coefficient decreased gradually in the period from 19:30 to 20:30 and increased but then decreased gradually in the range of 0.3–1.2 km later. In addition, the figure shows that the result inverted from the splicing signal presents a better distribution of aerosols in



(a)



(b)

FIGURE 8: (a) The correlation analysis of the visibility measured by the dual field of view lidar and a forward scatter visibility meter located at Gangji station. (b) The correlation analysis of the visibility measured by the dual field of view lidar and a forward scatter visibility meter located at Shushan station.

the lower hundreds of meters, indicating the advantages of the dual field of view lidar system.

Furthermore the visibility measured by the dual field of view lidar was compared with the ones from a forward scatter visibility meter. In Figure 7, the square data represents the visibility [14] measured by the dual field of view lidar, and the circular and triangular data represent the visibility of Gangji and Shushan stations. The stations are all located within a radius of 6 kilometers from the site of the lidar. From the figure, we can see that the three curves are all tending to decline and the results have little difference during the experimental period. Figures 8(a) and 8(b) further, respectively, show that the correlativity of the visibility measured by the dual field of view lidar system and forward scatter visibility meter is above 90%, so the dual field of view lidar can measure the visibility accurately and effectively.

## 5. Conclusion

In conclusion, we introduce a new method for the aerosol detection with a dual field of view lidar system. A CCD camera is used to detect the lower atmosphere and a backscatter lidar is used to detect the higher atmosphere; finally the signals are spliced to invert the extinction coefficient profiles. CCD camera has the characteristics of high dynamic and high resolution near-ground, compensating the data of the blind and transition zone of the backscatter lidar. The signal spliced not only includes the near-ground data, but also takes the detection range into account, so the method can detect the distribution of atmospheric aerosols effectively. In addition, the improved Fernald algorithm is used to invert the extinction coefficient profiles and the result is compared with the previous algorithm. The final result suggests that the improved algorithm is reasonable and effective. We have basically realized the no-blind aerosol detection with the dual field of view lidar system. Currently the dual field of view lidar technique is limited to use in night, so a further solution should be discussed to solve the background during the day.

## Conflict of Interests

The authors declare that there is no conflict of interests regarding the publication of this paper.

## Acknowledgments

This work was supported by the National Natural Science Foundation of China (no. 41305126), National Natural Science Foundation of China (no. 41205119), Key Project of Chinese National Programs for Fundamental Research and Development (973 Program) (Grant 2014CB447900), and the State Plan for High-Tech Research and Development (863 Program) (Grant 2014AA06A512).

## References

- [1] C. Weitkamp, *Lidar: Range-Resolved Optical Remote Sensing of the Atmosphere*, vol. 102 of *Springer Series in Optical Sciences*, Springer, New York, NY, USA, 2005.
- [2] T. Halldorsson and J. Langerholc, "Geometrical form factors for the lidar function," *Applied Optics*, vol. 17, no. 2, pp. 240–244, 1978.
- [3] B. M. Welsh and C. S. Gardner, "Bistatic imaging lidar technique for upper atmospheric studies," *Applied Optics*, vol. 28, no. 1, pp. 82–88, 1989.
- [4] K. Meki, K. Y. Yamaguchi, X. Li, Y. Saito, T. D. Kawahara, and A. Nomura, "Range-resolved bistatic imaging lidar for the measurement of the lower atmosphere," *Optics Letters*, vol. 21, no. 17, pp. 1318–1320, 1996.
- [5] J. E. Barnes, S. Bronner, R. Beck, and N. C. Parikh, "Boundary layer scattering measurements with a charge-coupled device camera lidar," *Applied Optics*, vol. 42, no. 15, pp. 2647–2652, 2003.
- [6] Z. Wang, Z. Tao, D. Liu, D. Wu, C. Xie, and Y. Wang, "New experimental method for lidar overlap factor using a CCD side-scatter technique," *Optics Letters*, vol. 40, no. 8, pp. 1749–1752, 2015.
- [7] S.-H. Wang, M.-F. Hu, and Z.-P. Chen, "Noise analysis and the study of SNR model on the astronomical CCD camera," *Semiconductor Optoelectronics*, vol. 28, no. 5, pp. 731–734, 2007.
- [8] E. Vermote, *Second Simulation of the Satellite Signal in the Solar Spectrum*, 6S User Guide Version 2, 1997.
- [9] D. N. Whiteman, B. Demoz, P. Di Girolamo et al., "Raman lidar measurements during the international H<sub>2</sub>O project. Part I: instrumentation and analysis techniques," *Journal of Atmospheric and Oceanic Technology*, vol. 23, no. 2, pp. 157–169, 2006.
- [10] H. Lifeng, G. Wei, L. Jun et al., "Signal splicing of dual-receiver Mie scattering lidar in atmospheric remote sensing," *Journal of Remote Sensing*, vol. 16, no. 4, pp. 712–719, 2012.
- [11] J. E. Barnes, N. C. Parikh Sharma, and T. B. Kaplan, "Atmospheric aerosol profiling with a bistatic imaging lidar system," *Applied Optics*, vol. 46, no. 15, pp. 2922–2929, 2007.
- [12] F. G. Fernald, "Analysis of atmospheric lidar observations: some comments," *Applied Optics*, vol. 23, no. 5, pp. 652–653, 1984.
- [13] Q. Du, Y. Ji, and C. Xu, "Data processing method of aerosol horizontal distribution detected by MPL," *Journal of Atmospheric and Environmental Optics*, vol. 3, no. 1, pp. 23–27, 2008.
- [14] X. Chengbo, H. Yong, L. Chao et al., "The vehicle-mounted Lidar used for atmospheric horizontal visibility measurement," *High Power Laser and Particle Beams*, vol. 17, no. 7, pp. 971–975, 2005.

## Research Article

# Multi-Quartz Enhanced Photoacoustic Spectroscopy with Different Acoustic Microresonator Configurations

Huadan Zheng,<sup>1,2</sup> Xukun Yin,<sup>1,2</sup> Lei Dong,<sup>1,2</sup> Hongpeng Wu,<sup>1,2</sup> Xiaoli Liu,<sup>1,2</sup>  
Weiguang Ma,<sup>1,2</sup> Lei Zhang,<sup>1,2</sup> Wangbao Yin,<sup>1,2</sup> and Suotang Jia<sup>1,2</sup>

<sup>1</sup>State Key Laboratory of Quantum Optics and Quantum Optics Devices, Institute of Laser Spectroscopy, Shanxi University, Taiyuan 030006, China

<sup>2</sup>Collaborative Innovation Center of Extreme Optics, Shanxi University, Taiyuan 030006, China

Correspondence should be addressed to Lei Dong; donglei@sxu.edu.cn

Received 16 September 2015; Accepted 22 October 2015

Academic Editor: Arnaud Cuisset

Copyright © 2015 Huadan Zheng et al. This is an open access article distributed under the Creative Commons Attribution License, which permits unrestricted use, distribution, and reproduction in any medium, provided the original work is properly cited.

Acoustic microresonators were added to the recently developed multi-QTF based QEPAS spectrophone to enhance the signal amplitude. Two kinds of “on-beam” configurations were experimentally investigated in detail. The developed multi-QTF based “on-beam” spectrophone had a signal enhancement of 1.6 times compared with the traditional single QTF based “on-beam” spectrophone, with the approximate noise level. A normalized noise equivalent absorption coefficient ( $1\sigma$ ) of  $1.24 \times 10^{-9} \text{ W}\cdot\text{cm}^{-1}\cdot\text{Hz}^{-1/2}$  was obtained for water vapor detection at atmospheric pressure.

## 1. Introduction

Laser absorption spectroscopy for trace gas detection has gained considerable interest over the past decades. Among optical spectroscopic techniques, photoacoustic spectroscopy (PAS) is a well-established sensitive approach, with the advantages of zero-background nature, excitation-wavelength independence, and linear dependence of signal amplitudes on excitation powers [1–4]. As a variation of PAS, quartz enhanced photoacoustic spectroscopy (QEPAS), by use of a quartz tuning fork (QTF) instead of a traditional microphone, is a booming technique for trace gas detection that has been widely used for environmental monitoring, industrial process control analysis, combustion processes, and detection of toxic and flammable gases, as well as explosives [5]. The sharply high Q value of the quartz tuning fork (QTF) not only facilitates the accumulation of the acoustic energy generated from the relaxation transition of gas molecules, but also makes the QEPAS based spectrophone immune to environmental noise.

Acoustic microresonators (AmRs) were usually used in QEPAS spectrophone to enhance the acoustic wave oscillation, induced by the modulated beam in the absorbing gas, by

virtue of the coupling effects between the QTF and the AmRs [6–8]. Two sophisticated QEPAS spectrophones with AmRs assembled in “on-beam” and “off-beam” configurations have been developed to improve the performance of bare-QTF based QEPAS sensors [9, 10]. The spectrophone assembled in the “on-beam” configuration [9], with two AmRs positioned closely on each side of the QTF, offers a signal-to-noise ratio (SNR) enhancement factor of  $\sim 30$ . The spectrophone assembled in the “off-beam” configuration [10], having a single AmR with a small slit made in the middle placed alongside the QTF, can simplify optical alignment and be applied to excitation sources with a low spatial radiation quality. Recently, some novel QEPAS spectrophones were also reported. Double acoustic microresonator quartz-enhanced photoacoustic spectroscopy which employed the spectrophone that consisted of a QTF and two sets of the “on-beam” AmRs was developed for optical signal addition and multigas rapid spectral measurement with a response time of 5 ms [1]. Multi-quartz enhanced photoacoustic spectroscopy (M-QEPAS) uses a pair of QTFs with similar resonance frequencies connected in parallel, instead of a single QTF in the traditional QEPAS spectrophone, to enhance the signal amplitude through coupling effect between the two QTFs [11].

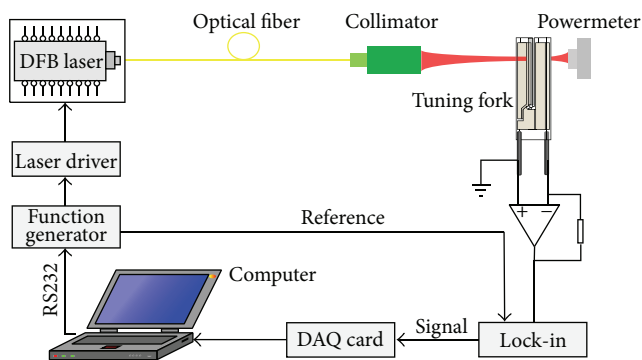


FIGURE 1: Schematic of the experimental setup.

M-QEPAS realized a 1.7 times signal enhancement for the water vapor detection in the air, compared to the QEPAS sensor with a single bare QTF. But there were no AmRs configured in the M-QEPAS spectrophone.

In this paper, AmRs were added to the M-QEPAS spectrophone to further enhance the signal amplitude of the sensor. Two kinds of multi-QTF based “on-beam” QEPAS spectrophone were proposed. The resonance curves of the proposed QEPAS spectrophones were measured to determine their resonance frequencies and Q values. For its practical implementation, water vapor in the laboratory air was selected as the target analyte to evaluate the sensor performance in detail. The distance between the AmR and the QTF in the multi-QTF based “on-beam” QEPAS spectrophone was optimized to obtain the maximum signal amplitude.

## 2. Experimental Setup

The schematic diagram of the experimental setup was depicted in Figure 1. A near-infrared fiber-coupled distributed-feedback (DFB) diode laser was employed as excitation source to generate photoacoustic signals. The output wavelength of the DFB laser was 1368.69 nm, with the temperature and the current of the DFB laser set to 27°C and 80 mA. The laser wavelength can be coarsely and finely tuned by scanning the temperature and the current, respectively. A commercial ~32 kHz quartz tuning fork was used as an acoustic transducer. The laser current was modulated at ~16 kHz, corresponding to a half of the QTF resonance frequency. The output beam from the DFB laser was focused to pass through the gap between the QTF prongs by means of a fiber coupled focuser. The acoustic wave induced by the modulated laser beam effectively pushed the prongs of the QTF to vibrate. The electrical signals generated by piezoelectric effect of the QTF were processed by a transimpedance preamplifier and then were fed to a lock-in amplifier, demodulating the signal at  $2f$  mode and retrieving the gas concentrations.

The output power and wavelength of the DFB laser as a function of current were plotted in Figure 2. The current of the DFB laser was scanned from 15 mA to 125 mA at a constant temperature of 23.95°C, corresponding to a wavelength range from  $7305.8\text{ cm}^{-1}$  to  $7309.9\text{ cm}^{-1}$ . Two  $\text{H}_2\text{O}$  absorption lines, located at  $7306.75\text{ cm}^{-1}$  and  $7308.82\text{ cm}^{-1}$ , were

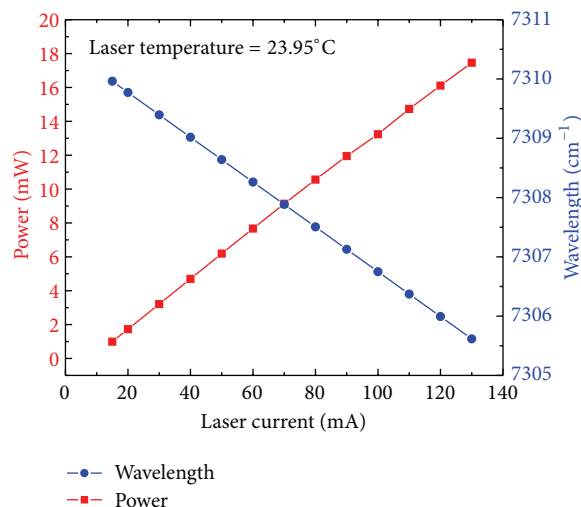


FIGURE 2: Output power and wavelength of the laser as a function of current.

covered within the scanning range. According to the HITRAN database, the two  $\text{H}_2\text{O}$  absorption lines have the line intensities of  $1.8 \times 10^{-20}\text{ cm/mol}$  and  $6.9 \times 10^{-22}\text{ cm/mol}$ , respectively, as shown in Figure 3(a). The relevant  $2f$  signal, obtained from the QEPAS sensor by use of the spectrophone based on a bare QTF, was shown in Figure 3(b). A lower detection limit can be achieved by selecting a stronger target line, but to avoid the overload of the lock-in amplifier, the weaker line at  $7308.82\text{ cm}^{-1}$  was selected as the target line in this experiment.

Figure 4 shows four different QEPAS spectrophones: (a) single bare QTF based spectrophone, (b) traditional single QTF based “on-beam” spectrophone, and (c), (d) multi-QTF based “on-beam” spectrophones. In Figure 4(c), two QTFs were placed in a line with a gap of  $20\text{ }\mu\text{m}$ , and two AmRs were positioned closely on the one side of each QTFs with the same gap of  $20\text{ }\mu\text{m}$ . The distance from the top of the QTF prongs to the center of the AmRs was  $0.7\text{ mm}$ . In Figure 4(d), an additional QTF was added to a traditional single QTF based “on-beam” spectrophone. The distance from the top of the QTF prongs to the center of the AmRs and the gaps between the QTF #3 and the AmRs were the same as in Figure 4(c). This configuration is equivalent to two traditional half “on-beam” spectrophones connected in series [12]. The geometric parameters of all the AmRs used in Figures 4(b)–4(d) are the same as in [13].

## 3. Results and Discussion

A function generator was used to generate sinusoidal waves to excite the QTF, and the output signals of the QTF at different excitation frequencies were recorded as the resonance curves. The resonance frequency  $f_0$  and Q value of the QTF can be obtained from Lorentz fitting of the square of the resonance curve [14]. The Q value is defined as  $f_0/\Delta f$ , where  $\Delta f$  represents the full width at half maximum (FWHM) of the resonance curve. The resonance curve of the single bare

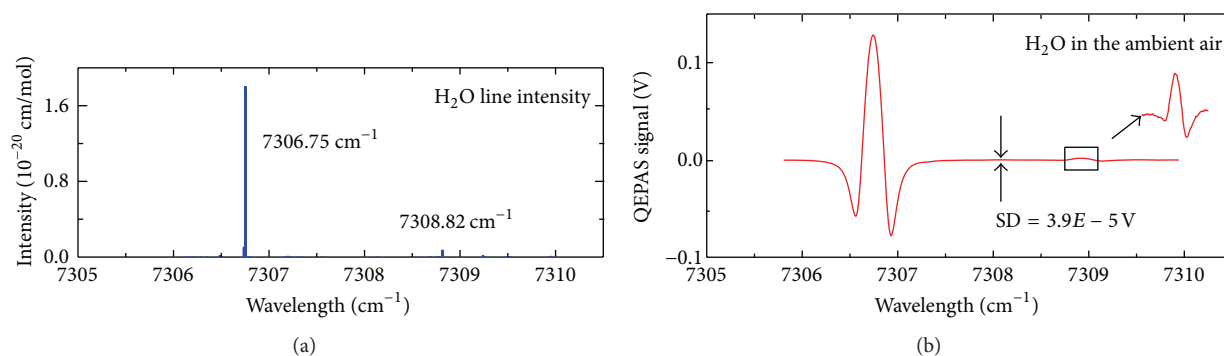


FIGURE 3: (a) Locations and intensities of H<sub>2</sub>O absorption lines from the HITRAN database; (b) 2f signal obtained from the QEPAS sensor by use of a single bare QTF based spectrophone; SD: standard deviation.

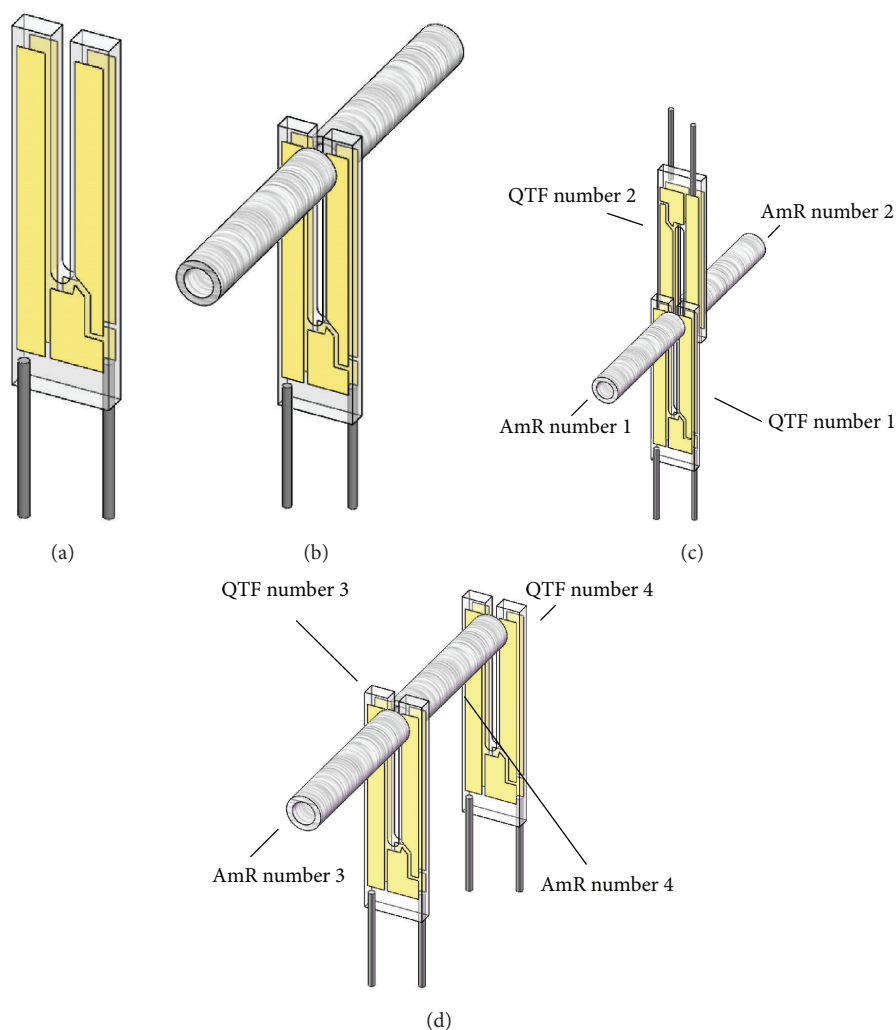


FIGURE 4: (a) Single bare QTF based spectrophone, (b) single QTF based "on-beam" spectrophone, and (c), (d) multi-QTF based "on-beam" spectrophones. The geometric parameters of all the AmRs used in Figure 4 are 4.4 mm in length and 0.6 mm in inner diameters, respectively.

QTF based spectrophone (Figure 4(a)) and the traditional single QTF based "on-beam" spectrophone (Figure 4(b)) were shown in Figure 5. The frequency of the sinusoidal wave from the function generator was scanned from 32720 Hz to 32780 Hz with peak to peak amplitude of 317 mV. A standard

QTF has the resonance frequency of 32768 Hz and Q value of 80,000–100,000 in a sealed vacuum metallic package. The frequency and the Q value decreased to 32748.8 Hz and 8396 in the air, after removal of the metallic housing. With the traditional single QTF based "on-beam" QEPAS

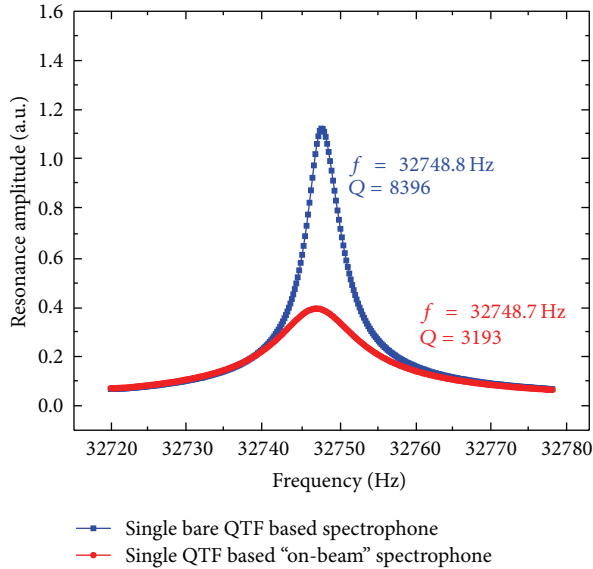


FIGURE 5: Resonance curves of a single bare QTF based spectrophone and a traditional single QTF based “on-beam” spectrophone measured at atmospheric pressure in the air.

TABLE 1: Parameters of multi-QTF based “on-beam” spectrophone (Figure 4(c)).

	QTF #1	QTF #2	Multi-QTF
Resonance frequency (Hz)	32747.29	32744.15	32746.93
Q value	5660	2923	6918

spectrophone, the Q factor further decreased to 3193, due to the strong coupling effect between the QTF and AmRs. The lower Q value means more acoustic energy exchange and storage between the QTF and the AmRs.

The performance of the multi-QTF based “on-beam” spectrophone shown in Figure 4(c) was first evaluated. The resonance curves of both QTFs were measured independently, and the corresponding parameters were listed in Table 1. QTFs #1 and #2 showed the approximate frequency. As a result, only one peak value on the response curve was observed, after connecting the electrodes of the two QTFs in parallel. The Q value of 5660 and 2923 for each QTF indicated that both the QTFs were coupled with the AmRs independently. Due to the strong coupling effect between the multi-QTF and the AmRs, the multi-QTF based “on-beam” spectrophone, shown in Figure 4(c), exhibited a Q value of 6918. Figure 6 shows the resonance curves obtained for QTF #1, QTF #2, and multi-QTF using the configuration of Figure 4(c), indicating that when two QTFs were connected in parallel and strongly coupled with the AmRs, Q-factor of multi-QTFs can be higher than each of the two QTFs.

The modulation depth of the laser was optimized with the bare QTF based spectrophone. The laboratory air containing 1.26% H<sub>2</sub>O was selected as the target analyte. The signal amplitudes and spectral profiles of the QEPAS 2f signal as a function of laser modulation depth were plotted in Figures 7(a) and 7(b). As shown in Figures 7(a) and 7(b), with

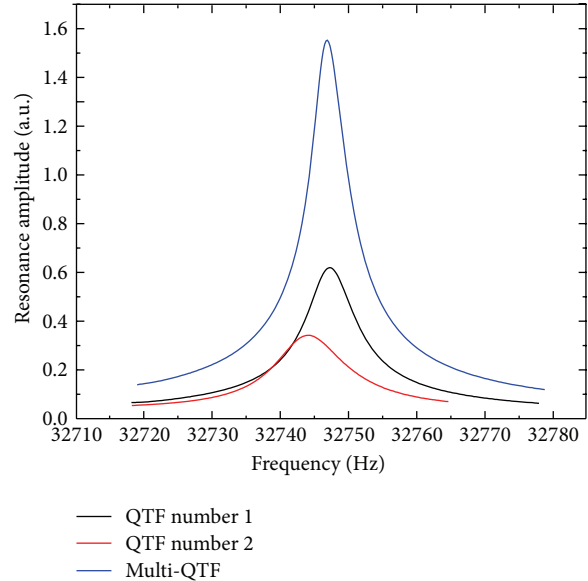


FIGURE 6: Resonance curves obtained for QTF #1, QTF #2, and Multi-QTF using the configuration of Figure 4(c).

TABLE 2: Parameters of multi-QTF based “on-beam” spectrophone (Figure 4(d)).

	QTF #3	QTF #4	Multi-QTF
Resonance frequency (Hz)	32744.93	32746.96	32745.68
Q value	5384	5540	5714

the modulation depth increasing from 5 to 20 mA, both the amplitude and spectra width of the QEPAS signal increased monotonously. However, with the modulation depth increasing from 13 to 20 mA, the signal amplitude increased only 9.4% (from 1.71 mV to 1.96 mV), shown in inset (j), but the spectra width increased 43.6% (from 0.44 cm<sup>-1</sup> to 0.63 cm<sup>-1</sup>), shown in inset (i). Therefore, an optimum modulation depth of 13 mA was selected, considering the spectral broadening.

QTFs #1 and #2 were first evaluated independently. The obtained signals were demonstrated in Figure 8(a). QTFs #1 and #2 showed the signal amplitudes of 41.5 mV and 37.5 mV which are 23.3 times and 21 times higher than that of the single bare QTF based spectrophone. This indicates that both QTFs #1 and #2 were strongly coupled with the AmRs assembled in the “on-beam” configuration. The QEPAS signal, obtained with the two QTFs’ electrodes connected in parallel, was also plotted in Figure 8(a). As a result, the multi-QTF based “on-beam” spectrophone showed the signal amplitude of 58.8 mV, yielding a 1.4 times enhancement compared to the traditional single QTF based “on-beam” spectrophone and a 33 times enhancement compared to the single bare QTF based spectrophone. The asymmetry of the signal was due to the residual amplitude modulation of the laser [15].

The performance of the multi-QTF based “on-beam” spectrophone in Figure 4(d) was evaluated in the same way. The comparisons in the resonance curves and the signal amplitudes were shown in Table 2 and Figure 8(b), respectively. In contrast with the spectrophone in Figure 4(c), the

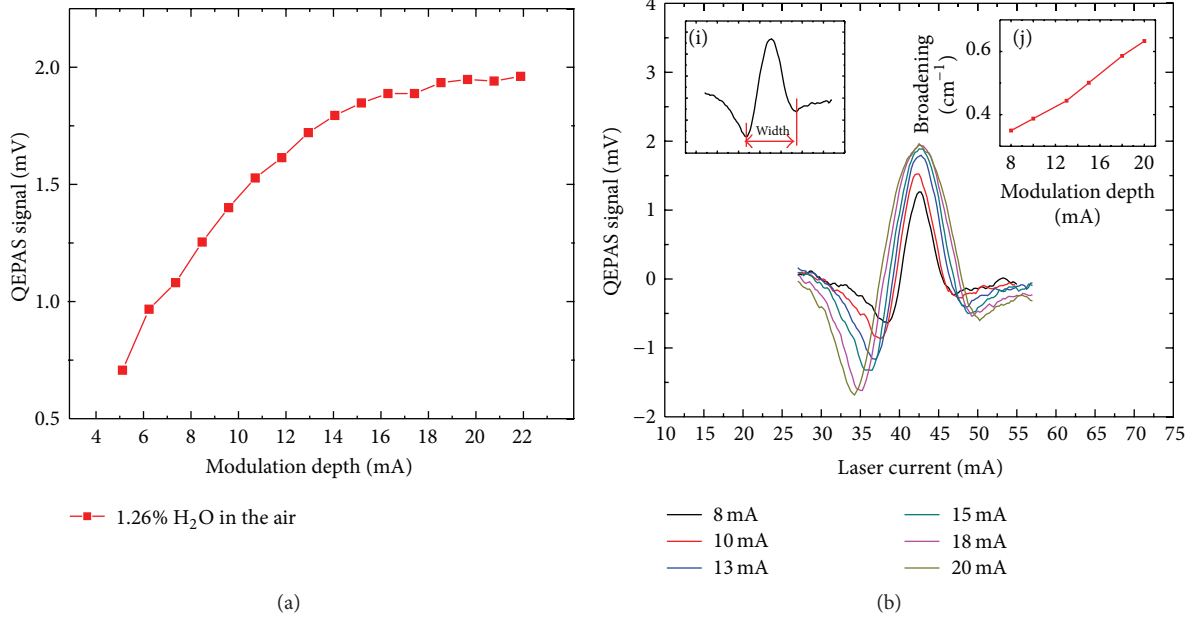


FIGURE 7: (a) QEPAS signal amplitudes as a function of laser modulation depth; (b) spectral broadening widths of QEPAS signal as a function of laser modulation depth.

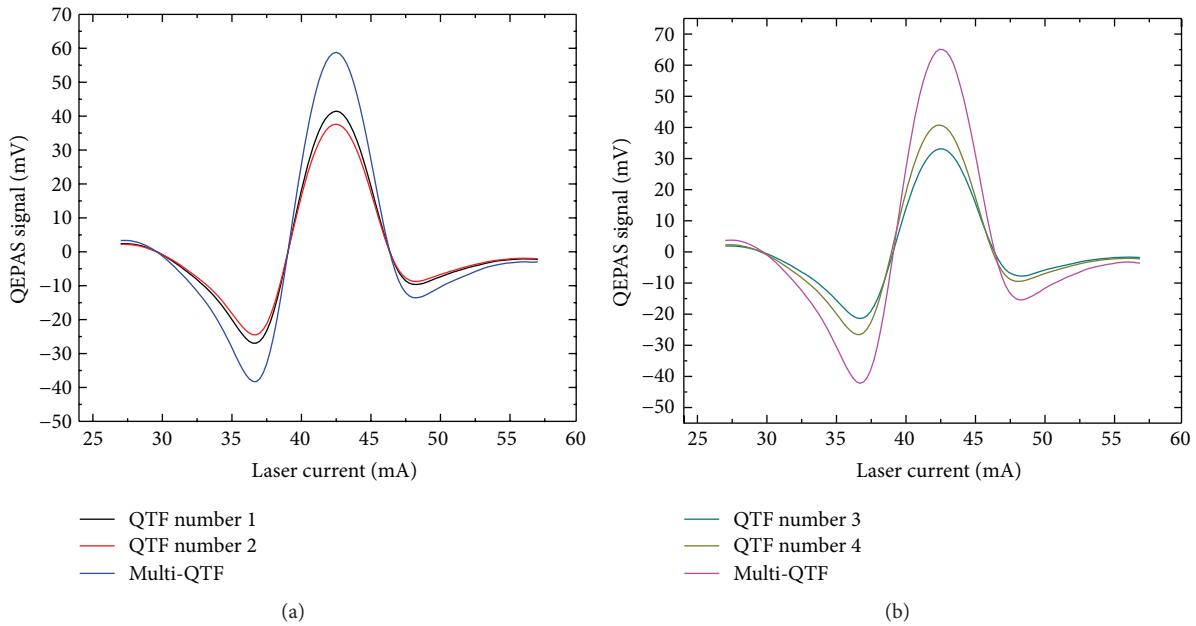


FIGURE 8: (a) Performance of multi-QTF based “on-beam” spectrophone shown in Figure 4(c); (b) performance of multi-QTF based “on-beam” spectrophone shown in Figure 4(d).

multi-QTF based “on-beam” spectrophone in Figure 4(d) generated a signal amplitude of 65.1 mV which is 1.6 times higher than that of the traditional single QTF based “on-beam” spectrophone and 36 times higher than that of the single bare QTF based spectrophone. Considering the higher signal gain, the multi-QTF based “on-beam” spectrophone in Figure 4(d) is preferred.

The QEPAS signal amplitude of the multi-QTF based “on-beam” spectrophone (Figure 4(d)) as a function of distance

between QTF #4 and AmR #4 was optimized and shown in Figure 9. With the distance increasing from 10 to 50  $\mu\text{m}$ , the signal amplitudes achieve the maximum value of 65.1 mV at the distance of 40  $\mu\text{m}$ , as shown in the inset of Figure 9. This observed behavior is due to the coupling effect of the acoustic wave fields between QTF #4 and the AmRs. The signal-to-noise ratio (SNR) of the sensor can be calculated from the  $2f$  signal maximum value and the noise background level obtained by tuning the laser wavelength far away from

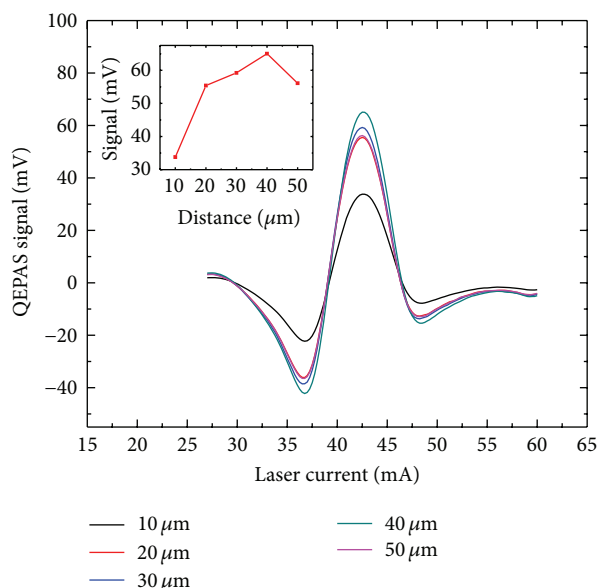


FIGURE 9: Signal amplitudes of the multi-QTF based “on-beam” spectrophone (Figure 4(d)) as a function of distance between QTF #4 and AmR #4.

the  $\text{H}_2\text{O}$  absorption lines. With the  $1\sigma$  noise of  $4.6 \times 10^{-5}$  V, the SNR of the multi-QTF based “on-beam” spectrophone (Figure 4(d)) is 1410, corresponding to a detection limit of 9.96 ppm. Normalized to the excitation power of 5.4 mW and the detection bandwidth of 0.125 Hz, the obtained  $1\sigma$  normalized noise equivalent absorption (NNEA) coefficients were  $1.24 \times 10^{-9} \text{ W}\cdot\text{cm}^{-1}\cdot\text{Hz}^{-1/2}$ .

#### 4. Conclusions

Acoustic microresonators are added to the most recently developed multi-QTF based QEPAS sensor to further enhance the signal amplitude. Two kinds of multi-QTF based spectrophones with “on-beam” AmR configurations were experimentally investigated and discussed. Compared with the traditional single QTF based “on-beam” spectrophone, the developed multi-QTF based “on-beam” spectrophone had a signal enhancement of 1.6 times at the same operating conditions, with the approximate noise level. A normalized equivalent absorption coefficient ( $1\sigma$ ) of  $1.24 \times 10^{-9} \text{ W}\cdot\text{cm}^{-1}\cdot\text{Hz}^{-1/2}$  was obtained for water vapor detection at normal atmospheric pressure. The signal enhancement can be further improved by using a phase shifter to adjust the possible phase difference between the multi-QTFs.

#### Conflict of Interests

The authors declare that there is no conflict of interests regarding the publication of this paper.

#### Acknowledgments

The work was supported by the 973 program (Grant no. 2012CB921603), the National Natural Science Foundation of

China (Grant nos. 61575113, 61275213, 61108030, 61475093, 61127017, 61178009, 61378047, and 61205216), the National Key Technology R&D Program (2013BAC14B01), the Shanxi Natural Science Foundation (2013021004-1), and the Shanxi Scholarship Council of China (2013-011, 2013-01).

#### References

- [1] L. Dong, H. Wu, H. Zheng et al., “Double acoustic microresonator quartz-enhanced photoacoustic spectroscopy,” *Optics Letters*, vol. 39, no. 8, pp. 2479–2482, 2014.
- [2] H. Wu, L. Dong, H. Zheng et al., “Enhanced near-infrared QEPAS sensor for sub-ppm level  $\text{H}_2\text{S}$  detection by means of a fiber amplified 1582 nm DFB laser,” *Sensors and Actuators B: Chemical*, vol. 221, pp. 666–672, 2015.
- [3] H. Yi, R. Maamary, X. Gao, M. W. Sigrist, E. Fertein, and W. Chen, “Short-lived species detection of nitrous acid by external-cavity quantum cascade laser based quartz-enhanced photoacoustic absorption spectroscopy,” *Applied Physics Letters*, vol. 106, no. 10, Article ID 101109, 2015.
- [4] A. Rosencwaig, *Photoacoustics and Photoacoustic Spectroscopy*, Wiley, 1980.
- [5] P. Patimisco, G. Scamarcio, F. K. Tittel, and V. Spagnolo, “Quartz-enhanced photoacoustic spectroscopy: a review,” *Sensors*, vol. 14, no. 4, pp. 6165–6206, 2014.
- [6] H. Wu, L. Dong, W. Ren et al., “Position effects of acoustic micro-resonator in quartz enhanced photoacoustic spectroscopy,” *Sensors and Actuators B: Chemical*, vol. 206, pp. 364–370, 2014.
- [7] H. Wu, A. Sampaolo, L. Dong et al., “Quartz enhanced photoacoustic  $\text{H}_2\text{S}$  gas sensor based on a fiber-amplifier source and a custom tuning fork with large prong spacing,” *Applied Physics Letters*, vol. 107, no. 11, Article ID 111104, 2015.
- [8] Y. Ma, G. Yu, J. Zhang, X. Yu, R. Sun, and F. K. Tittel, “Quartz enhanced photoacoustic spectroscopy based trace gas sensors using different quartz tuning forks,” *Sensors*, vol. 15, no. 4, pp. 7596–7604, 2015.
- [9] L. Dong, A. A. Kosterev, D. Thomazy, and F. K. Tittel, “QEPAS spectrophones: design, optimization, and performance,” *Applied Physics B: Lasers and Optics*, vol. 100, no. 3, pp. 627–635, 2010.
- [10] K. Liu, X. Guo, H. Yi, W. Chen, W. Zhang, and X. Gao, “Off-beam quartz-enhanced photoacoustic spectroscopy,” *Optics Letters*, vol. 34, no. 10, pp. 1594–1596, 2009.
- [11] Y. Ma, X. Yu, G. Yu et al., “Multi-quartz-enhanced photoacoustic spectroscopy,” *Applied Physics Letters*, vol. 107, no. 2, Article ID 021106, 2015.
- [12] H. Yi, W. Chen, X. Guo et al., “An acoustic model for microresonator in on-beam quartz-enhanced photoacoustic spectroscopy,” *Applied Physics B*, vol. 108, no. 2, pp. 361–367, 2012.
- [13] H. Zheng, L. Dong, X. Yin et al., “Ppb-level QEPAS  $\text{NO}_2$  sensor by use of electrical modulation cancellation method with a high power blue LED,” *Sensors and Actuators, B: Chemical*, vol. 208, pp. 173–179, 2015.
- [14] A. A. Kosterev, F. K. Tittel, D. V. Serebryakov, A. L. Malinovsky, and I. V. Morozov, “Applications of quartz tuning forks in spectroscopic gas sensing,” *Review of Scientific Instruments*, vol. 76, no. 4, Article ID 043105, 2005.
- [15] Y. Cao, W. Jin, H. L. Ho, L. Qi, and Y. H. Yang, “Acetylene detection based on diode laser QEPAS: combined wavelength and residual amplitude modulation,” *Applied Physics B*, vol. 109, no. 2, pp. 359–366, 2012.

## Research Article

# Analysis of ACAM Data for Trace Gas Retrievals during the 2011 DISCOVER-AQ Campaign

C. Liu,<sup>1</sup> X. Liu,<sup>1</sup> M. G. Kowalewski,<sup>2,3</sup> S. J. Janz,<sup>3</sup> G. González Abad,<sup>1</sup> K. E. Pickering,<sup>3</sup>  
K. Chance,<sup>1</sup> and L. N. Lamsal<sup>2,3</sup>

<sup>1</sup>Harvard-Smithsonian Center for Astrophysics, Cambridge, MA 02138, USA

<sup>2</sup>Goddard Earth Sciences Technology and Research, Universities Space Research Association, Columbia, MD 21044, USA

<sup>3</sup>NASA Goddard Space and Flight Center, Greenbelt, MD 20771, USA

Correspondence should be addressed to C. Liu; [chliu81@ustc.edu.cn](mailto:chliu81@ustc.edu.cn)

Received 15 June 2015; Accepted 30 July 2015

Academic Editor: Xiaoming Gao

Copyright © 2015 C. Liu et al. This is an open access article distributed under the Creative Commons Attribution License, which permits unrestricted use, distribution, and reproduction in any medium, provided the original work is properly cited.

To improve the trace gas retrieval from Airborne Compact Atmospheric Mapper (ACAM) during the DISCOVER-AQ campaigns, we characterize the signal to noise ratio (SNR) of the ACAM measurement. From the standard deviations of the fitting residuals, the SNRs of ACAM nadir measurements are estimated to vary from ~300 at 310 nm to ~1000 in the blue spectral region; the zenith data are noisier due to reduced levels of illumination and lower system throughput and also show many more pixels with abrupt anomalous values; therefore, a new method is developed to derive a solar irradiance reference at the top of the atmosphere (TOA) from average nadir measurements, at instrument spectral resolution and including instrument calibration characteristics. Using this reference can significantly reduce fitting residuals and improve the retrievals. This approach derives an absolute reference for direct fitting algorithms involving radiative transfer calculations and thus can be applied to both aircraft and ground-based measurements. The comparison of ACAM radiance with simulations using coincident ozonesonde and OMI data shows large wavelength-dependent biases in ACAM data, varying from ~-19% at 310nm to 5% at 360 nm. Correcting ACAM radiance in direct-fitting based ozone profile algorithm significantly improves the consistency with OMI total ozone.

## 1. Introduction

The Airborne Compact Atmospheric Mapper (ACAM) is an Ultraviolet (UV)/visible/near-infrared spectrometer covering the spectral range 304–910 nm [1]. It has been flown on board the NASA UC-12 aircraft in both nadir-viewing mode and much less frequently in zenith-sky mode during the DISCOVER-AQ campaigns as the primary airborne instrument to provide remote sensing column abundances of O<sub>3</sub>, NO<sub>2</sub>, and CH<sub>2</sub>O and explore column observations including profiles of partial O<sub>3</sub> columns [2].

To retrieve O<sub>3</sub> profiles or trace gas vertical column densities (VCDs) from ACAM data by directly fitting the radiance and using the optimal estimation inversion technique, it is critical to perform accurate radiometric calibration and characterize the signal to noise ratio (SNR) of the measurements as measurement constraint [3, 4]. Liu et al. [3]

performed empirical radiometric calibration of OMI data by comparing measured radiance with simulated radiance using zonal mean Microwave Limb Sounder (MLS) O<sub>3</sub> profiles in the stratosphere and climatological O<sub>3</sub> profiles in the troposphere. A similar method can be applied to ACAM measurements but using simultaneously observed O<sub>3</sub> sonde profiles during the DISCOVER-AQ campaigns. The SNR of ACAM measurements can be determined through examining the random part of the fitting residuals.

Because it is impossible to measure extraterrestrial solar irradiance spectrum with the same instrument for ground-based or aircraft UV/visible spectroscopic measurements, various methods have been used to obtain reference spectra for retrieving trace gas abundance from these measurements. The classical Langley extrapolation method derives the extraterrestrial solar irradiance by extrapolating measured irradiance to zero air mass to remove the effects of

the atmosphere [5–7]. It has been commonly used for Brewer and Dobson measurements to measure  $O_3$  and aerosol optical depth, but it has to be done at a very clean atmospheric site (e.g., Mauna Loa, Hawaii) under very special conditions (e.g., cloudless, with little atmospheric variation during the measurement period of a few hours in the morning or afternoon). Atmospheric variability and instrument instability can cause errors in top of the atmosphere (TOA) solar irradiance derived by this way. A more widely used method, especially for retrieving trace gases from UV/visible spectra, is to use zenith-sky or clean background measurements as references [8–16]. Retrievals performed using such reference spectra result in differential quantities between measured and reference spectra. Statistical approaches like minimum-amount Langley extrapolation (MLE) and the bootstrap-estimation methods or other correlative measurements are often used to derive the offset in the reference spectra [9, 17]. In addition, it is more complicated to use such reference spectra in direct fitting of radiance with radiative transfer calculations to derive absolute quantities from both nadir and zenith-sky measurements. Tzortziou et al. [18] convolved calibrated high-resolution solar irradiance reference [19] with instrument slit functions to derive the extraterrestrial solar irradiance spectrum from ground-based Pandora measurements for retrieving absolute total  $O_3$ . However, radiometric/wavelength calibration differences between high-resolution reference and measurements often cause large errors to minor trace gas determinations. In this paper, a novel technique is developed to derive TOA solar irradiance reference spectrum from aircraft nadir/zenith measurements.

The main purpose of this paper is to perform ACAM absolute radiometric calibration, characterize instrument measurement SNR, and derive proper TOA reference spectrum for improving trace gas retrievals from ACAM measurements during the 2011 Baltimore-Washington D.C. DISCOVER-AQ campaign. It is organized as follows. The ACAM instrument and data analysis are described in Section 2. Section 3 focuses on the wavelength and slit function calibration and characterization of ACAM SNR and identification of problematic spectral pixels. Section 4 presents a new method of deriving TOA solar irradiance reference spectrum. Section 5 concludes this study.

## 2. ACAM Instrument and Data Analysis

The Airborne Compact Atmospheric Mapper (ACAM) flown on board the NASA UC-12 aircraft was designed and built at the NASA Goddard Space Flight Center (GSFC). The science objectives of ACAM are to provide remote sensing observations of tropospheric and boundary layer pollutants to help understand some of the most important pollutants that directly affect the health of the population. The ACAM instrument includes two spectrographs, the air quality (AQ) spectrometer and the ocean color (OC) spectrograph. The first one, the UV/Visible AQ spectrometer, covers the 304 nm to 520 nm spectral region at a moderate resolution of 0.8 nm. It is optimized for the measurement of tropospheric pollutants and water vapor. The second one, the OC spectrograph,

covers the spectral region ranging from 460 nm to 900 nm with a resolution of 1.5 nm optimized for ocean color, water vapor, and aerosols. They operate in two viewing modes, nadir and zenith view, with a spatial resolution of  $\sim 1.5 \times 0.75 \text{ km}^2$  for nadir view. A detailed description of ACAM instrument can be found in [1].

The SAO basic optical absorption spectroscopy (BOAS) trace gas fitting algorithm is adapted to perform wavelength and slit function calibration and spectral fitting of trace gases [20] and has been described in detail in Liu et al. [21]. In this study, we use the derived broadened Gaussian slit function parameters from ACAM data [21] for preconvolution of trace gas cross sections. The fitting algorithm is quite sensitive to the input parameter settings such as retrieval fitting window, the order of polynomials which is used to remove the slow variation of observed spectrum, and the involved absorption of the other trace gases. In this study, through intensive investigations,  $O_3$ ,  $NO_2$ , and HCHO are optimized mainly by using new fitting window 318–335 nm, 430–485 nm, and 324–457 nm, respectively.

## 3. Instrument SNR Characterizations and Radiometric Calibration

The fitting residuals contain a systematic component as well as a random component. The standard deviation (i.e., random component) of mean fitting residuals can generally be used to characterize the SNR of the ACAM measurements. Figure 1 shows standard deviations of fitting residuals for three fitting windows derived from one day of ACAM nadir viewing and zenith-sky data on July 21, 2011. In general, they reflect the SNR of ACAM spectral pixels except for some anomalous pixels, especially in the zenith-sky measurements. The SNR of nadir measurements increases from  $\sim 300$  around 310 nm to  $\sim 700$  at 340 nm and 1000 in the blue spectral region. Note that ACAM measurements have 8 samples per FWHM, which effectively enhances the SNR by a factor of 1.63 compared to measurements with 3 samples per FWHM (e.g., OMI). The zenith data are noisier due to reduced levels of illumination and lower system throughput through the zenith fiber port. The anomalous pixels in zenith data are probably linked to instrument radiometric calibration problems and suggest that the current quality of zenith data is inadequate as a reference for retrieving trace gases from nadir measurements. We have identified these pixels with spikes in a previous version of the nadir data and reported them to the ACAM calibration team. They informed us that most of these pixels are affected by inadequate dark current correction. As shown in Figure 1, most of these spikes have been removed in the latest version of ACAM nadir data. They might be removed from zenith measurements in the future.

In order to investigate the quality of ACAM radiometric calibration and perform necessary corrections to ACAM radiance for direct fitting of radiance with radiative calculations, we compare ACAM radiance with simulated radiance using the vector linearized discrete ordinate radiative transfer model (VLIDORT) [22], similar to the comparison described in Liu et al. [3]. To improve the accuracy of the simulation,

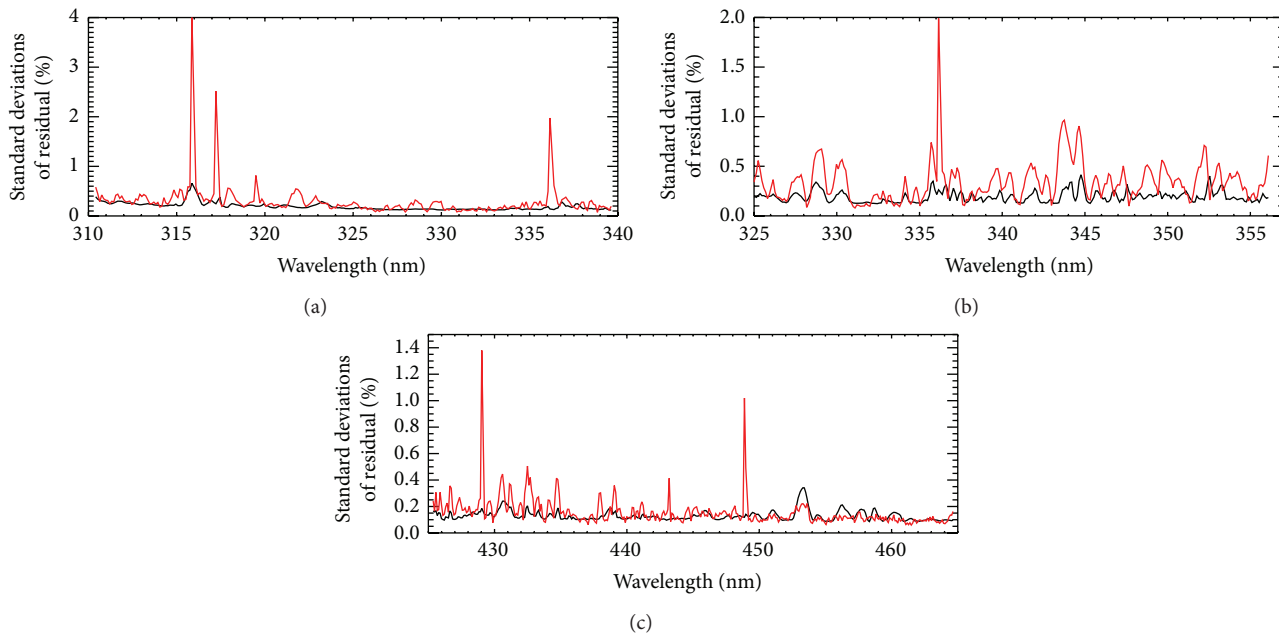


FIGURE 1: Standard deviations of fitting residuals from both zenith (red) and nadir (black) measurements of the ACAM AQ channel on July 21, 2011, for three selected wavelength ranges: (a)  $O_3$  fitting window, (b)  $CH_2O$  fitting window, and (c)  $NO_2$  fitting window.

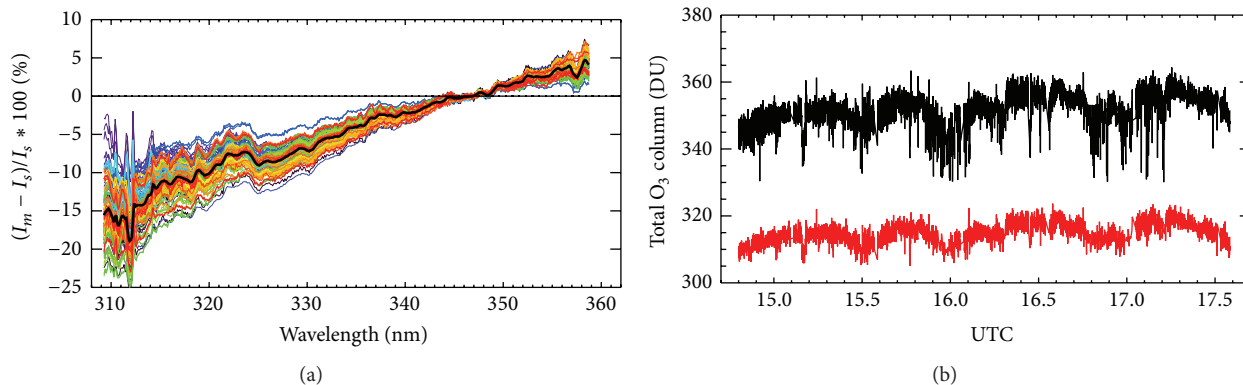


FIGURE 2: (a) Difference between ACAM ( $I_m$ ) and simulated ( $I_s$ ) radiance versus wavelength for 158 ozonesonde/ACAM collocations (within 2 hours and 1 km) in different colors, for the 2011 DISCOVER-AQ flight campaign. The average difference (black) is used as the empirical radiometric correction. (b) Retrieved total ozone column with (black) and without (red) using the derived empirical correction from ACAM radiance in the spectral region 318–335 nm from July 21, 2011, using the optimal estimation based ozone profile algorithm.

we use ozonesonde profiles measured at Beltsville (39.1°N, 76.9°W) and Edgewood (39.4°N, 76.3°W) during the 2011 DISCOVER-AQ flight campaign collocated with ACAM observations within 2 hours and 0.01° longitude and latitude below 100 hPa and scaled climatologically stratospheric ozone profiles from McPeters et al. [23] to match the daily overpass OMI  $O_3$  total ozone column (within 6 hours and 0.07° latitude and 1° longitude, 6 DU added to account for known systematic offset in the OMTO3 caused by the use of the Bass and Paur cross sections). A total of 158 collocations with 48 ozonesonde profiles are used in the simulations.

Figure 2(a) shows individual percentage differences between ACAM and simulated radiance in the spectral range 309–360 nm for all the collocations (in colors) and

the average difference (black). The average difference varies from  $\sim -19\%$  to  $\sim 5\%$  showing significant wavelength dependence. The difference is zero at 347.2 nm as we derive cloud information from this wavelength region by matching simulated and ACAM radiance. Thus, these are relative wavelength-dependent differences, which actually matter to the ozone profile algorithm [3]. There is significant variability in the derived differences ( $\sim 10\%$  at 310 nm and  $\sim 5\%$  at 360 nm) due to mismatch in time and location and uncertainties/errors in used ozone profiles. The presence of consistent overall features for these collocations indicates the existence of wavelength-dependent radiometric calibration errors in current ACAM data. The ACAM calibration team is currently revisiting ACAM's absolute radiometric calibration for

improvement, particularly in removing the stray light component which becomes increasingly important at wavelengths below 350 nm. To show the importance of applying this correction to the optimal estimation based ozone profile algorithm [3] modified for ACAM data, we apply an empirical correction to both ACAM radiance using the average difference and retrieve ozone profile from ACAM radiance in the spectral region 318–335 nm on July 21, 2011. Figure 2(b) compares the retrieved total ozone with and without applying this correction. After applying the correction, the total ozone is significantly reduced, by  $\sim 35$  DU, more consistent with the overpass OMI total ozone column of  $309 \pm 0.6$  DU, and appears to be less noisy.

#### 4. Derived TOA Solar Irradiance Reference

A new method is developed to derive the TOA solar irradiance reference spectrum over a spectral window from ACAM

$$I_{\text{TOA},n}(\lambda) = \frac{\left\{ \left[ \left( \overline{I}_n(\lambda) - P_b(\lambda) \right) / P_s(\lambda) - \sum_i a_{2,i} X_{2,i}(\lambda) \right] \exp \left( \sum_i n_i \sigma_i(\lambda) \right) - \sum_i a_{1,i} X_{1,i}(\lambda) \right\}}{A} \quad (1)$$

$A$  is the scaling parameter.  $X_{1,i}(\lambda)$ ,  $\sigma_i(\lambda)$ , and  $X_{2,i}(\lambda)$  are the basis functions in initial add-on, Beer's law, and second add-on modes, respectively, and  $a_{1,i}$ ,  $n_i$ , and  $a_{2,i}$  are the corresponding coefficients. The basis functions can include trace gas cross sections, Ring effect, undersampling spectra, and common residual spectra. Each basis function is typically included in only one of the modes (e.g., cross sections as  $\sigma_i$ , Ring effect (Chance and Spurr, 1997) as  $X_{1,i}$ , and common mode as  $X_{2,i}$ ).  $P_s(\lambda)$  and  $P_b(\lambda)$  are the scaling and baseline polynomials, respectively. An option to the above process is whether to apply  $n_i$  of the target trace gas. Applying  $n_i$  cancels the part in  $\overline{I}_n(\lambda)$ , leaving the artifact part in the  $I_{\text{TOA},n}(\lambda)$ . On the other hand, not applying  $n_i$  cancels the artifact part, leaving the part from  $\overline{I}_n(\lambda)$  in the  $I_{\text{TOA},n}(\lambda)$ .  $I_{\text{TOA},n}(\lambda)$  contains a systematic offset from the target gas in either case. To reduce the systematic offset, we apply  $n_i$  for  $\text{O}_3$  and do not apply  $n_i$  for other minor trace gases.

The derived  $I_{\text{TOA},n}(\lambda)$  is a solar irradiance reference at instrument spectral resolution that includes instrument calibration characteristics. When it is used as a reference in the trace gas retrievals, it cancels most of the systematic instrument calibration features, leading to improved relative root mean square (RMS) values of the fitting residuals as shown in the next paragraph. It can be derived from either nadir or zenith measurements but, due to much more frequent nadir measurements and their higher qualities (as shown in Figure 1), we derive TOA solar reference using the nadir measurements. This method can also be applied to ground-based measurements or satellite measurements if high quality solar irradiance measurements are not available. Although it contains some systematic offset, it can be used as an absolute reference spectrum for direct fitting algorithms

nadir measurements. First, we choose several hundred nadir measurements with similar radiance and have relatively small SCDs (through initial spectral fitting) of the target trace gas (i.e., for  $\text{NO}_2$  and  $\text{CH}_2\text{O}$ ) and derive an average nadir radiance spectrum  $\overline{I}_n(\lambda)$ . The averaging of nadir measurements at similar radiance significantly reduces random noise in the measurements. Second, we use the high-resolution solar reference spectrum  $I_{h0,\lambda}$  convolved with derived slit functions to fit  $\overline{I}_n(\lambda)$  over a fitting window larger than the target trace gas fitting window by  $\sim 2$  nm on both sides while simulating the radiance spectrum. The fitted trace gas SCDs come from two parts: (a) the actual trace gas in the atmosphere contained in  $\overline{I}_n(\lambda)$  and (b) the artifacts from the use of  $I_{h0,\lambda}$ , which introduces structures similar to some of the target trace gas. Typically, the former is much larger for  $\text{O}_3$ , but the latter is much larger for minor trace gases. Third, by replacing  $I_s(\lambda)$  with  $\overline{I}_n(\lambda)$  and applying all the fitted parameters in the reverse process, we can derive the TOA solar irradiance according to

involving radiative calculations (e.g., ozone profile retrieval algorithm) from both nadir and zenith measurements.

To show the retrieval improvement using our derived  $I_{\text{TOA},n}(\lambda)$ , we compare retrievals of  $\text{O}_3$ ,  $\text{CH}_2\text{O}$ , and  $\text{NO}_2$  SCDs using three references in Figure 3. The other two references for comparison are the average zenith-sky reference and the TOA solar irradiance reference  $I_{\text{TOA}}(\lambda)$  by directly convolving the high-resolution solar irradiance spectrum with ACAM slit functions using (1).  $I_{\text{TOA}}(\lambda)$  is very similar to our derived  $I_{\text{TOA},n}(\lambda)$  except that it does not contain ACAM calibration features. Using  $I_{\text{TOA},n}(\lambda)$  significantly reduces fitting RMS values and fitting uncertainties especially for  $\text{CH}_2\text{O}$  and  $\text{NO}_2$  by more than a factor of 3 and 4. The average zenith reference gives better precision for  $\text{CH}_2\text{O}$  fitting, comparable fitting precision and better RMS uncertainties for  $\text{NO}_2$  fitting, and worse precision for  $\text{O}_3$ , compared to the  $I_{\text{TOA}}(\lambda)$ . Although the zenith reference is also measured by the ACAM instrument, the large fitting RMS is likely due to the optical path difference of zenith port from the nadir port, by using additional optical fibers, systematic calibration differences between zenith and nadir data, and poorer SNR in the zenith data. Both TOA solar irradiance references are absolute references, giving actual SCDs in the atmosphere, while the average zenith reference is a relative reference, giving very small or even negative  $\text{O}_3$  SCDs especially when the solar zenith angle is small. However, for  $\text{CH}_2\text{O}$  and  $\text{NO}_2$  fitting, using  $I_{\text{TOA}}(\lambda)$  leads to large systematic offsets,  $\sim 2 \times 10^{17}$  and  $\sim 10^{16}$  molecules  $\text{cm}^{-2}$  for  $\text{CH}_2\text{O}$  and  $\text{NO}_2$ , respectively, mainly due to artifacts from the convolved solar irradiance. Compared to  $I_{\text{TOA},n}(\lambda)$ , the zenith reference gives similar  $\text{NO}_2$  SCDs but larger  $\text{CH}_2\text{O}$  SCDs by  $\sim 4 \times 10^{16}$  molecules  $\text{cm}^{-2}$ .

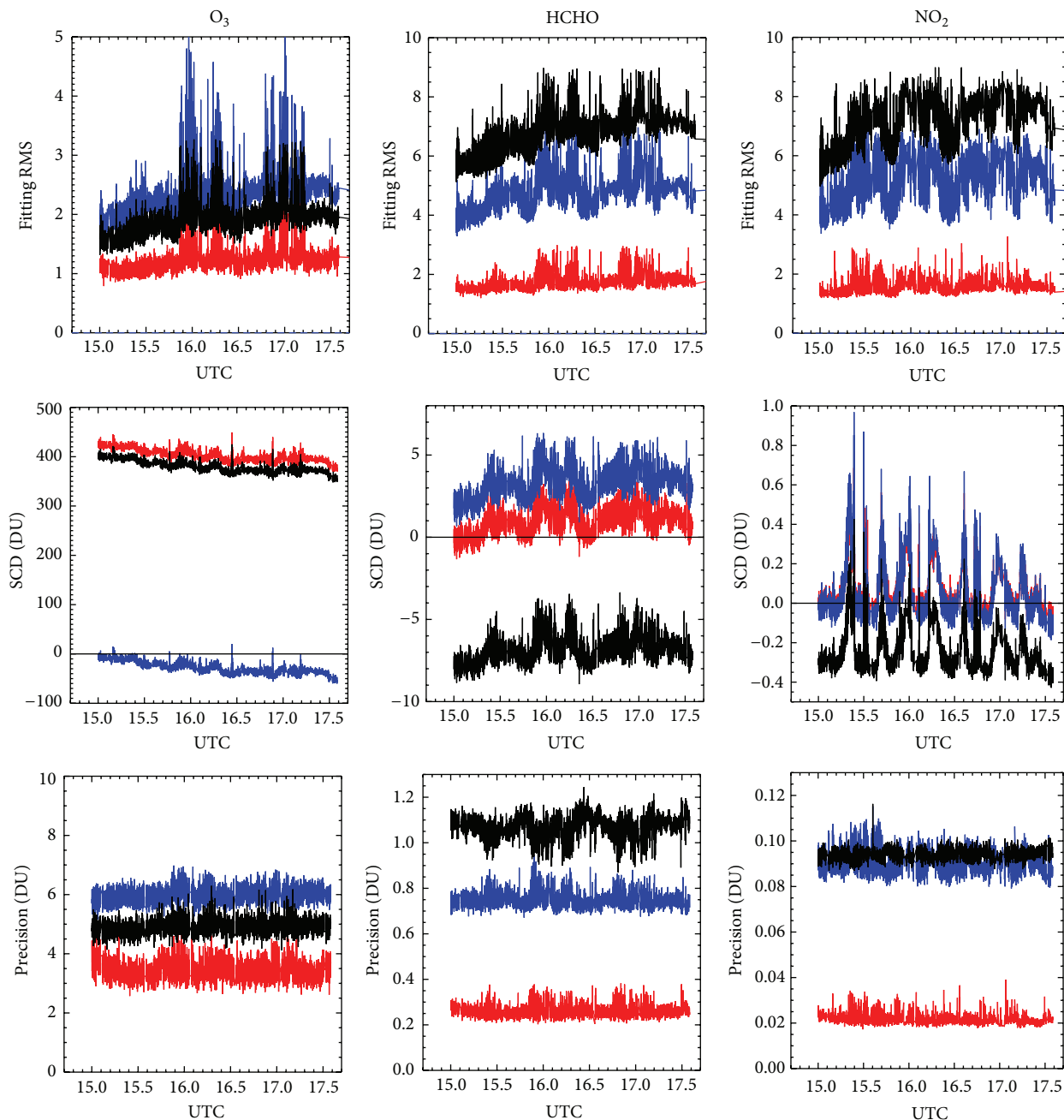


FIGURE 3: Comparison of  $O_3$  (left),  $CH_2O$  (middle column), and  $NO_2$  (right) fitting in (top) relative RMS, (middle row) SCDs, and (bottom) precision of SCDs for ACAM measurements from July 21, 2011, using three different reference spectra: average zenith reference (blue), high-resolution solar irradiance convolved with instrument slit functions (black), and derived TOA solar irradiance from average nadir radiance spectrum (red).

## 5. Summaries

In this study we estimate the SNRs and identify anomalous spectral pixels in the data from standard deviations of the fitting residuals. The SNRs for ACAM nadir measurements increase from  $\sim 300$  around 310 nm to  $\sim 700$  at 340 nm and 1000 in the blue spectral region. The zenith data are noisier and show many more anomalous pixels, indicating dark current calibration problems. This also suggests that the current

quality of zenith spectra is insufficient as reference spectra for trace gas retrievals. Using collocated ozonesonde measurements in the troposphere and climatological  $O_3$  in the stratosphere scaled to match overpass OMI total ozone column, we simulated radiance and compared them with ACAM radiance in the UV ( $\sim 309$ – $360$  nm). The average differences show strong wavelength dependence, varying from  $\sim -19\%$  at 310 nm to 5% at 360 nm, indicating the presence of large wavelength-dependent radiometric calibration errors in the

current ACAM data. Using the average difference as the correction to ACAM radiance, we evaluated the impact of this correction on the retrieved total ozone using the optimal estimation based ozone profile algorithm. The correction reduces the total ozone by  $\sim 35$  DU, making it more consistent with the coincident OMI total ozone.

We developed a new method to derive the TOA solar irradiance reference at instrument spectral resolution, including instrument calibration characteristics, from aircraft nadir measurements through reversing the calibration process. We compared the performance of retrieving  $O_3$ ,  $CH_2O$ , and  $NO_2$  SCDs using this derived TOA reference with those using an average zenith reference and a TOA reference by directly convolving high-resolution solar irradiance with derived instrument slit functions. Using our derived TOA reference significantly reduces fitting RMS/uncertainty (by a factor of 3 and 4 for  $CH_2O$  and  $NO_2$ ). It gives absolute  $O_3$  SCDs compared to the zenith reference and significantly reduces the artificial offsets in  $CH_2O$  and  $NO_2$  SCDs compared to the directly convolved TOA reference. This method can be applied to both aircraft and ground-based measurements to derive retrieval reference spectra, which can serve as absolute reference for direct fitting algorithms involving radiative calculations, although it still causes systematic offsets in the derived quantities as do most of the conventional reference spectra for aircraft/ground-based measurements.

## Disclosure

The current address for C. Liu is University of Science and Technology of China, Hefei, Anhui, China.

## Conflict of Interests

The authors declare that there is no conflict of interests regarding the publication of this paper.

## Acknowledgments

Funding for this work at SAO is provided by NASA Grants NNX11AH77G and NNX12AJ66G as part of the NASA Earth Venture-1 DISCOVER-AQ project and by the Smithsonian Institution. The authors thank Anne Thompson (NASA/GSFC) and Everette Joseph (Howard University) who provided the ozonesonde data from the Edgewood and Beltsville sites, respectively. They acknowledge James Crawford for his strong support on this work.

## References

- [1] M. G. Kowalewski and S. J. Janz, "Remote sensing capabilities of the airborne compact atmospheric mapper," in *Earth Observing Systems XIV*, vol. 7452 of *Proceedings of SPIE*, San Diego, Calif, USA, August 2009.
- [2] X. Liu, K. Chance, C. E. Sioris et al., "Ozone profile and tropospheric ozone retrievals from global ozone monitoring experiment: algorithm description and validation," *Journal of Geophysical Research*, vol. 110, Article ID D20307, 2005.
- [3] X. Liu, P. K. Bhartia, K. Chance, R. J. D. Spurr, and T. P. Kurosu, "Ozone profile retrievals from the ozone monitoring instrument," *Atmospheric Chemistry and Physics*, vol. 10, no. 5, pp. 2521–2537, 2010.
- [4] C. R. Nowlan, X. Liu, K. Chance et al., "Retrievals of sulfur dioxide from the global ozone monitoring experiment 2 (GOME-2) using an optimal estimation approach: algorithm and initial validation," *Journal of Geophysical Research: Atmospheres*, vol. 116, no. 18, 2011.
- [5] J. Gröbner and J. B. Kerr, "Ground-based determination of the spectral ultraviolet extraterrestrial solar irradiance: providing a link between space-based and ground-based solar UV measurements," *Journal of Geophysical Research: Atmospheres*, vol. 106, no. 7, Article ID 2000JD900756, pp. 7211–7217, 2001.
- [6] A. F. Bais, "Absolute spectral measurements of direct solar ultraviolet irradiance with a Brewer spectrophotometer," *Applied Optics*, vol. 36, no. 21, pp. 5199–5204, 1997.
- [7] A. Cheymol, H. De Backer, W. Josefsson, and R. Stübi, "Comparison and validation of the aerosol optical depth obtained with the Langley plot method in the UV-B from Brewer Ozone Spectrophotometer measurements," *Journal of Geophysical Research: Atmospheres*, vol. 111, no. 16, Article ID D16202, 2006.
- [8] K.-P. Heue, A. Richter, M. Bruns et al., "Validation of SCIAMACHY tropospheric  $NO_2$ -columns with MAXDOAS measurements," *Atmospheric Chemistry and Physics*, vol. 5, no. 4, pp. 1039–1051, 2005.
- [9] J. Herman, A. Cede, E. Spinei, G. Mount, M. Tzortziou, and N. Abuhassan, " $NO_2$  column amounts from ground-based Pandora and MFDOAS spectrometers using the direct-sun DOAS technique: intercomparisons and application to OMI validation," *Journal of Geophysical Research: Atmospheres*, vol. 114, no. 13, Article ID D13307, 2009.
- [10] H. K. Roscoe, M. Van Roozendaal, C. Fayt, and et al., "Intercomparison of slant column measurements of  $NO_2$  and  $O_4$  by MAX-DOAS and zenith-sky UV and visible spectrometers," *Atmospheric Measurement Techniques*, vol. 3, no. 6, pp. 1629–1646, 2010.
- [11] R. Sinreich, S. Coburn, B. Dix, and R. Volkamer, "Ship-based detection of glyoxal over the remote tropical Pacific Ocean," *Atmospheric Chemistry and Physics*, vol. 10, no. 23, pp. 11359–11371, 2010.
- [12] H. Irie, H. Takashima, Y. Kanaya et al., "Eight-component retrievals from ground-based MAX-DOAS observations," *Atmospheric Measurement Techniques*, vol. 4, no. 6, pp. 1027–1044, 2011.
- [13] T. Vlemmix, A. J. M. Pijters, A. J. C. Berkhout, L. F. L. Gast, P. Wang, and P. F. Levelt, "Ability of the MAX-DOAS method to derive profile information for  $NO_2$ : can the boundary layer and free troposphere be separated?" *Atmospheric Measurement Techniques*, vol. 4, no. 12, pp. 2659–2684, 2011.
- [14] C. Popp, D. Brunner, A. Damm, M. Van Roozendaal, C. Fayt, and B. Buchmann, "High-resolution  $NO_2$  remote sensing from the Airborne Prism Experiment (APEX) imaging spectrometer," *Atmospheric Measurement Techniques*, vol. 5, no. 9, pp. 2211–2225, 2012.
- [15] A. Merlaud, M. van Roozendaal, J. van Gent et al., "DOAS measurements of  $NO_2$  from an ultralight aircraft during the Earth Challenge expedition," *Atmospheric Measurement Techniques*, vol. 5, no. 8, pp. 2057–2068, 2012.
- [16] G. Pinardi, M. Van Roozendaal, N. Abuhassan et al., "MAX-DOAS formaldehyde slant column measurements during

- CINDI: intercomparison and analysis improvement,” *Atmospheric Measurement Techniques*, vol. 6, pp. 167–185, 2013.
- [17] A. Cede, J. Herman, A. Richter, N. Krotkov, and J. Burrows, “Measurements of nitrogen dioxide total column amounts using a Brewer double spectrophotometer in direct Sun mode,” *Journal of Geophysical Research*, vol. 111, p. 5304, 2006.
- [18] M. Tzortziou, J. R. Herman, A. Cede, and N. Abuhassan, “High precision, absolute total column ozone measurements from the Pandora spectrometer system: comparisons with data from a Brewer double monochromator and Aura OMI,” *Journal of Geophysical Research: Atmospheres*, vol. 117, no. 16, Article ID 16303, 2012.
- [19] K. Chance and R. L. Kurucz, “An improved high-resolution solar reference spectrum for earth’s atmosphere measurements in the ultraviolet, visible, and near infrared,” *Journal of Quantitative Spectroscopy and Radiative Transfer*, vol. 111, no. 9, pp. 1289–1295, 2010.
- [20] K. Chance, “Analysis of BrO measurements from the Global Ozone Monitoring Experiment,” *Geophysical Research Letters*, vol. 25, no. 17, pp. 3335–3338, 1998.
- [21] C. Liu, X. M. G. Liu, S. J. Kowalewski et al., “Characterization and verification of ACAM slit functions for trace gas retrievals during the 2011 DISCOVER-AQ flight campaign,” *Atmospheric Measurement Techniques*, vol. 8, pp. 751–759, 2015.
- [22] R. J. D. Spurr, “VLIDORT: a linearized pseudo-spherical vector discrete ordinate radiative transfer code for forward model and retrieval studies in multilayer multiple scattering media,” *Journal of Quantitative Spectroscopy and Radiative Transfer*, vol. 102, no. 2, pp. 316–342, 2006.
- [23] R. D. McPeters, G. J. Labow, and J. A. Logan, “Ozone climatological profiles for satellite retrieval algorithms,” *Journal of Geophysical Research*, vol. 112, no. 5, Article ID D05308, 2007.

## Research Article

# Retrieval of Atmospheric CO<sub>2</sub> and CH<sub>4</sub> Variations Using Ground-Based High Resolution Fourier Transform Infrared Spectra

Tian Yuan,<sup>1</sup> Liu Cheng,<sup>1,2</sup> Sun You Wen,<sup>1</sup> Xie Pin Hua,<sup>1,2</sup> Wang Wei,<sup>1</sup>  
Liu Wen Qing,<sup>1,2</sup> Liu Jian Guo,<sup>1,2</sup> Li Ang,<sup>1</sup> Hu Ren Zhi,<sup>1</sup> and Zeng Yi<sup>1</sup>

<sup>1</sup>Key Lab of Environmental Optics & Technology, Anhui Institute of Optics and Fine Mechanics,  
Chinese Academy of Sciences, Hefei 230031, China

<sup>2</sup>University of Science and Technology of China, Hefei 230026, China

Correspondence should be addressed to Liu Cheng; liucheng@hfcas.ac.cn

Received 23 June 2015; Accepted 31 August 2015

Academic Editor: Arnaud Cuisset

Copyright © 2015 Tian Yuan et al. This is an open access article distributed under the Creative Commons Attribution License, which permits unrestricted use, distribution, and reproduction in any medium, provided the original work is properly cited.

High resolution Fourier transform near IR solar spectra are used to estimate the column-averaged dry-air mole fraction (DMF) of CO<sub>2</sub> and CH<sub>4</sub> variations in the atmosphere. The preliminary retrieval results for CO<sub>2</sub> and CH<sub>4</sub> variations in the area of Hefei, China, are presented, and the underlying error sources are also analyzed. Both a forward analysis and an inversion algorithm are included in the retrieval. The forward analysis uses the modeled atmospheric transmittance to line-by-line (LBL) convolute the instrument line shape function. The influences of the temperature, pressure, humidity, and a priori gases are considered in the atmospheric transmittance model. The inversion algorithm is based on the nonlinear iterative and nonlinear least squares spectral fitting, which is used to obtain VCD<sub>CO<sub>2</sub></sub> and VCD<sub>CH<sub>4</sub></sub> (which represent vertical column density of CO<sub>2</sub> and CH<sub>4</sub>, resp.). Furthermore, the VCD<sub>O<sub>2</sub></sub> is also retrieved for converting the VCDs into DMFs. DMFs are final products of data analysis. The inversion results can clearly resolve the tiny variations of CO<sub>2</sub> and CH<sub>4</sub> under strong atmospheric background. Spectral fitting residuals for both VCD<sub>CO<sub>2</sub></sub> and VCD<sub>CH<sub>4</sub></sub> are less than 0.5%. Finally, CO<sub>2</sub> and CH<sub>4</sub> diurnal variations are investigated based on a typical observation. About 2 ppm amplitude for DMF<sub>CO<sub>2</sub></sub> diurnal variations and less than 15 ppb amplitude for DMF<sub>CH<sub>4</sub></sub> are observed.

## 1. Introduction

Greenhouse effect caused by greenhouse gases (GHGs) can produce a series of environmental and economic problems. Recording GHG variations with high precision and accuracy is of great significance for predicting future climate change. Besides, good knowledge of global source and sink of carbon is the prerequisite for global warming control because carbon (except vapor) is the most important component in the GHGs [1].

CO<sub>2</sub> and CH<sub>4</sub> are two important GHGs and carbon compounds, which have been the research hotspots for decades [1, 2]. To have good knowledge of these two gases, the world has established more than 100 in situ observation sites over the past 30 years [3, 4]. A large number of GHG researches have been accomplished based on the combination

of the in situ observation and global transmission model. In situ observations are mainly focused on the atmospheric boundary layer. The most striking characteristic of in situ observations on the atmospheric boundary layer is its high accuracy. But it is severely affected by the local source and sink and limited in the spatial coverage range [5]. Column density measurements can fill these gaps and are less influenced by the atmospheric boundary layer height changes and vertical transport [6]. Compared to in situ observation, column density measurements are less affected by temporal and spatial variations and thus make the horizontal gradients of the results more directly related to the underlying regional-scale fluxes [5]. The typical high precision tools for column measurements are satellite-based and ground-based Fourier transform spectrometer [7]. Currently, satellite-based Fourier transform spectrometer includes GOSAT (Japan), launched



FIGURE 1: Experimental instrument system.

in 2009, and the OCO-2 (United States), launched in 2014. To validate these satellite data, ground-based atmospheric GHGs observation network is established, called the Total Carbon Column Observation Network (TCCON) [5]. However, there is still no TCCON site locating in the area of China. That means it is unable to validate the satellite-based measurements in the whole area of China.

This paper aims to first retrieve  $\text{CO}_2$  and  $\text{CH}_4$  variations in China using ground-based high resolution Fourier transform infrared spectra. This study can not only provide an evidence for resolving the local source and sink of carbon circle but also facilitate the satellite-based GHG measurements validation.

## 2. Instrument Descriptions

The observation laboratory is installed on an island located in the west of Hefei (the capital of Anhui Province) in central and eastern China. It is adjacent to a lake with a longitude of  $117^{\circ}10'E$ , latitude of  $31^{\circ}54'N$ , and altitude of 30 m. The system consists of a high resolution ground-based Fourier transform infrared spectrometer (IFS125HR) and a solar tracker (Tracker-A Solar 547), both of which are purchased from Bruker Company. IFS125HR has 9 scanner compartments, with a maximum resolution of  $0.00096\text{ cm}^{-1}$ , and covers a spectral range of  $5\sim 50,000\text{ cm}^{-1}$ . The solar tracker is mounted inside a dome controlled by a motor on the building roof (as shown in pictures on the right of Figure 1). A tracking precision of  $\pm 0.1^{\circ}$  can be achieved by using the Camtracker mode (a built-in camera continuously adjusts the distance

between the sun spot and the field spot). Solar tracker directs the sun light through the roof aperture (as shown in pictures on the left of Figure 1) into the spectrometer. For  $\text{CO}_2$  and  $\text{CH}_4$  observation, the spectral resolution is set to  $0.02\text{ cm}^{-1}$  and the  $\text{CaF}_2$  beam splitter is used [8]. We choose InSb as the detector which covers  $3900\sim 15500\text{ cm}^{-1}$  spectral range and cooled with liquid nitrogen during operation. In order to avoid detector saturation, we select a minimum entrance aperture (0.5 mm) and insert an attenuator (grid metal) in front of the detector.

## 3. Spectra Retrieval

Spectra retrieval includes two steps, that is, VCDs retrieval and then DMFs retrieval. We use the GFIT algorithm to retrieve the  $\text{CO}_2$  and  $\text{CH}_4$  VCDs. GFIT is developed by JPL (Jet Propulsion Laboratory), California Institute of Technology [5, 9]. It combines nonlinear iteration and nonlinear least squares fitting. It is a standard inversion algorithm for TCCON network. When fitting a spectral range, GFIT attempts to minimize the quantity  $\chi^2$  with respect to the variables  $\alpha$ ,  $\beta$ ,  $\delta$ ,  $x_1$ ,  $x_2$ , and  $x_3$  and other parameters:

$$\chi^2 = \sum_{i=1}^{NM} \frac{(Y_i^M - Y^C(\alpha, \beta, V_i + \delta, x_1, x_2, x_3 \dots))^2}{\delta_i^2}, \quad (1)$$

where  $Y^M$  represents the measured spectra,  $Y^C$  represents the calculated spectra,  $\alpha$  is termed the continuum level,  $\beta$  is termed the continuum tilt,  $\delta$  is the frequency shift, and the

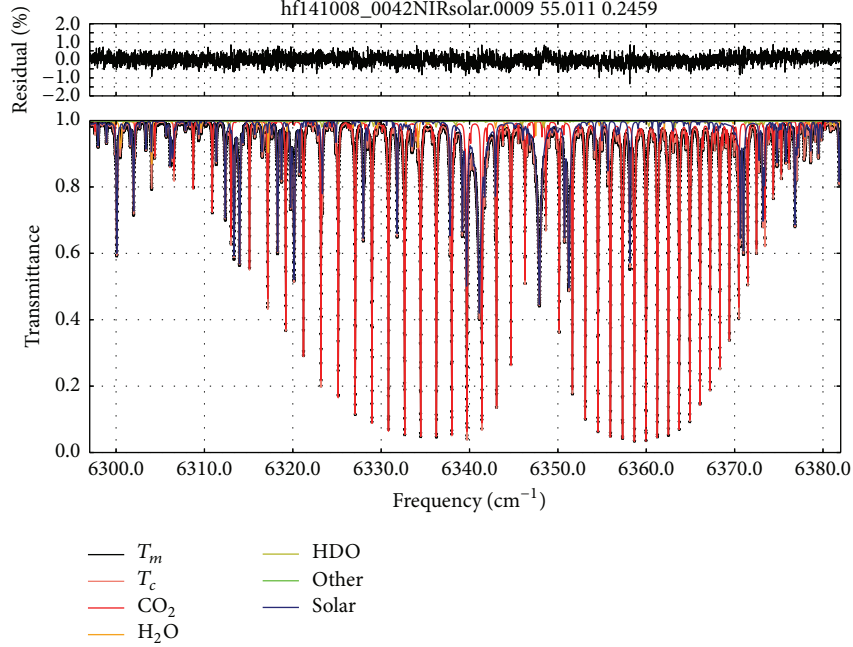


FIGURE 2: CO<sub>2</sub> spectral fitting within 6339 cm<sup>-1</sup> window: the spectrum was recorded on October 8, 2014, 0:47 (UTC). Black lines are the measurements, orange lines are the fitted transmittance, and contributions from individual gases are shown in color. Fitting residuals ( $T_m - T_c$ ) for CO<sub>2</sub> are 0.2459%.

various  $x$  terms are the scale factors for the different gases and  $\sigma_i$  is the uncertainty in the value of the  $i$ th element of  $Y^M$ .  $\alpha$ ,  $\beta$ ,  $\delta$ ,  $x_1$ ,  $x_2$ ,  $x_3$ ,  $\dots$ , and so forth are important outputs of GFIT. Due to the complexity of modeling the measured spectra  $Y^M$ , a forward model  $Y^C$  is exploited. It is expressed as

$$Y^M = Y^C + \varepsilon, \quad (2)$$

where  $\varepsilon$  is the measurement error.

Forward model  $Y^C$  is commonly termed the convolution of atmospheric transmittance and the instrument line shape function [10, 11]:

$$y_i^c = \left\{ [C + S(\nu_i - \nu_0)] y_{i_{\text{top}}} \text{ILS}(\nu_i, \delta) \otimes T(\nu_i) \right\} + z_{\text{offset}}, \quad (3)$$

$$T(\nu_i) = e^{-\sum_{j=0}^{70} \sum_k \sum_l \{ [c_k w_{0k,j}] [R_{l,k,j} F_{l,k,j}(\nu_i - \nu_{k,j})] n_j s_j \}}, \quad (4)$$

where  $y_i^c$  is the  $i$ th element of  $Y^C$ ,  $y_{i_{\text{top}}}$  is the atmosphere top layer spectra,  $C$  is continuum level,  $S$  is continuum tilt,  $\delta$  is frequency drift, and  $T(\nu_i)$  represents atmospheric transmittance. When modeling measured spectra, a discrete, line-by-line, multilayer, and multispecies expression for the atmospheric transmittance is applied as expressed by (4) [5].  $\nu_0$  is the center frequency of a spectral window,  $\text{ILS}(\nu_i, \delta)$  is instrument line shape function, and  $z_{\text{offset}}$  is spectral zero level offset. And the ILS used in GFIT is a nominal ideal ILS that is a numerical convolution of the sinc function with a rectangular function when the instrument is well aligned. The effect of the thermal radiation is ignored due to its negligible influence on the near-infrared spectrum.

Solar intensity relative fluctuation threshold is set to 5% for removing the interference of clouds and aerosols.

**3.1. Model Parameters Determination.** In order to achieve high precision retrieval, longitude, latitude, altitude, a priori profiles, real-time surface temperature, humidity, pressure, wind speed, wind direction, and other meteorological parameters need to be considered in the process of the forward model calculation [12]. In addition, the high resolution spectrometer IFS125HR should be calibrated by a low pressure HCl cell regularly because instrument alignment has great influence on the inversion results [10]. For the current version of spectra, we did not save the real-time surface temperature, humidity, and pressure parameters, and no HCl cell is available. Thus, in this study, we have to make some assumptions in the model calculation.

(1) Inside the laboratory, the air conditioning is set to a constant value of 24°, the dehumidifier is set to a constant value of 60%, and the IFS125HR is evacuated while saving the solar spectra. So we assume that the temperature inside the instrument ( $T_{\text{inside}}$ ) is a constant value of 24°, the internal pressure ( $P_{\text{inside}}$ ) is a constant value of 1 mbar, the internal relative humidity ( $H_{\text{inside}}$ ) is a constant value of 60%, the temperature outside the instrument ( $T_{\text{outside}}$ ) is a constant value of 24°, the external pressure ( $P_{\text{outside}}$ ) is a constant value of 1 standard atmospheric pressure (1024 pa), and the external relative humidity ( $H_{\text{outside}}$ ) is a constant value of 60%. In addition, a priori profiles for temperature, pressure, and humidity above observation station are based on NCEP (National Center for Environmental Prediction) data [13]. A priori profiles for all gases use the American standard

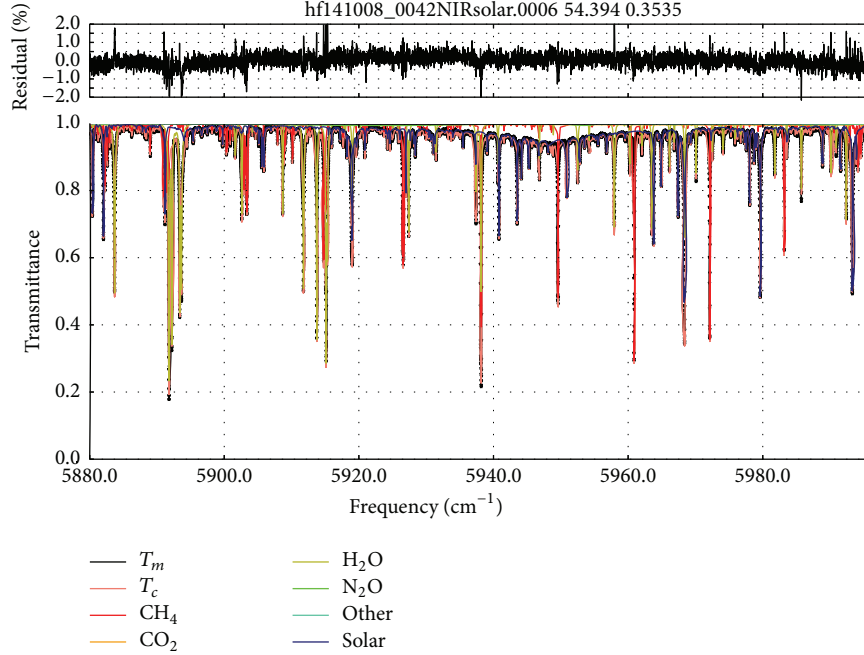


FIGURE 3:  $\text{CH}_4$  spectral fitting within  $5938 \text{ cm}^{-1}$  window: the spectrum was recorded on October 8, 2014, 0:47 (UTC). Black lines are the measurements, orange lines are the fitted transmittance, and contributions from individual gases are shown in color. Fitting residuals ( $T_m - T_c$ ) for  $\text{CH}_4$  are 0.3535%.

atmospheric parameters for the mid-latitude of northern hemisphere.

(2) We already aligned the IFS125HR just before we started to save the spectra, so we assume that the alignment of instrument is well because of the excellent stability of the instrument; that is, the influence of the instrument drift is neglected for all the spectra.

(3) Time correction is done every day before observations, so the saved spectra are consistent with the UTC (Universal Time Coordinated) within  $\pm 1$ -second precision.

**3.2. VCD Retrieval.** We use the GFIT algorithm to calculate the  $\text{CO}_2$  and  $\text{CH}_4$  VCDs which finds the best fitting between the calculated spectra and the measured spectra [14]. The most important outputs of the GFIT algorithm are scaling factors and their uncertainties as mentioned in (1). A priori profile mole fraction of a gas is multiplied by the scaling factor to yield the retrieved vertical column density [13]

$$\text{column}_{\text{gas}} = \text{SF}_{\text{gas}} \int_{z_s}^{\infty} f_{\text{gas}}^{\text{apriori}} n dz, \quad (5)$$

where  $\text{SF}_{\text{gas}}$  is the scaling factor for a gas,  $f_{\text{gas}}^{\text{apriori}}$  is the a priori profile of the gas,  $n$  is the total molecules number,  $z$  represents altitude, and  $z_s$  is the altitude of the first mirror of the solar tracker.

**3.3. DMF Calculation.** Gas column average dry-air mole fraction (DMF) is defined as

$$X_{\text{gas}} = \frac{\text{column}_{\text{gas}}}{\text{total dry column}}. \quad (6)$$

Because  $\text{VCD}_{\text{O}_2}$  in the atmosphere is well known, the total dry-air column can be obtained by using the relationship between  $\text{VCD}_{\text{O}_2}$  and the total dry-air column [15]:

$$\text{total dry column} = \frac{\text{column}_{\text{O}_2}}{0.2095}. \quad (7)$$

Substituting (7) into (6) yields the DMF:

$$X_{\text{gas}} = 0.2095 \frac{\text{column}_{\text{gas}}}{\text{column}_{\text{O}_2}}. \quad (8)$$

The advantages of DMF compared with VCD are as follows: (1) reducing the influence of surface pressure changes and water vapor interference on the inversion results; (2) reducing the systematic error sources which affect both the target gas and  $\text{O}_2$ ; (3) improving the inversion precision by minimizing the common scatter [15].

## 4. Data Analysis and Discussion

In this study, the direct solar spectra collected between October 6, 2014, and December 1, 2014, are retrieved. All the spectra which are saturated or the signal to noise ratios (SNR) which are less than 500 or the relative intensity variations which are larger than 5% (mainly caused by clouds and/or aerosols) are removed.  $\text{CO}_2$ ,  $\text{CH}_4$ , and  $\text{O}_2$  gases are retrieved simultaneously. Retrieval window parameters for  $\text{CO}_2$ ,  $\text{CH}_4$ , and  $\text{O}_2$  are listed in Table 1. The two central frequencies for  $\text{CO}_2$  windows are  $6220.00 \text{ cm}^{-1}$  and  $6339.50 \text{ cm}^{-1}$ , respectively. The final  $\text{VCD}_{\text{CO}_2}$  is the average of the windows' results. The same treatment is also applied to  $\text{CH}_4$ . The target gases

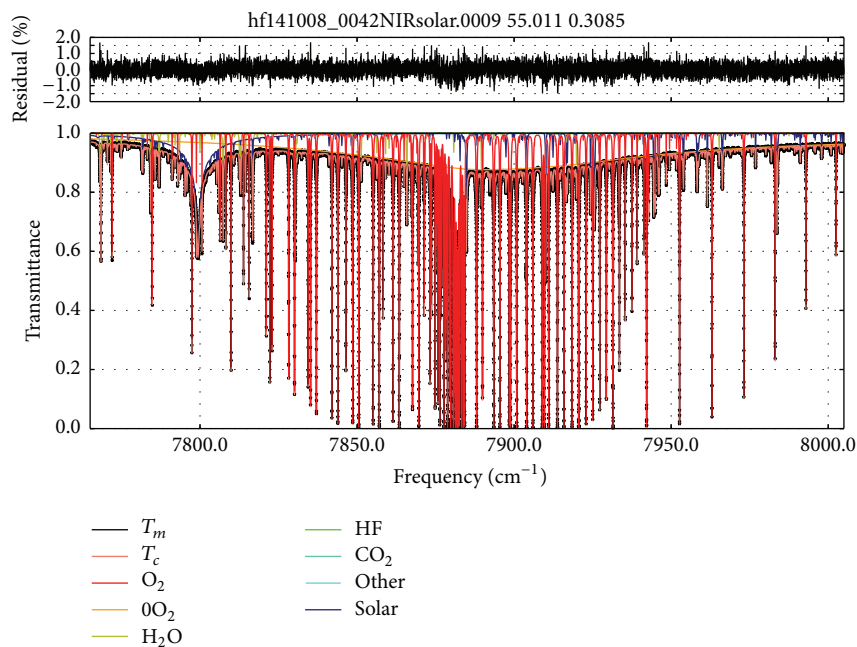


FIGURE 4:  $O_2$  spectral fitting within  $7885\text{ cm}^{-1}$  window: the spectrum was recorded on October 8, 2014, 0:47 (UTC). Black lines are the measurements, orange lines are the fitted transmittance, and contributions from individual gases are shown in color. Fitting residuals ( $T_m - T_c$ ) for  $O_2$  are 0.3085%.

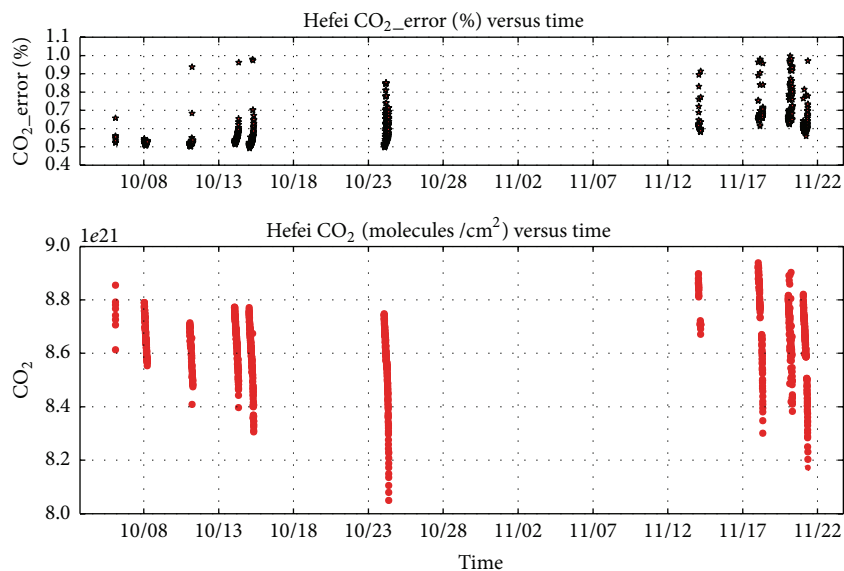


FIGURE 5:  $VCD_{CO_2}$  time series ranging from October 6, 2014, to December 1, 2014, which are the average of the retrieval values in  $6220\text{ cm}^{-1}$  and  $6339\text{ cm}^{-1}$  windows.

of interest (bold font) and interfering gases are also shown in Table 1. We set a fitting residual of  $<1\%$  to filter out those spectra which do not fulfill the assumptions in Section 3.1.

Figures 2, 3, and 4 are fitting examples for  $CO_2$ ,  $CH_4$ , and  $O_2$ , respectively, which are from a spectrum measured at  $26.535^\circ$  SZA (solar zenith angle) on October 8, 2014.  $T_c$  and  $T_m$  represent calculated spectrum and measured spectrum, respectively. Fitting residuals ( $T_m - T_c$ ) for  $CO_2$ ,  $CH_4$ , and  $O_2$

are 0.2459%, 0.3535%, and 0.3085%, respectively. The fitting residuals are mainly attributed to the unknown structure of spectroscopies and systematic errors, for example, electronic noise, acquisition noise, spectral structure noise, and scanning mirror fluctuation noise.

The time series of retrieved  $VCD_{CO_2}$  and  $VCD_{CH_4}$  are shown in Figures 5 and 6, respectively. Time periods ranging from October 6, 2014, to December 1, 2014, are presented for

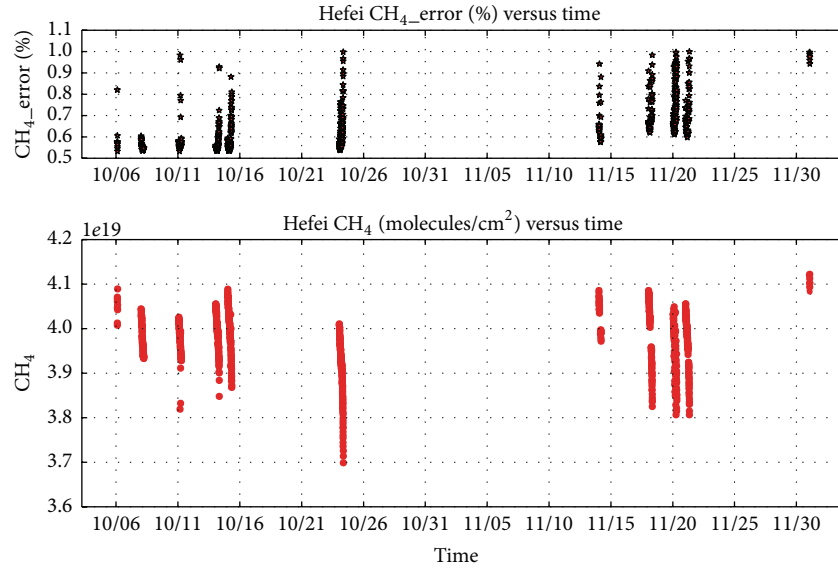


FIGURE 6:  $\text{VCD}_{\text{CH}_4}$  time series ranging from October 6, 2014, to December 1, 2014, which are the average of the retrieval values in  $5938\text{ cm}^{-1}$ ,  $6002\text{ cm}^{-1}$ , and  $6076\text{ cm}^{-1}$  windows.

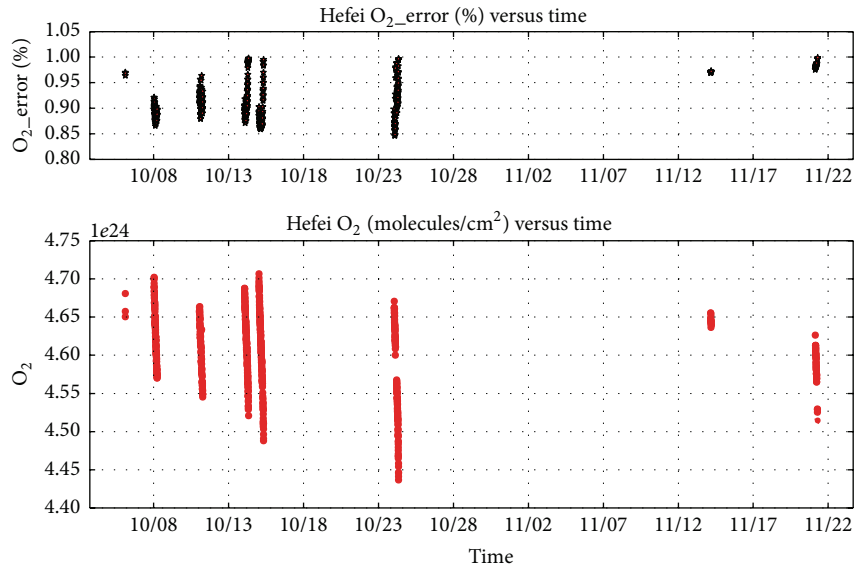


FIGURE 7:  $\text{VCD}_{\text{O}_2}$  time series ranging from October 6, 2014, to December 1, 2014, which are the retrieval values in  $7885\text{ cm}^{-1}$  window.

TABLE 1: Retrieval window parameters for  $\text{CO}_2$ ,  $\text{CH}_4$ , and  $\text{O}_2$ .

Gases to fit	Central frequencies ( $\text{cm}^{-1}$ )	Width ( $\text{cm}^{-1}$ )
$\text{CO}_2$ , $\text{H}_2\text{O}$ , $\text{HDO}$ , and $\text{CH}_4$	6220.00	80.00
$\text{CO}_2$ , $\text{H}_2\text{O}$ , and $\text{HDO}$	6339.50	85.00
$\text{CH}_4$ , $\text{CO}_2$ , $\text{H}_2\text{O}$ , and $\text{HDO}$	5938.00	116.00
$\text{CH}_4$ , $\text{CO}_2$ , $\text{H}_2\text{O}$ , and $\text{HDO}$	6002.00	11.10
$\text{CH}_4$ , $\text{CO}_2$ , $\text{H}_2\text{O}$ , and $\text{HDO}$	6076.00	138.00
$\text{O}_2$ , $\text{CO}_2$ , $\text{H}_2\text{O}$ , and $\text{HF}$	7885.00	240.00

both  $\text{CO}_2$  and  $\text{CH}_4$ . The  $\text{VCD}_{\text{CO}_2}$  in Figure 5 is the average of the fitted results in 6220 and  $6339\text{ cm}^{-1}$  windows. The averaged fitting errors for  $\text{CO}_2$  are less than 1%. Most  $\text{VCD}_{\text{CO}_2}$  lies between  $8.2$  and  $8.8 \times 10^{21}$  molecules/ $\text{cm}^2$ . The  $\text{VCD}_{\text{CH}_4}$  in Figure 6 is the average of the results in  $5938\text{ cm}^{-1}$ ,  $6002\text{ cm}^{-1}$ , and  $6076\text{ cm}^{-1}$  windows. Most  $\text{VCD}_{\text{CH}_4}$  lies between  $3.7$  and  $4.1 \times 10^{19}$  molecules/ $\text{cm}^2$ . The averaged fitting errors for  $\text{CH}_4$  are also less than 1%. Figure 7 is the  $\text{VCD}_{\text{O}_2}$  time series retrieved from  $7885\text{ cm}^{-1}$  window with fitting error of  $<1\%$ . VCDs as shown in Figures 5~7 are intermediate products of data analysis and so postprocessing procedures

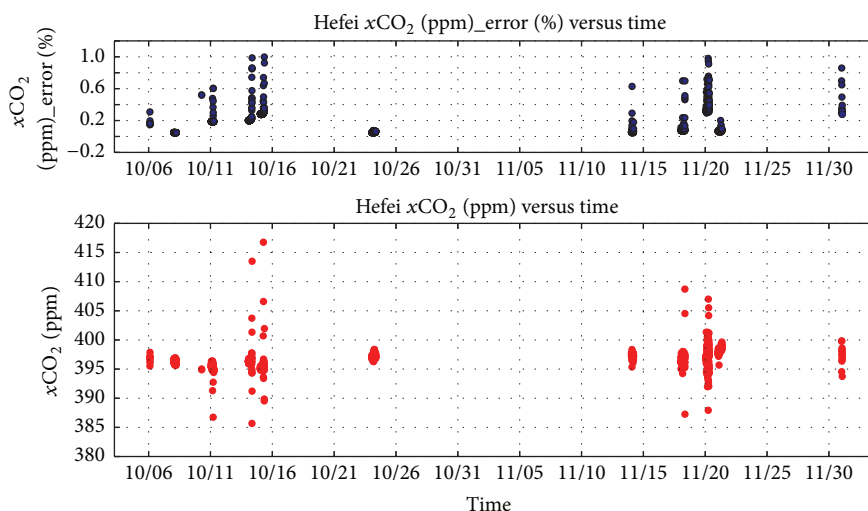


FIGURE 8: DMF<sub>CO<sub>2</sub></sub> time series ranging from October 6, 2014, to December 1, 2014, which are calculated according to VCD<sub>CO<sub>2</sub></sub> and VCD<sub>O<sub>2</sub></sub>.

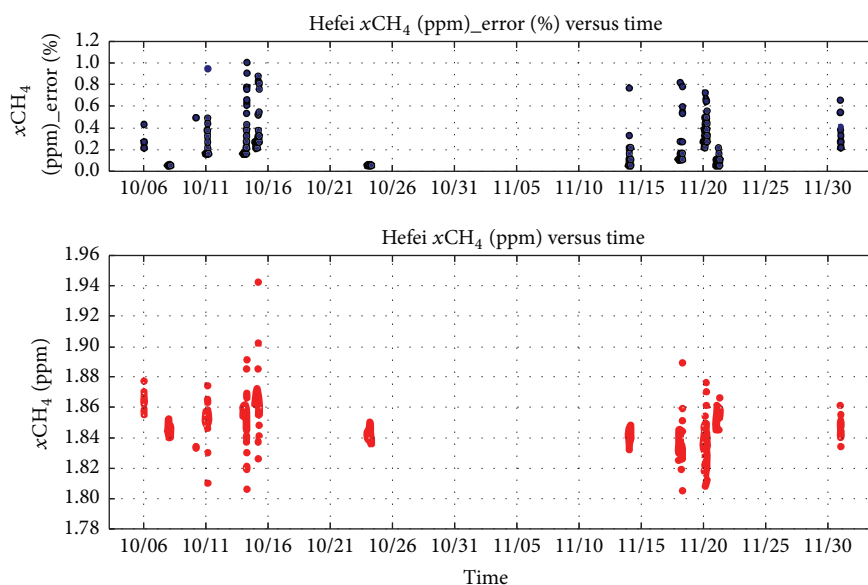


FIGURE 9: DMF<sub>CH<sub>4</sub></sub> time series ranging from October 6, 2014, to December 1, 2014, which are calculated according to VCD<sub>CH<sub>4</sub></sub> and VCD<sub>O<sub>2</sub></sub>.

are not applied to them. Time series of DMF<sub>CO<sub>2</sub></sub> and DMF<sub>CH<sub>4</sub></sub>, respectively, in Figures 8 and 9 are calculated by the ratio of VCD<sub>CO<sub>2</sub></sub>/VCD<sub>O<sub>2</sub></sub> and VCD<sub>CH<sub>4</sub></sub>/VCD<sub>O<sub>2</sub></sub>, respectively. DMFs are final products of the data analysis. Both retrieval errors and precision are improved greatly (with less scatters).

In addition, the diurnal variations of DMF<sub>CO<sub>2</sub></sub> and DMF<sub>CH<sub>4</sub></sub> are investigated based on typical daily measurements. The diurnal variations of both DMF<sub>CO<sub>2</sub></sub> and DMF<sub>CH<sub>4</sub></sub> are clearly observed, which are shown in Figures 10 and 11, respectively. Precision ( $1\sigma$  standard error) for both DMF<sub>CO<sub>2</sub></sub> and DMF<sub>CH<sub>4</sub></sub> is less than 0.1%. DMF<sub>CO<sub>2</sub></sub> concentrates on around 396 ppmv with diurnal variation amplitude of  $\sim 2$  ppm. DMF<sub>CH<sub>4</sub></sub> concentrates on around 1845 ppbv with diurnal variation amplitude of  $\sim 15$  ppbv. The peak in DMF<sub>CO<sub>2</sub></sub> and DMF<sub>CH<sub>4</sub></sub> on October 24, 2014, may be caused by human activities. The observed diurnal variations do not indicate

any feature so far, but with the increase of the number of observations we will do further research.

## 5. Conclusions and Discussion

CO<sub>2</sub> and CH<sub>4</sub> are important greenhouse gases and carbon compounds. Capturing their variations in the atmosphere is of importance to determine their source or sink information. This study uses high resolution Fourier transform near IR solar spectra to calculate the CO<sub>2</sub> and CH<sub>4</sub> VCDs and DMFs. The preliminary retrieval results for CO<sub>2</sub> and CH<sub>4</sub> variations in the area of Hefei, China, are presented, and the underlying error sources are also analyzed. The results show that tiny variations of CO<sub>2</sub> and CH<sub>4</sub> in the atmosphere can be clearly resolved. The retrieval error is dominated by the deficiencies in the forward model. Future work will concentrate on

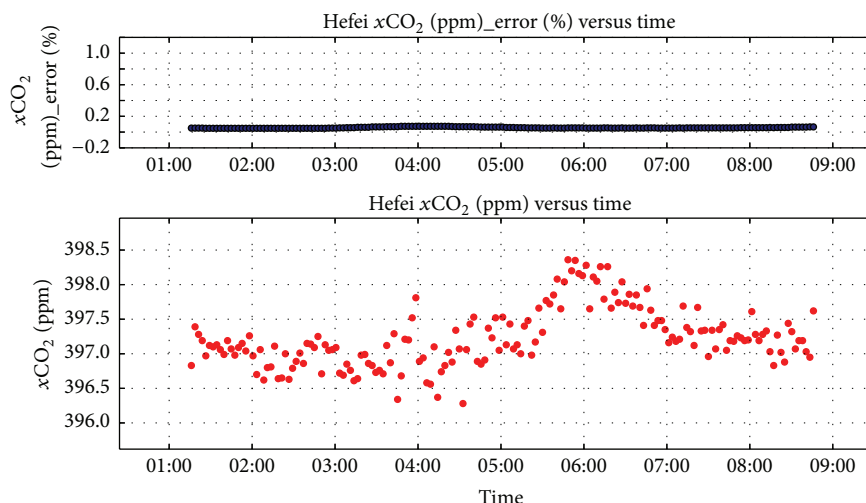


FIGURE 10: DMF<sub>CO<sub>2</sub></sub> time series on October 24, 2014, which are calculated according to VCD<sub>CO<sub>2</sub></sub> and VCD<sub>O<sub>2</sub></sub>.

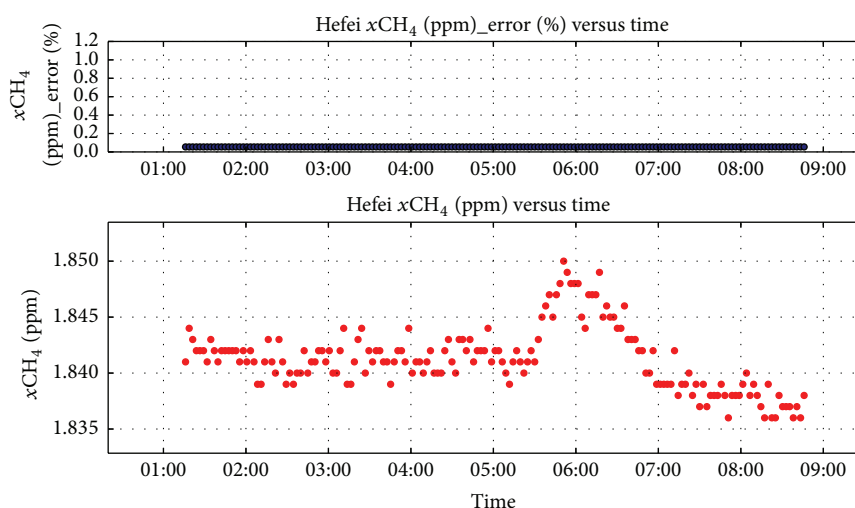


FIGURE 11: DMF<sub>CH<sub>4</sub></sub> time series on October 24, 2014, which are calculated according to VCD<sub>CH<sub>4</sub></sub> and VCD<sub>O<sub>2</sub></sub>.

optimizing the input parameters of the model and calibrate the instrument regularly with HCl cell. We are confident that, with these improvements, this technical will be more than adequate for future climate change forecast and satellite-based column observations validation.

### Conflict of Interests

The authors declare that there is no conflict of interests regarding the publication of this paper.

### Acknowledgments

This work is jointly supported by the National Natural Science Foundation of China (Grant no. 41275038), the Key Research Program of the Chinese Academy of Sciences (Grant no. KJZD-EW-TZ-G06), the National High Technology Research and Development Program of China (Grants nos. 2014AA06A508 and 2014AA06A511), the Scientific and Technological Project

of Anhui Province (Grant no. 1301022083), and the Natural Science Foundation of Anhui Province (Grant no. 1308085QF124). The authors would like to thank Caltech JPL for providing the source code of GFIT which formed the basis of the retrieval program in this study. They also give great thanks to Bremen IUP for assisting in the spectra retrieval.

### References

- [1] R. J. Andres, G. Marland, and S. Bischof, *Global and Latitudinal Estimates of  $\delta^{13}C$  from Fossil-Fuel Consumption and Cement Manufacture*, Carbon Dioxide Information Center, Oak Ridge National Laboratory, Oak Ridge, Tenn, USA, 1999, <ftp://cdiac.ornl.gov/pub/db1013/>.
- [2] GLOBALVIEW-CO2: Cooperative Atmospheric Data Integration Project 21 Carbon Dioxide, CDROM, NOAA ESRL, Boulder, Colo, USA, 2009, <ftp://ftp.cmdl.noaa.gov/products/globalview/co2/>.

- [3] F. Chevallier, N. M. Deutscher, T. J. Conway et al., "Global CO<sub>2</sub> fluxes inferred from surface air-sample measurements and from TCCON retrievals of the CO<sub>2</sub> total column," *Geophysical Research Letters*, vol. 38, no. 24, pp. 1–5, 2011.
- [4] T. Warneke, A. K. Petersen, C. Gerbig et al., "Co-located column and in situ measurements of CO<sub>2</sub> in the tropics compared with model simulations," *Atmospheric Chemistry and Physics*, vol. 10, no. 12, pp. 5593–5599, 2010.
- [5] D. Wunch, G. C. Toon, J.-F. L. Blavier et al., "The total carbon column observing network," *Philosophical Transactions of the Royal Society A: Mathematical, Physical and Engineering Sciences*, vol. 369, no. 1943, pp. 2087–2112, 2011.
- [6] T. Warneke, Z. Yang, S. Olsen et al., "Seasonal and latitudinal variations of column averaged volume-mixing ratios of atmospheric CO<sub>2</sub>," *Geophysical Research Letters*, vol. 32, no. 3, pp. 2–5, 2005.
- [7] A. J. Cogan, H. Boesch, R. J. Parker et al., "Atmospheric carbon dioxide retrieved from the Greenhouse gases Observing SATellite (GOSAT): comparison with ground-based TCCON observations and GEOS-Chem model calculations," *Journal of Geophysical Research: Atmospheres*, vol. 117, no. 21, 2012.
- [8] J. Messerschmidt, R. Macatangay, J. Notholt, T. Warneke, and C. Weinzierl, "Side by side measurements of CO<sub>2</sub> by ground-based Fourier transform spectrometry (FTS)," *Tellus B*, vol. 62, no. 5, pp. 749–758, 2010.
- [9] R. Sussmann, A. Ostler, F. Forster et al., "First intercalibration of column-averaged methane from the total carbon column observing network and the network climate for the detection of atmospheric composition change," *Atmospheric Measurement Techniques*, vol. 6, no. 2, pp. 397–418, 2013.
- [10] F. Hase, T. Blumenstock, and C. Paton-Walsh, "Analysis of the instrumental line shape of high-resolution Fourier transform IR spectrometers with gas cell measurements and new retrieval software," *Applied Optics*, vol. 38, no. 15, pp. 3417–3422, 1999.
- [11] S. Dohe, V. Sherlock, F. Hase et al., "A method to correct sampling ghosts in historic near-infrared Fourier Transform Spectrometer (FTS) measurements," *Atmospheric Measurement Techniques*, vol. 6, no. 8, pp. 1981–1992, 2013.
- [12] H. Tran, J.-M. Hartmann, G. Toon et al., "The 2ν<sub>3</sub> band of CH<sub>4</sub> revisited with line mixing: consequences for spectroscopy and atmospheric retrievals at 1.67 μm," *Journal of Quantitative Spectroscopy and Radiative Transfer*, vol. 111, no. 10, pp. 1344–1356, 2010.
- [13] L. Kuai, D. Wunch, R.-L. Shia, B. Connor, C. Miller, and Y. Yung, "Vertically constrained CO<sub>2</sub> retrievals from TCCON measurements," *Journal of Quantitative Spectroscopy and Radiative Transfer*, vol. 113, no. 14, pp. 1753–1761, 2012.
- [14] M. C. Geibel, C. Gerbig, and D. G. Feist, "A new fully automated FTIR system for total column measurements of greenhouse gases," *Atmospheric Measurement Techniques*, vol. 3, no. 5, pp. 1363–1375, 2010.
- [15] Z. H. Yang, G. C. Toon, J. S. Margolis, and P. O. Wennberg, "Atmospheric CO<sub>2</sub> retrieved from ground-based near IR solar spectra," *Geophysical Research Letters*, vol. 29, no. 9, 2002.